Thèse n° 8933

In situ nanoscale studies of copper-based catalysts for carbon dioxide electroreduction

Présentée le 24 août 2021

Faculté des sciences de base
Laboratoire de science à l'échelle nanométrique
Programme doctoral en physique

pour l'obtention du grade de Docteur ès Sciences

par

Karla BANJAC

Acceptée sur proposition du jury

Prof. R. Houdré, président du jury
Dr. M. A. Lingenfelder, directrice de thèse
Prof. B. Roldán Cuenya, rapporteuse
Prof. M. T. M. Koper, rapporteur
Prof. G. Tagliabue, rapporteuse

École
polytechnique
fédérale
de Lausanne

2021

"God made the bulk;
the surface was invented by the devil."
— Wolfang Pauli

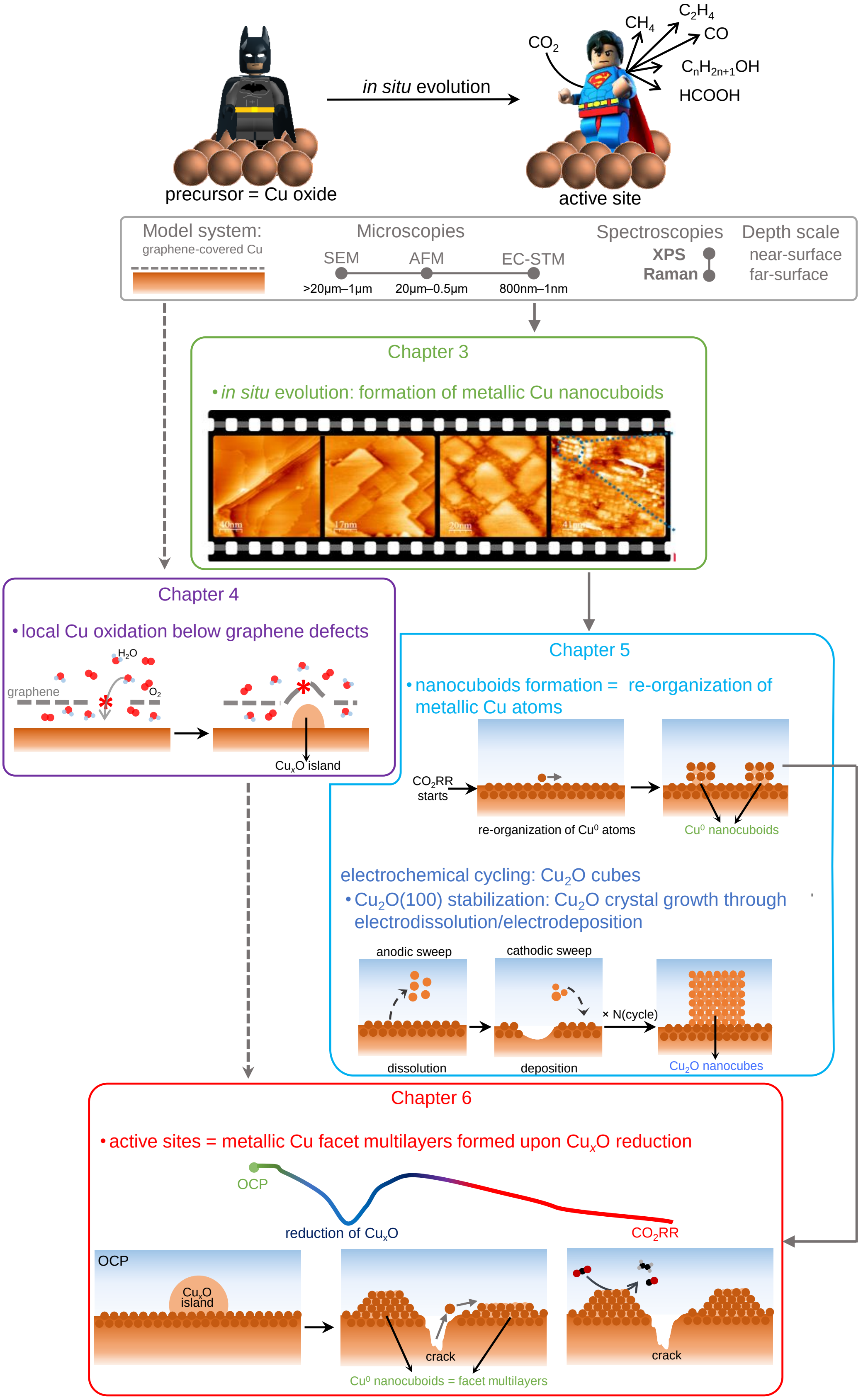
precursor = Cu oxide
in situ evolution
CO_2
CH_4
C_2H_4
CO
$C_nH_{2n+1}OH$
HCOOH
active site
Model system:
graphene-covered Cu
Microscopies
SEM
AFM
EC-STM
>20μm–1μm
20μm–0.5μm
800nm–1nm
Spectroscopies
XPS
Raman
Depth scale
near-surface
far-surface
Chapter 3
• in situ evolution: formation of metallic Cu nanocuboids
40nm
17nm
20nm
41nm
Chapter 4
• local Cu oxidation below graphene defects
H_2O
graphene
O_2
Cu_xO island
Chapter 5
• nanocuboids formation = re-organization of metallic Cu atoms
CO_2RR starts
re-organization of Cu^0 atoms
Cu^0 nanocuboids
electrochemical cycling: Cu_2O cubes
• $Cu_2O(100)$ stabilization: Cu_2O crystal growth through electrodissolution/electrodeposition
anodic sweep
cathodic sweep
× N(cycle)
dissolution
deposition
Cu_2O nanocubes
Chapter 6
• active sites = metallic Cu facet multilayers formed upon Cu_xO reduction
OCP
reduction of Cu_xO
CO_2RR
OCP
Cu_xO island
crack
crack
Cu^0 nanocuboids = facet multilayers

Abstract

The urgency of climate change demands the simultaneous removal of carbon dioxide from the atmosphere and the transition to renewable energy sources. This aim is realizable through electrochemical reduction of carbon dioxide (CO_2RR), which is a promising route for synthesizing renewable carbon-based fuels and chemicals.

Among many existing CO_2RR catalysts, copper is the only earth-abundant metal that produces energy-rich molecules. Practical application is hindered by its poor product selectivity and modest long-term catalyst stability. To overcome these limitations, an atomistic understanding of the catalytic processes and identification of CO_2RR active sites on Cu are needed.

Current research implies that the active sites form upon the catalysts' evolution during the reaction. However, fast Cu oxidation hinders their identification in conventional *ex situ* studies. The following questions remain unanswered: What are the morphology and chemical composition of the active sites? How do they form?

This thesis explores the *in situ* evolution of Cu-based CO_2RR catalysts. We study this phenomenon down to the nanoscale through a synergy of *in situ* microscopy and spectroscopy studies. We employ graphene as a 2D protecting layer on Cu to study the Cu nanoscale structural evolution *in situ* via electrochemical scanning tunneling microscopy (EC-STM). We use *in situ* Raman and X-ray photoelectron spectroscopies to study the evolution of the Cu catalysts' oxidation state.

First, EC-STM studies reveal the formation of few nanometer-sized cuboids on Cu catalysts as the main structural evolution during CO_2RR. We show that this evolution occurs in aqueous electrolytes over a wide range of pH and compositions. Second, we show that metallic Cu is the active phase. Reduction of the Cu oxide, formed either through chemical synthesis or through the exposure of Cu catalysts to air, is unavoidable prior to CO_2RR.

To understand the nanocuboid formation mechanism, we present a comparative study of the Cu nanocuboids formed upon CO_2RR and the Cu_2O cubes prepared through electrochemical cycling synthesis. Morphological and chemical composition differences between them allow us to conclude on distinct formation mechanisms. We show that the metallic Cu nanocuboids form during a potential-driven re-organization of atoms in the topmost surface layers.

Furthermore, we present EC-STM studies revealing the atomistic details of the Cu nanocuboid formation. By comparing these processes with the multilayer mound growth in Cu homoepitaxy, we show that the nanocuboids are (100) facet multilayers formed upon reduction of Cu oxides. We propose that the nanocuboids are CO_2RR active sites, ultimately forming on any Cu catalyst regardless of its initial macroscopic shape and oxidation state.

The *in situ* identification of active sites, presented here, offers a unique framework for the re-interpretation of the existing literature, invites further fundamental theoretical and experimental research, and paves the way for rational catalyst design. Moreover, this thesis further demonstrates the importance of *in situ* studies across different length scales in understanding key catalytic processes in renewable energy schemes.

Keywords: electrochemical reduction of carbon dioxide, Cu-based catalysts, *operando* surface science, *in situ* evolution, active sites, electrochemical scanning tunneling microscopy, electrochemical Raman spectroscopy, X-ray photoelectron spectroscopy, atomic force microscopy.

Résumé

L'urgence du changement climatique exige l'élimination simultanée du dioxyde de carbone de l'atmosphère et la transition vers des sources d'énergie renouvelables. Ces objectifs sont réalisables grâce à la réduction électrochimique du dioxyde de carbone (CO_2RR), une voie prometteuse pour la synthèse de carburants et de produits chimiques renouvelables à base de carbone. Parmi les nombreux catalyseurs de CO_2RR existants, le cuivre est le seul métal abondant sur Terre qui produise des molécules riches en énergie. L'application pratique de la CO_2RR catalysée par Cu est entravée par une mauvaise sélectivité en produits ainsi que par la modeste stabilité de ce catalyseur à long terme.

Les recherches actuelles laissent entendre que les sites actifs se forment lors de l'évolution des catalyseurs au cours de la réaction. Cependant, l'oxydation rapide du Cu empêche leur identification par des études *ex situ* conventionnelles. Les questions suivantes restent sans réponse : quelles sont la morphologie et la composition chimique des sites actifs ? Comment se forment-ils ?

Cette thèse explore l'évolution *in situ* des catalyseurs de CO_2RR à base de Cu. Nous étudions ce phénomène jusqu'à l'échelle nanométrique grâce à une synergie d'études de microscopie et de spectroscopie *in situ*. Nous exploitons des surfaces en Cu polycristallin recouvertes de graphène ; nous employons la microscopie à effet tunnel électrochimique (EC-STM) pour étudier l'évolution structurelle à l'échelle nanométrique *in situ* ; nous utilisons les spectroscopies photoélectroniques *in situ* Raman et par rayons X afin d'étudier l'évolution de l'état d'oxydation des catalyseurs Cu.

Premièrement, les études EC-STM révèlent que quelques cuboïdes de taille nanométrique sur des catalyseurs Cu constituent la principale évolution structurelle *in situ*. Nous montrons que cette évolution se produit dans les électrolytes aqueux quels que soient leur pH et leur composition. Deuxièmement, nous montrons que le Cu métallique est la phase active.

Pour comprendre le mécanisme de formation des nanocuboïdes, nous présentons une étude comparative des nanocuboïdes formés lors de la CO_2RR et des cubes de Cu_2O préparés par synthèse par cycles électrochimiques précédemment rapportée. Nous montrons que les nanocuboïdes métalliques de Cu se forment en raison de la réorganisation des atomes dans les couches superficielles supérieures, dirigée par le potentiel. De plus, nous présentons des études EC-STM révélant les détails atomistiques de la formation de nanocuboïdes Cu. En comparant ces processus avec la formation de multicouches à facettes dans l'homoépitaxie de Cu, nous montrons que les nanocuboïdes sont des multicouches à facettes (100) formées lors de la réduction des oxydes de Cu. Nous proposons l'hypothèse que les multicouches à facettes sont les sites actifs de la CO_2RR, qui se forment finalement sur n'importe quel catalyseur Cu indépendamment de sa forme macroscopique initiale et de son état d'oxydation.

Cette thèse offre un cadre unique pour la réinterprétation de la littérature existante et ouvre la voie à de nouvelles recherches sur la CO_2RR catalysée par Cu. Il démontre en outre l'importance des études *in situ* sur différentes échelles de longueur dans la compréhension des processus catalytiques clés des schémas d'énergie renouvelable.

Mots-clés : électrocatalyse de la reduction du dioxide de carbone, électrocatalyse, catalyseurs Cu, *operando* science des surfaces, évolution dynamique, microscopie à effet tunnel électrochimique, spectroscopie Raman électrochimique.

List of acronyms

AFM	atomic force microscopy
CE	counter electrode
CO_2RR	electrochemical reduction reaction of carbon dioxide
CV	cyclic voltammetry
DFT	density functional theory
ECSA	electrochemically active surface area
(EC-)STM	(electrochemical) scanning tunneling microscopy
ES	Ehrlich-Schwoebel
GC	gas chromatography
G-Cu	graphene-covered polycrystalline Cu
GIXRD	grazing incidence X-ray diffraction
HER	hydrogen evolution reaction
HOPG	highly oriented pyrolitic graphite
HPLC	high performance liquid chromatography
LSV	linear sweep voltammetry
ML	monolayer
NC	nanocube
OER	oxygen evolution reaction
OLEMS	online electrochemical mass spectrometry
PEC	photoelectrochemical cell
RE	reference electrode
RHE	reversible hydrogen electrode
SEM	scanning electron microscopy
OCP	open circuit potential
OER	oxygen evolution reaction
TEM	transmission electron microscopy
UHV	ultra-high vacuum
XPS	X-ray photoelectron spectroscopy

Contents

Abstract **iii**

Résumé **v**

List of acronyms **vii**

1 Introduction **1**
- 1.1 Global warming 1
- 1.2 Electrochemical reduction of carbon dioxide 6
- 1.3 Structural evolution across length scales 7
- 1.4 Thesis overview 8

I Setting the stage **11**

2 Experimental methods **13**
- 2.1 Microscopy 14
  - 2.1.1 Scanning probe microscopies 14
  - 2.1.2 Scanning electron microscopy 20
- 2.2 Spectroscopy 20
  - 2.2.1 Raman spectroscopy 21
  - 2.2.2 X-ray photoelectron spectroscopy 24
- 2.3 Complementary techniques 25
  - 2.3.1 Electrochemical characterization 25
  - 2.3.2 CO_2RR product analysis 26
- 2.4 Surface science studies: Model systems 28

II Surface evolution **33**

3 Emergence of Cu nanocuboids during CO_2RR **35**
- 3.1 Introduction 37
- 3.2 Experimental details 37
- 3.3 Results 38
- 3.4 Discussion 43
- 3.5 Conclusion 45

III Surface chemistry **47**

4 Oxidation of G-Cu **49**
4.1 Introduction . . . 50
4.2 Experimental section . . . 50
4.3 Results . . . 51
4.3.1 Ambient oxidation . . . 51
4.3.2 Oxidation in contact with electrolyte . . . 54
4.4 Discussion . . . 56
4.5 Conclusion . . . 59

5 *In situ* surface chemistry: Cu nanocuboids *versus* Cu_2O nanocubes **61**
5.1 Introduction . . . 63
5.2 Experimental details . . . 64
5.3 Results . . . 65
5.3.1 Morphology differences . . . 65
5.3.2 Chemical composition differences . . . 68
5.3.3 Effect of chloride on Cu_2O cube formation . . . 69
5.4 Discussion and conclusions . . . 70

IV Surface physics **75**

6 *In situ* surface physics: Mechanism of Cu nanocuboid formation during CO_2RR **77**
6.1 Introduction . . . 79
6.2 Experimental procedures . . . 79
6.3 Results . . . 80
6.3.1 Mound formation over hundred-nanometer scale: Implications of the mechanism . . . 80
6.3.2 Mound formation on sub-nanometer scale: Atomistic insights through qualitative description . . . 84
6.3.3 Mound formation during CO_2RR . . . 87
6.4 Discussion and conclusion . . . 89

V The end **93**

7 Final remarks **95**

A Stability of graphene during CO_2RR **99**

B Supplementary Information: Chapter 3 **103**

C Supplementary Information: Chapter 5 **109**

D Supplementary Information:

- Chapter 6 117

Bibliography 123

Acknowledgements 141

Publication list 143

Curriculum Vitae 145

1 Introduction

1.1 Global warming

Climate change is the central issue of the modern society. Although it is not the first climate change in the history of the planet Earth, it is the first one that greatly threats over 7.8 billion people and the first one that is fully driven by the human impact through extensive emission of greenhouse gases.

The most concerning evidence of climate change is global warming, characterized by an alarming rise in average temperature of about 0.2 °C per decade since the pre-industrial times. Putting this information in the historical context, the past six years are the six warmest years on record.[1] An extensive list of direct physical consequences threatening the biosphere includes global sea rising, glacial melting, droughts and (marine) heatwaves, ocean acidification, river floods, wildfires, abnormal lighting activity, desertification, among others. These climate disasters are further correlated to increased food and health insecurity as well as socioeconomic issues, including evacuations and armed conflicts.

Vivid examples of the impact of climate change in 2020 include extreme minimum sea-ice extent in the Arctic (second lowest on record), loss of 152 Gt of ice, heavy rains and extensive flooding in Africa and Asia, severe droughts in South America, and the largest north Atlantic hurricane season with 30 named storms. Further expanding this list to the indirect consequences, I highlight displacement of 9.8 million people due to hydro-meteorological disasters in Africa, dislocation of more than 4.8 million people in India and Bangladesh due to Cyclone Amphan in May, evacuation of 2.2 million people in China due to floods and landslide and 1.3 million people in Vietnam due to Typhoon Molave. Moreover, the U.S. government reports on a total cost of 95 billion dollars, mainly due to Hurricane Laura, the August derecho, and the Western wildfires.[2]

The threat of the irreversible impacts, to be avoided only if keeping the global warming below 1.5 °C compared to pre-industrial levels,[3] call for instant mitigation. The goal is clear: global greenhouse gas emission needs to be net-zero by 2050.[4] Strategies relying on decarbonization, carbon sequestration, and carbon recycling focus on renewable energy, where a combination of decarbonization and carbon recycling to high-energy products is especially appealing.

A process that converts atmospheric CO_2 into high-energy carbohydrates is known in nature as photosynthesis, in which plants use a renewable energy source: sunlight. Photosynthesis involves reactions driven by sunlight and carbon fixation reactions with the net equation being:

$$\mathrm{CO_2} + \mathrm{H_2O} + h\nu \rightarrow \mathrm{CH_2O} + \mathrm{O_2},$$

where $h\nu$ stands for photon energy and CH_2O represents carbohydrates, primary sucrose and starch. The photosynthetic apparatus, situated in chloroplasts, consists of two photosystems that respond to light with a wavelength shorter than 700 nm. In this complex reaction scheme, light, absorbed by pigment molecules, *i.e.*, chlorophylls, generates high-energy electrons that are used to produce nicotinamide adenine dinucleotide phosphate (NADPH) and adenosine triphosphate (ATP) molecules, while O_2 is a side product. NADPH is the main reducing agent for biosynthesis reactions; ATP is considered as the molecular unit currency of intracellular energy transfers. NADPH and ATP produced in the light reactions thus drive the reduction of CO_2 to carbohydrates through carbon fixation reactions.

Only 48.7% of the energy emitted from the Sun falls into the photosynthetically active band.[5] Surface reflections reduce the efficiency of the plantal photoabsorption in this photosynthetically active range; hence, the plants absorb 60% of the light.[6] Moreover, imperfect light absorption, rapid relaxation of high excited states in chlorophylls, poor efficiency of the energy transfer between photosystem-I and photosystem-II, and (photo)respiration lead to additional energy losses and decrease of the maximum theoretical photosynthesis efficiency down to 4.6% for C_3 and 6% for C_4 plants.[5] These obstacles call for artificial photosynthetic systems composed of broadband photoabsorbers and efficient catalysts for the CO_2 reduction reaction (CO_2RR), where all components should be durable and made of earth-abundant materials.

Artificial photosynthesis systems consist of a semiconductor-based photovoltaic solar cell and two electrodes assembled in a photoelectrochemical cell (PEC), where reduction reactions occur on the cathode and oxygen evolution might be a counter reaction on the anode. While these three components are essential, one finds a wide range of device architectures classified in two categories: i) a combination of a photovoltaic cell and an unbiased electrolyzer in a modular PEC, where the photovoltaic cell is either coupled with the electrolyzer through external wiring or acts as a support for the cathode or the anode and ii) an integrated PEC with at least one photoelectrode.

Renewable fuels are always produced in reduction reactions on the cathodes. The reaction is either the hydrogen evolution reaction (HER):

$$2\mathrm{H}^+ + 2\mathrm{e}^- \rightarrow \mathrm{H_2}$$

or the reduction of carbon dioxide (CO_2RR):

$$xCO_2 + nH^+ + ne^- \rightarrow \text{product} + yH_2O,$$

where “product” denotes a variety of reduced carbon compounds to be used as renewable fuels and chemicals (Figure 1.1). In both cases, the oxygen evolution reaction (OER): $2H_2O \rightarrow O_2(g) + 4H^+ + 4e^-$ is a counter reaction on the anode.

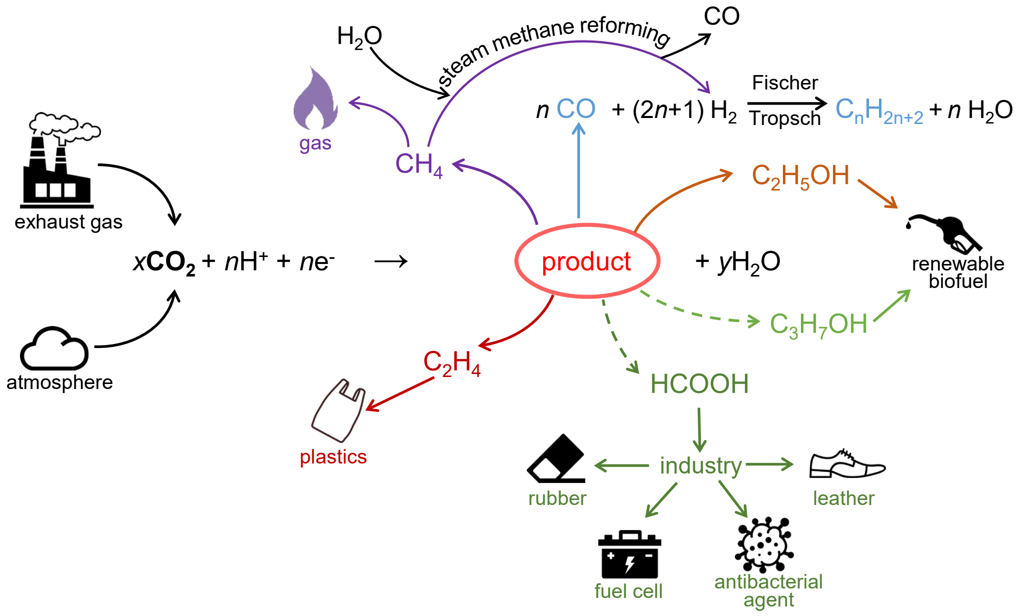
H$_2$O
steam methane reforming
CO
gas
CH$_4$
n CO + (2n+1) H$_2$
Fischer
Tropsch
C$_n$H$_{2n+2}$ + n H$_2$O
exhaust gas
C$_2$H$_5$OH
renewable biofuel
xCO$_2$ + nH$^+$ + ne$^-$ →
product
+ yH$_2$O
C$_3$H$_7$OH
atmosphere
C$_2$H$_4$
HCOOH
plastics
industry
rubber
leather
fuel cell
antibacterial agent

Figure 1.1 – **Electrochemical reduction of carbon dioxide.** Schematic illustration of CO_2 recycling based on CO_2RR. CO_2, captured either at industrial point sources or from air, is converted to reduced products. CO_2RR products can be used as renewable fuels or as renewable chemicals. The reactions are listed in Table 1.2.

CO_2RR is a preferable reaction for fuel generation due to the high volumetric energy densities of carbon-based fuels that can be easily integrated in the existing infrastructure. However, the inefficiencies of CO_2RR catalysts currently limit their integration in PEC devices. This is evident from the state-of-the-art CO_2RR-based PEC research, where a very few examples in Table 1.1 demonstrate the lack of selectivity towards CO_2RR products beyond HCOOH and CO.[7] Moreover, the choice of unsustainable materials represents a mining threat for biodiversity.[24] A sustainable strategy for renewable energy production thus calls for utilization of earth-abundant materials as catalysts.

Design of CO_2RR-based PEC is a tremendous scientific and technological challenge that calls for a combined optimization of the individual components and the assembled PEC device. The complexity of the PEC integration comes from the issues associated with catalysts’ scale-up and interfacial losses. These challenges are to be overcome through a multidisciplinary approach, where the experts in catalysis, interfacial engineering, and PEC design offer a unique pool of background knowledge. An example of such an interdisciplinary team is the consortium of the A-LEAF project, aiming at the realization of an artificial photosynthesis device. The A-LEAF project, a collaborative project joining the experts

Table 1.1 – **CO_2RR-based photoelectrochemical devices.** STF stands for solar-to-fuel efficiency, where the fuels are CO_2RR products. FE stands for faradaic efficiency. Table adapted from reference 7.

Modular PEC devices

Photovoltaic	Cathode	Anode	Main product / FE	STF/%	Ref.
GaInP/ GaInAs/Ge	SnO_2/CuO	SnO_2/CuO	CO / 81	13.8	8
perovskite	anodized Au	IrO_2	CO / 90	6.5	9
Si	Mn complex	FeO_x/NiO_x	CO / 80	3.4	10
Si	Cu foam/Zn flakes	Ni foam	CO / 16	4.3	11
Si	Cu/Bi dendrites	IrO_2	HCOOH / 95	8.5	12

Integrated PEC devices

Cathode	Anode	Product-1/FE	Product-2/FE	STF/%	Ref.
WSe_2	Co(II)-oxide/ hydroxide	CO / 24	/	4.6	13
CuO/$CuFeO_2$	Pt	HCOOH / 90	/	1	14
Ti/Pd/C NPs	InGaP/GaAs/ TiO_2/Ni	HCOOH / 94	/	10	15
InP/Ru-complex	reduced $SrTiO_3$	HCOOH / 71	/	0.14	16
Ru-complex/ InP	TiO_2	HCOOH / 70	/	0.04	17
Ru-complex/ TiO_2/Fe_2O_3/ Cr_2O_3	TiO_2	HCOOH / 79	CO / 16	0.15	18
Co-complex/ perovskite	$CoO_x/BiVO_4$	CO / 25	/	0.02	19
Ag/Cu/TiO_2	IrO_2	CO / 25	/	3.5	20
ZnO–ZnTe–CdTe–Au	Ni foam/ Co-HCO_3	CO / 80	/	0.35	21
organic/TiN	$FeO_x/BiVO_4$	HCOOH / 77	/	0.08	22
RuRe-complex/ $CuGaO_2$	CoO_x/TaON	CO / 41	/		23

from 12 European universities and research centers, has rapidly become a world-leading symbol of group synergy overcoming the challenges of practical artificial photosynthesis. The importance of interdisciplinarity, especially evident at the frontiers between surface science, electrocatalytic studies, theoretical modeling, and interfacial engineering,[25–28] was of great importance for preliminary optimization of PEC components and for delicate

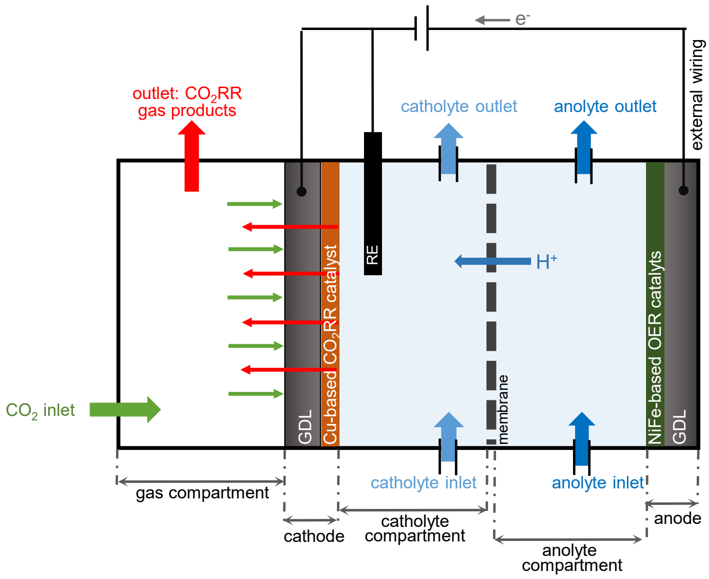
e$^-$
external wiring
outlet: CO_2RR gas products
catholyte outlet
anolyte outlet
RE
H$^+$
GDL
Cu-based CO_2RR catalyst
membrane
NiFe-based OER catalysts
GDL
CO_2 inlet
catholyte inlet
anolyte inlet
gas compartment
cathode
catholyte compartment
anolyte compartment
anode

Figure 1.2 – **Artificial leaf device.** Scheme of the (photo)electrochemical cell designed in the A-LEAF consortium. Two schemes for integration of the photovoltaic cell (not shown here) are: a photovoltaic cell as support for the anode and a photovoltaic cell connected through external wiring. Scheme not to scale.

synthesis/preparation adjustments needed for their integration in a PEC device.

A scheme of the A-LEAF electrolyser, developed and optimized in the group of Professor Siglinda Perathoner at Universitá degli Studi di Messina, is shown in Figure 1.2. This advanced version of the integrated PEC device consists of a three-compartment electrolyser and a photovoltaic Si-based heterojunction cell: these two components can be coupled through external wiring, while the exact coupling scheme is yet to be determined based on the results of the performance tests currently being performed in the groups of the A-LEAF partners. The advantages of the three-compartment electrolyser are: prolonged electrolysis by combining an electrolyser with the catholyte and anolyte flow systems; separation of the gas and liquid CO_2RR products; enhanced performance of the Cu-based CO_2RR catalysts at the three-phase cathodic interface[29]. Moreover, preliminary performance tests of the state-of-the-art Cu-based CO_2RR and NiFe-based OER catalysts, synthesized and tested by the A-LEAF partners, support an optimistic forecast for the overall performance of the A-LEAF prototype.

Extensive knowledge on the individual prototype components reveals the poor selectivity and stability of CO_2RR catalysts as bottlenecks for further optimization of the CO_2RR-based PEC performance. This goes in line with the poor understanding of CO_2RR, where the knowledge gap extends from the fundamental questions on the reaction mechanism, the chemical composition and the morphology of the active sites, the *in situ* transformations, to the differences in reaction conditions and microenvironments.

Table 1.2 – **Electrochemical reactions of CO_2 reduction with equilibrium potentials.** Table adapted from reference 30.

Reaction	E^0 / V *vs* RHE	Product name
$CO_2 + 2H^+ + 2e^- \rightarrow HCOOH(aq)$	-0.12	Formic Acid
$CO_2 + 2H^+ + 2e^- \rightarrow CO(g) + H_2O$	-0.10	Carbon monoxide
$CO_2 + 6H^+ + 6e^- \rightarrow CH_3OH(aq) + H_2O$	-0.10	Methanol
$CO_2 + 8H^+ + 8e^- \rightarrow CH_4(g) + 2H_2O$	0.17	Methane
$2CO_2 + 8H^+ + 8e^- \rightarrow CH_3COOH(aq) + 2H_2O$	0.11	Acetic acid
$2CO_2 + 10H^+ + 10e^- \rightarrow CH_3CHO(aq) + 3H_2O$	0.06	Acetaldehyde
$CO_2 + 12H^+ + 12e^- \rightarrow C_2H_5OH(aq) + 3H_2O$	0.09	Ethanol
$CO_2 + 12H^+ + 12e^- \rightarrow C_2H_4(g) + 4H_2O$	0.08	Ethylene
$CO_2 + 18H^+ + 18e^- \rightarrow C_3H_7OH(aq) + 5H_2O$	0.1	Propanol

1.2 Electrochemical reduction of carbon dioxide

Initial screening of metal-based CO_2RR catalysts revealed that copper (Cu) is the only pure metal capable of converting CO_2 to C_{2+} products. As such, it stands out from other formate-producing (Pb, Hg, Tl, In, Sn, Cd, and Bi), CO-producing (Au, Ag, Zn, Pd, and Ga), and hydrogen-producing (Ni, Fe, Pt, and Ti) metals.[31,32] This classification was further explained through a theoretical study of the binding energy of HER and CO_2RR (COOH* and CO*) intermediates. Binding energies of both CO* and H* to Cu seem to be strong enough for co-binding, yet not too strong to poison the catalysts surface.[33]

Single-crystal studies revealed the correlations between the atomic arrangements of different Cu surfaces and their CO_2RR product selectivities. Cu(100) single crystals are selective towards ethylene, while Cu(111) single crystals produce methane.[34] This relationship further motivated rational design of (100)-rich Cu catalysts and extensive preparation of cubic nanocatalysts, *i.e.*, nanocubes. Broad literature on shape-controlled synthesis of catalysts via various synthetic routes, such as colloidal chemistry,[35] electrochemical treatments,[36,37] and reduction of halogen-based[38] or oxide-based cubic scaffolds, confirms a favored formation of C_{2+} products on Cu(100).

The review by Nitopi *et al.*[30] classifies Cu-based CO_2RR catalysts into three categories: nanoparticles, 3D interconnected catalysts, and bimetallics. The nanoparticles are individual particles of various shapes with a diameter below 100 nm, ideally supported on a highly-conductive and durable substrate; 3D interconnected catalysts are unsupported oxide-derived or non-oxide-derived electrodes; bimetallics exist in both nanoparticulate and interconnected form.

Among these classes, 3D interconnected catalysts derived from oxide precursors, *i.e.*, oxide-derived (OD) CO_2RR catalysts, have low overpotentials and enhanced product selectivity towards CO, HCOOH and C_{2+} products.[39–41] Pioneering reports on OD Cu revealed *highly active sites along the grain boundaries*[42] and *across the surrounding surface.*[43] Interestingly, the *active sites relax upon annealing* to a moderate temperature of up to 200 °C *without significant changes in the grain boundaries*. These results led to the hypothesis that the oxide species are the key components of the active sites.[44,45] However, the stability of the oxide species is counter-intuitive at the negative potentials at which CO_2RR occurs. Differences in *ex situ vs in situ* spectroscopic findings on the chemical composition of (OD-)Cu CO_2RR catalysts present the first challenge towards fundamental understanding of Cu-catalyzed CO_2RR.

Understanding the chemical composition and morphology under *in situ* conditions is thus the key for the transition from the black box approach, focusing on efficient CO_2RR performance without atomistic understanding, to the white box approach based on the detailed knowledge of the reaction mechanism and CO_2RR active sites. Historically, this interest in the nature of the Cu-based catalysts during CO_2RR coincides with a general interest in *in situ* and operando characterization and the emergence of a new research field at the interface between traditional surface science and catalysis.

1.3 Structural evolution across length scales

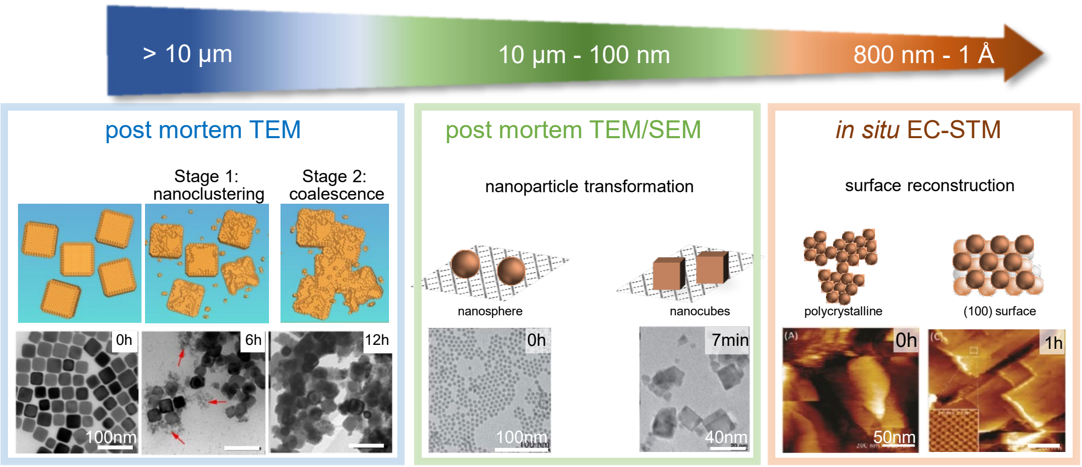
> 10 µm
10 µm - 100 nm
800 nm - 1 Å
post mortem TEM
Stage 1: nanoclustering
Stage 2: coalescence
0h
6h
12h
100nm
post mortem TEM/SEM
nanoparticle transformation
nanosphere
nanocubes
0h
7min
100nm
40nm
in situ EC-STM
surface reconstruction
polycrystalline
(100) surface
(A)
0h
(C)
1h
50nm

Figure 1.3 – ***In situ* structural evolution of Cu-based CO_2RR catalysts over different length scales.** Left: clustering of nanoparticles. Middle: transformation of nanospheres to nanocubes. Right: surface reconstruction of polycrystalline to (100)-like surface. Left and middle panels adapted from references 46 and 47. Right panel adapted with permission from *Langmuir* 2014, 30, 50, 15053–15056. Copyright 2014 American Chemical Society.

As mentioned in Section 1.2, Cu-based catalysts are prone to transformations during CO_2RR. Literature reports on three main structural transformations (Figure 1.3) characteristic for nanoparticles, nanostructured catalysts, and planar model surfaces. First, the nanoparticles undergo clustering.[46] Second, the nanoparticles smaller than 50 nm undergo geometrical transformations. For example, the nanospheres transform into nanocubes within 7 minutes.[48] Third, polycrystalline surfaces undergo surface reconstruction to (100)-rich facets.[47]

Length scales, at which these structural transformations occur, expand over five orders of magnitude differences. Such a length scale, generalized to the macroscopic length scale, equalizes to the differences between the sharp pencil point and the approximate length of the football pitch. This imposes constrains for the microscopy techniques used to study *in situ* structural evolution. Transformations at the micrometer scale are observable by electron microscopy, whereas surface reconstructions at atomic scale are resolvable by scanning probe microscopies (SPM). In particular, electrochemical scanning tunneling microscopy (EC-STM) stands out as the *in situ* microscopy technique with atomic resolution.

1.4 Thesis overview

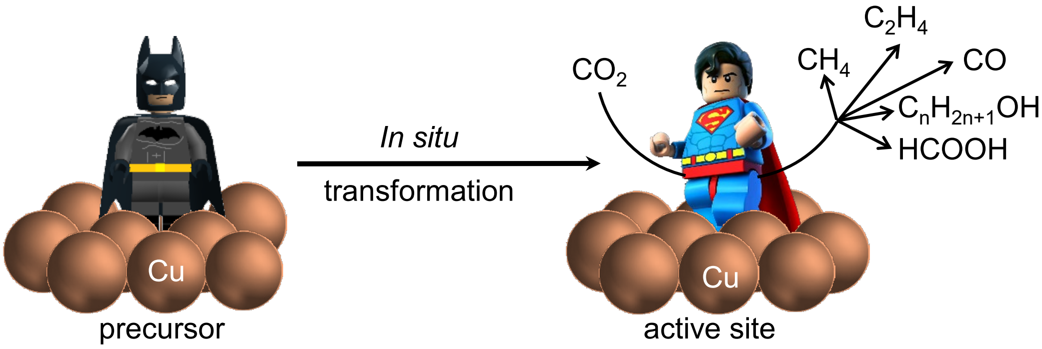

Figure 1.4 – ***In situ* evolution of Cu-based CO_2RR catalysts.** Cartoon illustrating the surface dynamics processes of Cu-based catalysts during CO_2RR. Examples of the transformations might be associated with activation, the formation of active sites, transformations related to chemical composition changes, and deactivation.

The literature overview presented above implies substantial transformations of Cu-based catalysts during CO_2RR (Figure 1.4). This thesis explores the surface physics processes behind *in situ* transformations. Cu-based catalysts are studied through a combination of three *in situ* surface science techniques: electrochemical scanning tunneling microscopy, electrochemical Raman spectroscopy, and quasi-*in situ* X-ray photoelectron spectroscopy.

Chapter 2 discusses the experimental methods used in this work. I first present microscopic and spectroscopic techniques, with the main focus on two main techniques: scanning probe microscopy and Raman spectroscopy. A broad overview of each of them is given through a summary of their basic principles, a report on the experimental set-ups that were installed during this project, and an in-detail review of the general workflow. I introduce complementary experimental techniques: quasi-*in situ* X-ray photoelectron spectroscopy, electrochemical characterization, and CO_2RR product analysis. Two model systems for *in situ* surface studies of Cu-based CO_2RR catalysts are compared: 44 nm-edge length nanocubes prepared by a colloidal-chemistry method and graphene-covered polycrystalline Cu surfaces.

Chapter 3 reports on the evolution of polycrystalline Cu surfaces during CO_2RR. *In situ* EC-STM studies reveal the formation of the (100) facet multilayers as the main structural evolution during CO_2RR. *In situ* electrochemical Raman spectroscopy shows that Cu oxide, formed upon ambient oxidation, rapidly reduces to metallic Cu as soon as CO_2RR potential is applied. These findings, supported by density functional theory (DFT) calculations, imply that the nanocuboids form upon a potential-driven re-organization of metallic Cu atoms.

Chapter 4 presents the study of the oxidation of Cu underneath a graphene overlayer. We focus on two main aspects: ambient oxidation and oxidation in contact with an electrolyte. This study allows us to understand the surface processes at play, and thus is essential for the interpretation of further *in situ* studies under CO_2RR conditions.

Chapter 5 explores how the nanocuboids form during CO_2RR. We compare Cu^0 nanocuboids presented in Chapter 3 with Cu_2O nanocubes prepared through electrochemical cycling. We show that nanocuboids and Cu_2O nanocubes are of different morphologies and chemical compositions. By elucidating the growth mechanism of the nanocubes during electrochemical cycling, we discard the hypothesis that nanocuboids form upon dissolution and electrodeposition, and we show the effect of chloride in this process.

Chapter 6 discusses the nanocuboid formation mechanism. EC-STM studies reveal that the atomistic processes of the nanocuboid formation resemble Cu/Cu(100) homoepitaxy. These results show that the nanocuboids are (100) facet multilayers (mounds). We speculate that multilayer mounds form upon reduction of (native) Cu_xO on any Cu catalyst regardless of its crystallinity, initial macroscopic shape, or chemical composition, therefore pointing to mounds as CO_2RR active sites.

Chapter 7 summarizes the main results of the thesis.

Setting the stage Part I

2 Experimental methods

Most of our current understanding of heterogeneous catalysis is based on static and *ex situ* characterization studies of the materials before and after the catalytic reaction has taken place ("post mortem"). In the last years, the rise of *in situ* studies under operating conditions is helping the community to understand the dynamic nature of electrocatalysts across different length scales.

This thesis relies on the synergy of *in situ* microscopic and spectroscopic techniques: electrochemical scanning tunneling microscopy, electrochemical Raman spectroscopy, and quasi *in situ* X-ray photoelectron spectroscopy. *Ex situ* microscopy characterization was carried out using scanning electron microscopy, atomic force microscopy, and STM at the air/solid and at the liquid/solid interface; *ex situ* spectroscopy was carried out using Raman spectroscopy; electrochemical characterization was carried out using basic electrochemical methods (cyclic voltammetry, chronoamperometry, and linear sweep voltammetry); CO_2RR products were analyzed using (online) high-performance liquid chromatography and gas chromatography. This synergistic approach allows us to characterize the model system over different length and depth scales.

In this Chapter, we present the basic principles of each technique, outline their advantages and disadvantages in the context of Cu-based CO_2RR catalysis, and describe the set-ups and workflows. Additionally, I introduce two model systems investigated during this work.

2.1 Microscopy

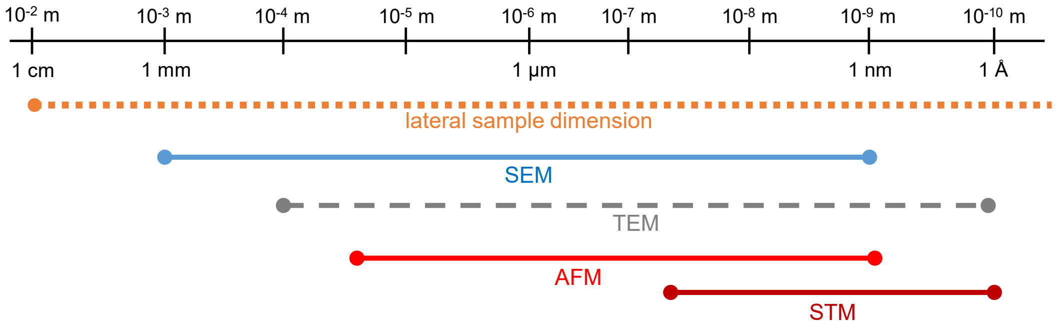

Figure 2.1 – **Length scales and microscopy ranges.** Overview of the imaging ranges for different microscopy techniques together with the lateral sample dimensions. The dots on the right of each line denote the highest theoretical resolution limits for the corresponding techniques. Adapted from reference 49.

Introductory discussion on the length scales involved in surface evolution of Cu-based CO_2RR catalysts entails a synergistic microscopy approach, which can overcome not only resolution limits (Figure 2.1), but also the disadvantages of each technique. This work relies on scanning probe microscopy techniques based on the simultaneous raster scans over the surface, detection, and recording of the physical quantity changes at each point.

2.1.1 Scanning probe microscopies

Scanning probe microscopies rely on the interactions between a physical probe and the sample surface: atomic force microscopy (AFM) employs the forces acting between the tip and the sample, whereas scanning tunneling microscopy (STM) exploits the phenomenon of quantum tunneling. These techniques can go beyond the diffraction limit, unlike traditional optical and electron microscopies. SPM stands out as the microscopy with the highest possible resolution allowing the visualization of surface atoms.

For both AFM and STM, the interactions are only at tip-sample distances below 10 nm. Therefore, SPM operation requires angstrom control over the lateral and vertical tip movement. SPM set-ups consist of the following components: sharp and stable tips; coarse positioning system allowing the user to bring the tip a few micrometers from the sample surface; piezo tubes as the main actuator moving the tip across the surface; voltage and/or current amplifiers; feedback controllers that maintain either constant interactions (as in static AFM mode and a constant-current mode in STM) or constant probe-sample distance (more precisely, constant amplitude and constant force gradient for dynamic AFM mode and constant-height mode in STM); efficient vibration isolation.

Atomic force microscopy

AFM employs the interactions between the probe and the surface indirectly detected from the probe's deflection. In the simplest approximation, the probe-surface interactions are

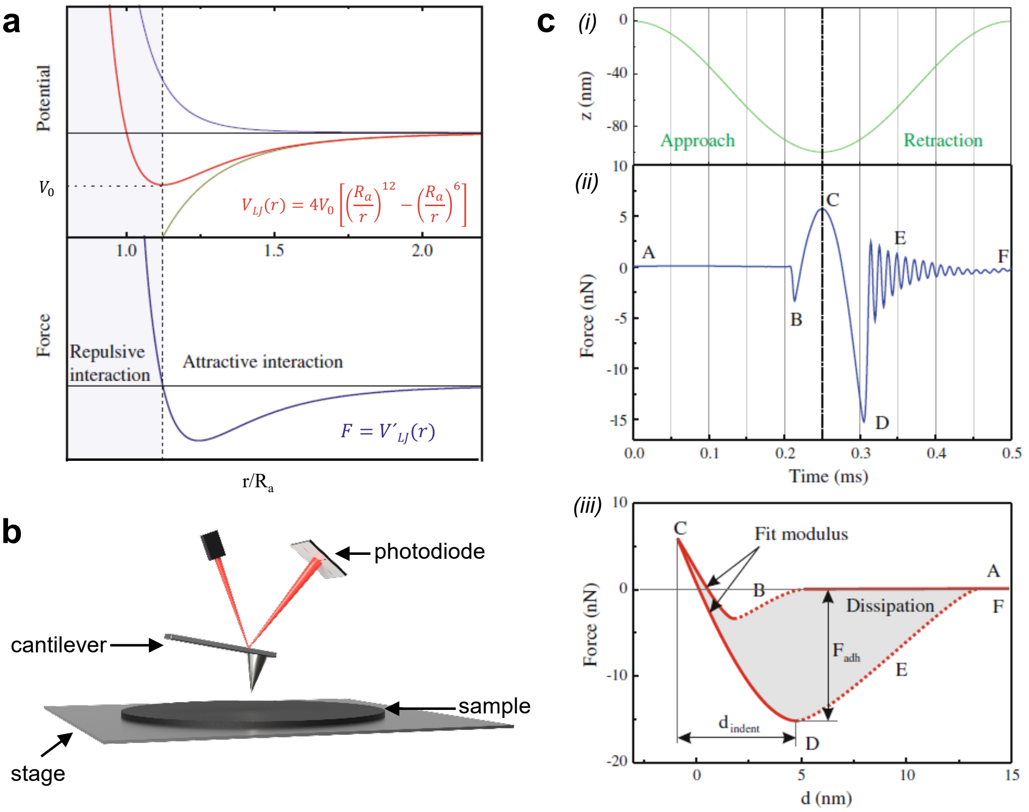

Figure 2.2 – **Atomic force microscopy.** (a) The Lennard-Jones potential as a model potential for a tip-sample interactions together with the corresponding forces. The green and the blue lines show the attractive and the repulsive potentials, respectively. (b) Scheme of the beam deflection. (c) The principles of the PeakForce tapping mode. (i) Sinusoidal change of the z-position of the tip. (ii) Tip-sample force as a function of time. (iii) Tip-sample force-distance curve. (a) and (c) adapted from reference 49, (b) adapted from reference 50.

described through the Lennard-Jones potential (Figure 2.2 a)):

$$V_{\mathrm{LJ}}(r) = 4V_0\left[\left(\frac{R_a}{r}\right)^{12} - \left(\frac{R_a}{r}\right)^{6}\right], \tag{2.1}$$

where V_0 is the depth of the potential well, R_a is the distance at which $V_{\mathrm{LJ}}(r) = 0$, and r is the distance between the atoms. The first term describes strong repulsive interactions at short distances, while the second term describes attractive forces (Van der Waals) at large distances.

The tip-sample interactions strongly vary on the atomic scale. AFM thus relies on sharp tips that are soft in the vertical direction and rigid in lateral directions (cantilevers, Figure 2.2 b)). The main properties of the rectangular $w \times L \times t$ cantilever are the stiffness $k = \frac{Ywt^3}{4L^3}$, eigenfrequency $f_0 = 0.162\frac{t}{L^2}\sqrt{\frac{Y}{\rho}}$, quality factor Q, the chemical and structural compositions. The cantilever holds the sharp, small-radius tip. Finally, deflections are measured through the deflections of a laser beam from the reflective backside of the cantilever.

AFM can be operated in several modes, out of which the tapping mode is the most common one. In tapping mode, the cantilever oscillates at the frequency close to f_0. As the tip taps each scan point, the resonance frequency change modifies the vibration amplitude and the phase, which are used as the parameters for a feedback loop.

Each cantilever oscillation can be described by the tip-sample force-distance curve, where the force is deduced from the cantilever deflection. Such curve consists of six regions characteristic for approach and retraction (Figure 2.2 c)). As the tip approaches the surface, the attractive forces increase (cantilever bending up from A to B) until the tip snaps into the contact (point B) and enters the repulsion force regime (point B); the forces, now repulsive, further increase until reaching the maximal (peak) force at point C. As the tip retracts from the surface, the repulsion forces turn into attractive adhesion force until reaching the point of the maximal attractive force. The tip then snaps out of contact, and the cantilever oscillates as a free oscillator. If the curves are obtained for each oscillation cycle and at each point of the sample, their analysis provides us with the maps of mechanical properties (dissipation energy, Young modulus, elasticity) and adhesion. These maps can be qualitative or quantitative (if performing the calibration of the cantilever and detector sensitivity, so that the cantilever deflection can be converted to force). However, this approach remains hindered for tapping mode because the cantilever's rapid oscillations back-and-forth along the force-distance curve translates into the maps of the average interactions in the phase channels. Phase channel images thus contain information on materials properties, but lack of information on the force-distance curves per pixel hinders the contrast interpretation.

This thesis exploits an advanced version of the tapping mode that allows force mapping, *i.e.*, PeakForce tapping mode. The key technical modifications are: sinusoidal excitation rather than linear; off-frequency operation at frequencies of several thousand Hz; direct extraction of the peak force; force-driven feedback loop (operation at constant forces in piconewton range). Simultaneous force control and force mapping allow the highest resolution AFM imaging with the piconewton imaging forces, preservation of tip and sample integrity, acquisition of thousands of force-distance curves per second, and on-the-fly analysis of the topography and material's properties maps. Additionally, PeakForce mapping is coupled with an automatically optimized feedback loop (ScanAsyst), allowing map acquisition within a predefined noise level.

The main benefits of AFM characterization using a combination of the fast-scanning AFM scanner and PeakForce mapping are: nondestructive characterization with control over the forces in the piconewton range; simultaneous acquisition of the topography and the material's property maps with indirect implications on the chemical contrast; high scan rates; automatic control over the gain parameters. The main limitations of AFM are the maximal scan-size of $32 \times 32\ \mu m^2$ which is further limited to $10 \times 10\ \mu m^2$ surface areas at realistic scan rates (1 Hz), and the constraints related to high surface roughness.

AFM has been rarely utilized for characterization of the Cu-based CO_2RR catalysts. This is mostly a consequence of the challenges related to the AFM operation, especially for the rough, nanostructured catalysts and nanoparticles. The success of AFM experiments is determined by several equally important factors: the vibration isolation, the sample immobilization, the sample roughness, the choice and the state of the cantilever, and the imaging parameters.

Experimental details

Set-up. The AFM set-up consists of a Dimension FastScan scanner, digital camera, motorized chuck coupled with NanoScope Controller V, high-voltage amplifier, and Icon Stage Controller FS. The vibration isolation system consists of Stacis 2100 (TMC) active vibration cancellation system, Newport I-2000 system (passive vibration system), and acoustically shielded box.[50]

Workflow. The samples were immobilized either using the vacuum chuck or gluing them on the metal puck (Micro-Tec D12 double-sided adhesive tape) mounted on a magnetic stage. For G-Cu samples, immobilization on the metal puck was used. Typical imaging parameters relied on ScanAsyst-optimized gains, scan rates between 0.7 and 4 Hz, imaging forces below 400 pN, frequency of 8 kHz, and amplitudes below 25 nm. All images reported in this thesis were obtained in PeakForce mapping mode using FastScan-B (Bruker) probes (nominal f_0 =450 kHz, k =1.8 N m^{-1}, and tip radius of 5 nm).

Image analysis. AFM images were post-processed using WSxM software.[51] Post-processing included plane fitting and equalization.

(Electrochemical) scanning tunneling microscopy

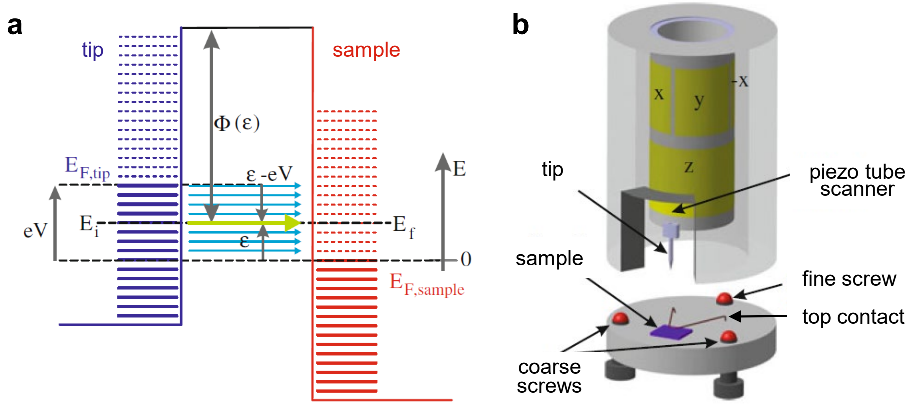

Figure 2.3 – **Scanning tunneling microscopy.** (a) Energy diagram of tip and sample states for the case of positive bias voltage. (b) Scheme of a Nanoscope STM. (a) and (b) adapted from reference 49.

Scanning tunneling microscopy (STM) employs the phenomenon of quantum tunneling. The sharp, metallic tip is firstly brought 0.5 nm–1 nm away from the conductive surface. When a potential is applied between two, the electrons from the tip tunnel to the sample (or vice versa, depending on the bias voltage polarity).

STM imaging is based on the fact that the tunneling current is an exponential function of tip-sample distance. Following the Tersoff-Hamman adaptation of the Bardeen model for planar metal-insulator-metal tunneling junctions,[52,53] the tunneling current in STM is described by:

$$I_{\mathrm{t}}(V) \propto e^{-2\kappa \cdot d} \int_0^{eV} \rho_s(E, x, y) \cdot \rho_t(E - eV)\, dE,$$

where $\kappa = \sqrt{(\frac{m_e}{\hbar^2}) \cdot (\phi_s + \phi_t)}$ depends on the work functions of the sample (ϕ_s) and the tip (ϕ_t), d is the tip-sample distance, ρ_s is the local density of states of the sample at the position (x, y), and ρ_t is the local density of states of the tip, V is the applied bias voltage, and eV is the corresponding energy shift. The first factor reveals exponential sensitivity of the tunneling currents on the tip-sample distance allowing the sub-angstrom precision on the vertical movement and lateral resolution down to atomic scale. The second factor relates the tunneling current with the density of states of the tip and the surface. It follow that STM images are the contours of constant tunneling probability rather than topography or constant electron density maps.

Even though I_{t} depends on the sample's density of the states, chemical information in STM images is heavily masked by topography effects. Thus, interpretation of STM images relies on: (i) the knowledge of the sample composition, preparation and history; (ii) supplementary images of the atomic lattices; (iii) image appearance (*e.g.*, image fuzziness suggests the mobility of the surface species); (iv) complementary spectroscopy studies. Additional information might be given by the shape and apparent heights. For example, island shape indirectly implies the crystallinity of both homoepitaxially grown islands and the underlying substrate.

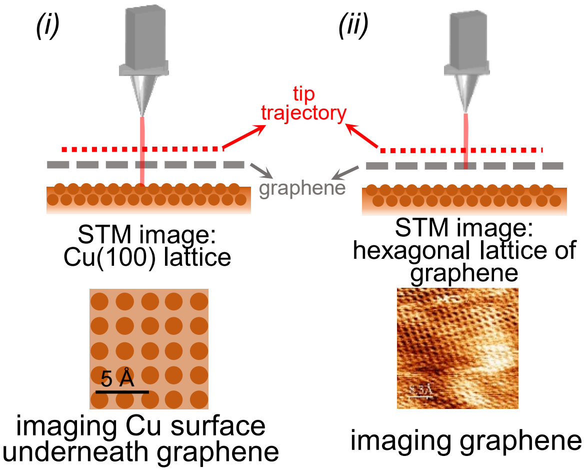
(i)
(ii)
tip trajectory
graphene
STM image: Cu(100) lattice
STM image: hexagonal lattice of graphene
5 Å
imaging Cu surface underneath graphene
imaging graphene

Figure 2.4 – **Scanning tunneling microscopy: graphene-covered polycrystalline Cu.** Scheme of STM imaging of G-Cu. By changing the imaging parameters, one images (i) Cu surface (*e.g.*, Cu(100) atomic lattice) or (ii) graphene overlayer (*e.g.*, hexagonal lattice of graphene).

STM has been widely used to study adsorbates, self-assembled layers, and 2D materials supported by (semi)conductors. In all three cases, the system can be considered as a vertical duplex, where changes in the bias voltage allow visualization of either the substrate or the overlayer. To illustrate this concept, I take graphene-covered polycrystalline Cu surface as an example (Figure 2.4 a)). By changing the imaging parameters, one images either Cu surface or graphene layer. Therefore, one can visualize either atomic lattice of Cu surface or atomic lattice of graphene on small scale STM images (scan sizes $\leq 20 \times 20$ nm^2).

EC-STM allows imaging the surfaces under realistic electrochemical conditions. The EC-STM set-up consists of a conventional STM set-up coupled with an electrochemical cell and a bipotentiostat (Figure 2.5). Additionally, coated tips are used to minimize interference between the tunneling currents (typically in 50 pA–10 nA range) and (non-)faradaic currents, where the (non-)faradaic currents are associated with electrochemical reactions (the charging-discharging processes). This condition is especially limiting for EC-STM studies of Cu-based CO_2RR catalysts with high overpotentials. EC-STM experiments were thus conducted at low overpotentials.

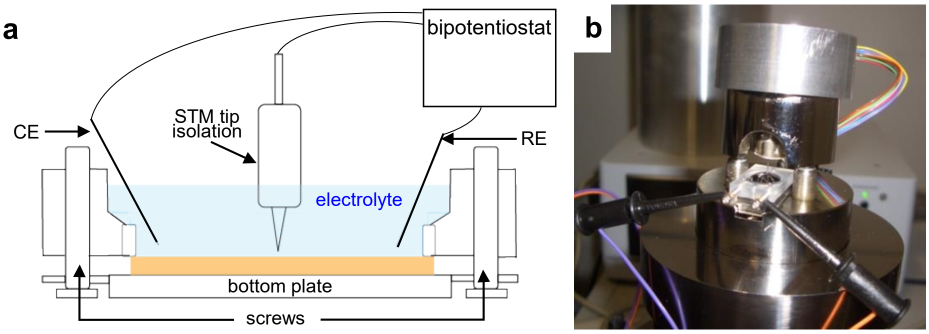

Figure 2.5 – **Electrochemical scanning tunneling microscopy.** (a) Scheme of EC-STM set-up. (b) Photo of EC-STM set-up used in this work.

The advantages of STM are: atomic resolution, high scan rates, and the possibility to study both air/solid and liquid/solid interfaces. The challenges are the sample and tip preparation, the maximal scan size ($\approx 800 \times 800$) nm^2 allowing studies of local environments, thermal drift challenging continuous tracking of a pre-selected surface area,[54] and the requirements for flat (model system) surfaces.

Experimental details

Set-up. STM characterization was performed on a MS-10 STM (Bruker) coupled with a NanoScope Controller V and a high-voltage amplifier. The set-up was mounted on the optical table suspended on Stacis 2100 (TMC) active vibration cancellation system and Newport I-2000 system (passive vibration system). For EC-STM experiments, as-assembled STM was connected to NanoScope Universal Potentiostat. An electrochemical cell (Bruker) was fitted with two Pt wires which served as a pseudo-reference (RE) and counter electrodes (CE). All STM and EC-STM experiments were performed in a constant-current mode at room temperature.

Workflow. Ex situ STM characterization was conducted at the air/solid interface or at the liquid/solid interface, where the *liquid* in the latter term refers to a poorly conductive, organic solvent such as octanoic acid. STM tips were prepared by mechanical cutting from a Pt/Ir wire (80%/20%, diameter 0.25 mm). Several (x, y) position along the sample were imaged using typical imaging parameters: V_{bias} =(−1 mV)–(−500 mV) and I_{t} =20 pA–

1.5 nA. This procedure provides an overview of the characteristic topography features.

The EC-STM tips were electrochemically etched from tungsten wire (diameter 0.25 mm) in 2 M KOH solution, rinsed with water, dried, and subsequently coated by passing the tip through a lamella of hot-melt glue. The apparatuses for etching and tip insulation were similar to those reported in reference 55. A set of 10 freshly prepared EC-STM tips was tested in air on HOPG: this step allows pre-selection of the EC-STM tips of the acceptable quality prior to the EC-STM experiment.

STM experiments both under open circuit potential (OCP) and under electrochemical control were conducted in the EC-STM cell. Surface imaging was conducted under chronoamperometric conditions (constant-potential polarization at low overpotentials). Since we aimed to study *in situ* structural changes, the same surface area was imaged for as long as the system was stable, *i.e.*, between several minutes and several hours. In the case of instabilities, the tip was re-approached at another x, y_1 position.

Image analysis. STM images were processed using WSxM software[51] with further details reported in Chapter 6.

2.1.2 Scanning electron microscopy

SEM was used complementing *ex situ* scanning probe microscopy characterization. The main advantage of SEM over scanning probe microscopies is that it allows us to characterize: (i) surface areas larger than 10×10 µm^2 and (ii) samples that are considered too rough for SPM. Additionally, I acknowledge Dr. Cyril Cayron for electron backscattered diffraction maps obtained at Thermomechanical Metallurgy Laboratory, EPFL.

Experimental details

Set-up. SEM micrographs, presented in Chapters 5 and Appendix C, were obtained on Gemini 300 (Zeiss) microscope installed in the Interdisciplinary Center for Electron Microscopy, EPFL.

Workflow. G-Cu and Cu samples, that were exposed to the electrochemical treatments (electrochemical cycling in Chapter 5) prior to SEM imaging, were thoroughly rinsed with Milli-Q water, dried with nitrogen flow, and transferred in vacuum-sealed bags. To minimize sample oxidation, the sample preparation and SEM characterization were carefully scheduled so that the samples were imaged within 30 minutes after the sample preparation. SEM images were obtained using InLens secondary electron detector and an acceleration voltage of 3 kV.

2.2 Spectroscopy

Spectroscopy is used to identify the chemical nature of the CO_2RR-active Cu phase. X-ray photoelectron spectroscopy (XPS) spectra reflect the chemical composition of $\approx$2 nm deep surface layers, whereas Raman spectra contain information collected over the first 15 nm

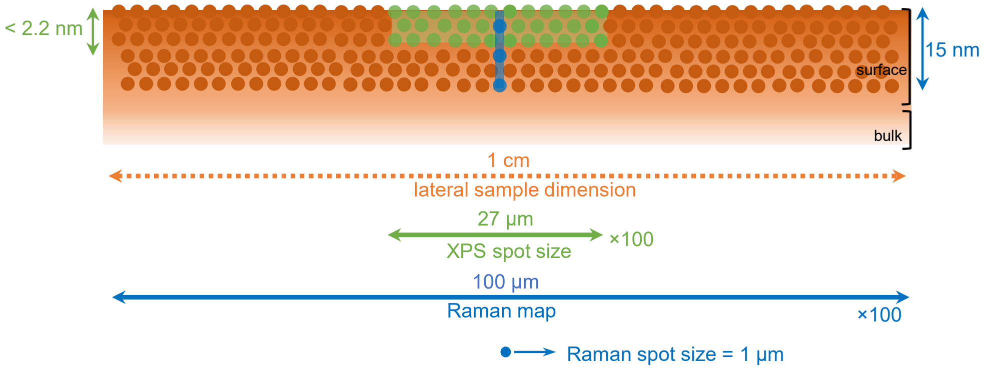

Figure 2.6 – **Surface spectroscopy: length and depth scales.** The sizes of a X-ray beam and Raman laser beam are scaled with respect to the sample dimension.

of the surface. XPS is thus considered as a near-surface and Raman spectroscopy as a far-surface sensitive technique.

2.2.1 Raman spectroscopy

Raman spectroscopy is an optical spectroscopic method relying on the inelastic scattering of the incoming light from a molecule or surface (Figure 2.7 a)). An incident photon with energy $E_i = E_{\text{laser}}$ interacts with the sample by exciting molecular/solid-state vibrations. The outcoming photon has energy $E_f < E_{\text{laser}}$ if the system undergoes transition from the ground to excited vibrational state (Stokes Raman scattering) or $E_f > E_{\text{laser}}$ if the system is originally in an excited vibrational state and undergoes a transition to the ground state (anti-Stokes scattering).

Most photons scatter elastically. Spontaneous Raman scattering is thus a very weak process, with Stokes scattering being more likely and more intense than Anti-Stokes scattering. Raman scattering can be enhanced through resonance Raman, in which the excitation wavelength coincides (*i.e.*, is in resonance) with an electronic transition of the material, or through surface-enhanced Raman, which exploits a combination of electromagnetic and chemical enhancement. Fluorescence, as a side-process with the intensity six orders of magnitude higher than the Raman scattering, has to be suppressed in both cases. The most user-friendly approach for fluorescence suppression is coupling the spectrometer with a confocal microscope (Figure 2.7 b)).

Raman spectra of solid-state samples contain information on the material properties. In particular, it is possible to deduce the chemical composition from the positions of Raman bands, stress/strain from the respective changes in the Raman peak positions, the crystal quality from the peak widths, and quantitative information on the composition from the peak intensities. To qualitatively illustrate these correlations, I take resonant Raman spectroscopy of G-Cu as an example. A Raman spectrum of the fresh G-Cu displays the Raman spectrum of a perfect graphene—the absence of the defect-induced D band at $\approx 1350\,\text{cm}^{-1}$, together with the G band at $\approx 1600\,\text{cm}^{-1}$ and the 2D band at $\approx 2700\,\text{cm}^{-1}$ as two characteristic graphene bands. Large background corresponds to the photoluminescence of the metallic copper underneath graphene[56] and is thus characteristic

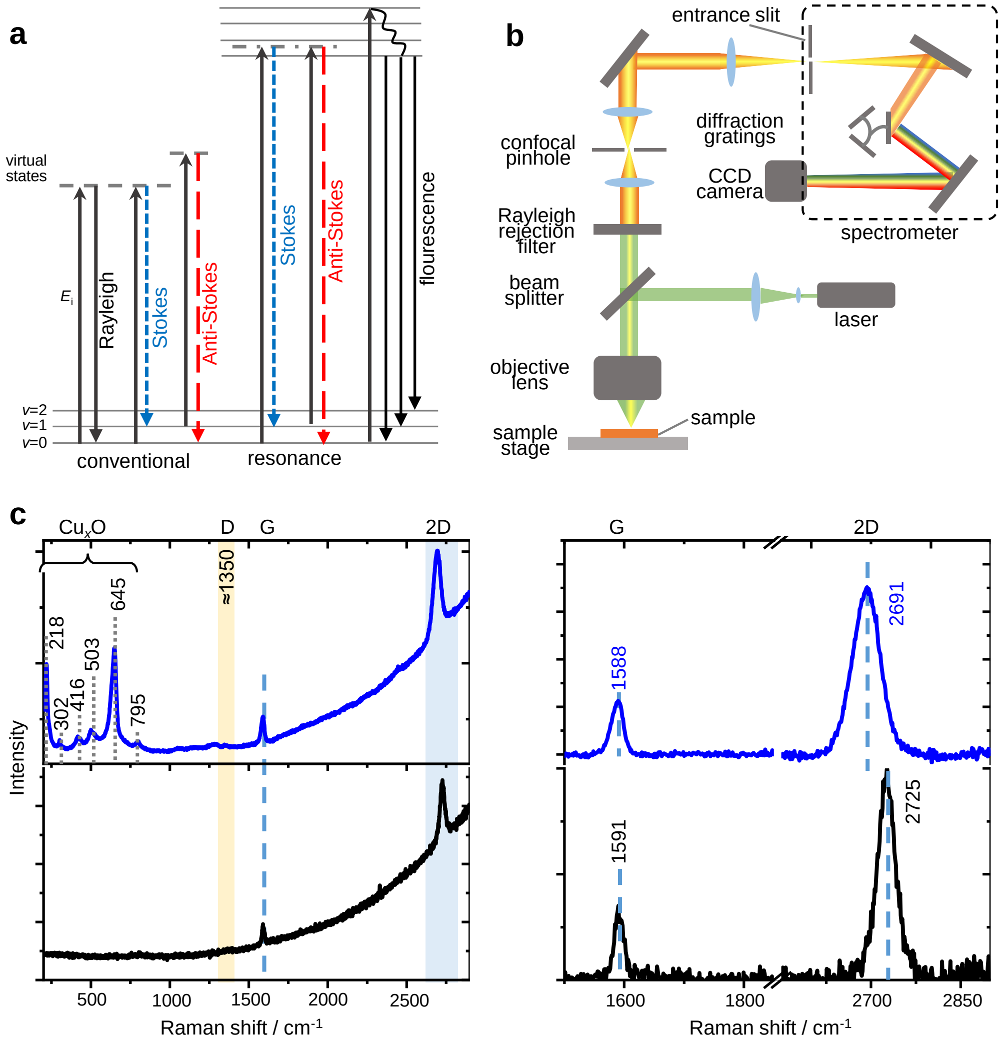

Figure 2.7 – **Raman spectroscopy.** (a) Scheme of Raman scattering. (b) Scheme of the confocal Raman spectroscopy. (c) Representative Raman spectra of the unoxidized G-Cu and oxidized G-Cu together with the corresponding G and 2D bands of the same samples. Left: as-obtained spectra with the photoluminescence background. Right: background-corrected spectra.

for G-Cu samples regardless of the Cu oxidation state. The same spectroscopic signatures together with the Cu$_x$O bands are present on the Raman spectrum of the air-oxidized G-Cu samples. Cu$_x$O bands are situated in the 200–1000 cm^{-1} spectral region: Cu$_2$O peaks[57,58] at 218 and 635 cm^{-1} and CuO peaks at ≈302 and 619 cm^{-1}. To the best of our knowledge, the peaks at 416, 503, and 795 cm^{-1} are currently unassigned for *ex situ* Raman spectrum of G-Cu and mostly likely are the higher-order modes of Cu$_x$O.[59] Due to the fact that this spectrum was obtained under *ex situ* rather than *in situ* conditions on SERS-inactive substrate[60], we rule out that these *ex situ* Raman peaks on G-Cu are due to the CO-containing CO$_2$RR intermediates. Finally, the graphene's G and 2D peaks are highly sensitive to the interaction between graphene and the substrate (*e.g.*, charge transfer from one to another), crystallographic orientation of the underlying Cu,[61] strain along the graphene overlayer.[62]

Experimental details

Set-up. Raman spectroscopy experiments were performed on an inVia confocal Raman spectroscope (Renishaw) controlled by WiRE 4.4 software (Renishaw) and installed in the Facility for Crystal Growth, EPFL. The incident laser wavelengths was 488 and 532 nm. *Ex situ* spectra were collected using 50× and 100× objectives (Leica) and detected using an electron multiplying charge-coupled device camera.

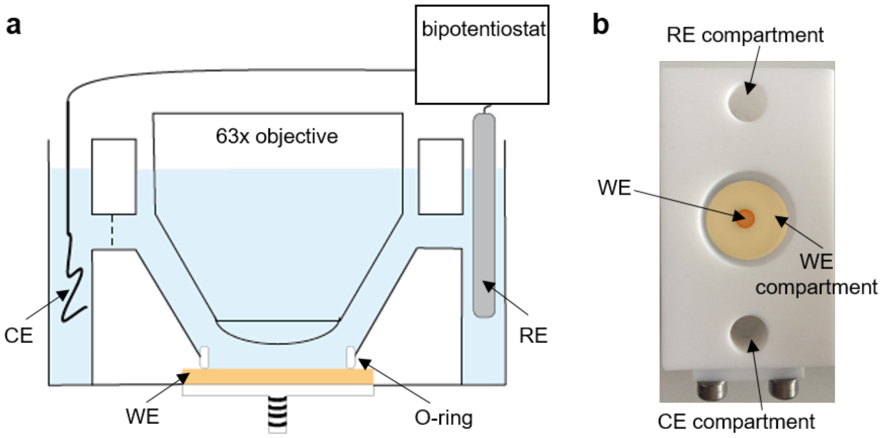

Figure 2.8 – ***In situ* Raman spectroscopy set-up.** (a) Scheme of *in situ* Raman set-up. (b) Photographs of the electrochemical cell used for *in situ* Raman spectroscopy.

In situ Raman spectroscopy experiments were performed using 63× water immersible objective (Leica) and a home-built, three-compartment electrochemical cell made of Teflon. The cell design was adapted from the reference 63. G-Cu (Graphenea) or (electrochemically treated) polycrystalline Cu foils were used as the working electrodes (A_{geo} =0.28 cm^2), miniature Ag/AgCl electrode (ProSense B.V.) or Pt pseudo-RE were used as the RE, a coiled Au wire was used as the CE. 0.1 M CO_2 saturated $KHCO_3$ was used as electrolyte. The cell was controlled using a VersaSTAT 4 (Ametek) potentiostat coupled with VersaStudio software.

Workflow. Before each experiment, the spectroscope was calibrated using a Si crystal (521 cm^{-1}). The laser power was ≤1 mW. Spectroscopic data over the micrometer scale were obtained by collecting Raman maps. The maps were collected either in the point mapping mode with the lateral steps of 1 µm on the surface areas of 5×5 µm^2 or in the StreamLine mapping mode with the laser focused in a line. The accumulation times varied between 5 and 30 seconds.

Data analysis. Raman peaks were fitted by a Lorentzian function on pre-defined spectral ranges that were pre-corrected for the linear background. For graphical representation, the spectra were corrected for the background that was fitted using either Intelligent fit (WiRE software, Renishaw) or asymmetric least square smoothing baseline algorithm with the smoothing factor 6 (OriginPro).

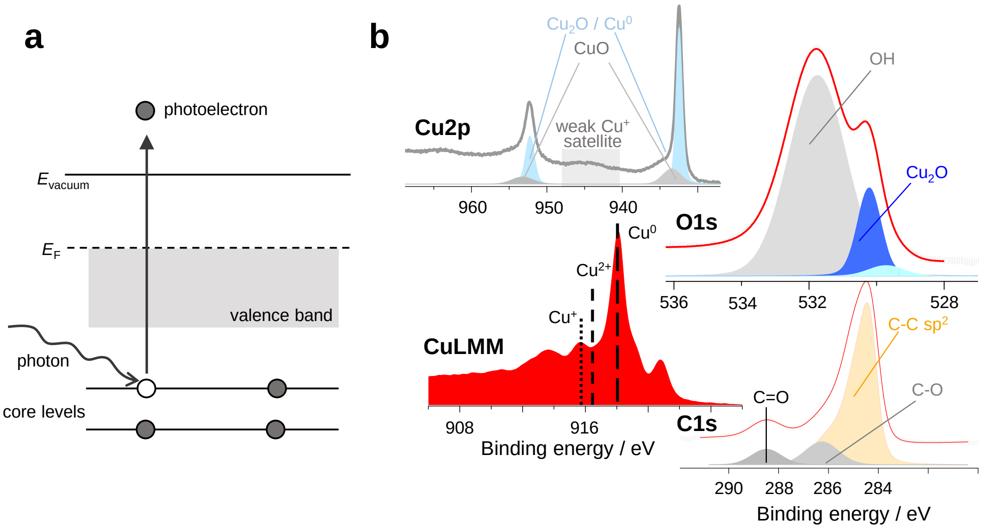

Figure 2.9 – **X-ray photoelectron spectroscopy.** (a) Scheme of the photoemission principle. (b) XPS characterization of G-Cu: the analysis of $Cu2p_{3/2}$, CuLMM, O1s, and C1s spectra.

2.2.2 X-ray photoelectron spectroscopy

X-ray photoelectron spectroscopy is a photon-in-electron-out spectroscopy that enables the chemical composition analysis of a solid's outer surface (within first 2 nm for Cu surface).[64] It relies on the photoelectric effect (Figure 2.9 a)): X-rays ionizing radiation with energy $h\nu$ ejects the electron from the atom inner shell. As-emitted electrons, photoelectrons with kinetic energy E_{kin}, reach the analyzer. The electron binding energy is then calculated from the photoelectric effect equation:

$$E_{\mathrm{binding}} = h\nu - (E_{\mathrm{kinetic}} + \phi),$$

where ϕ is the work function of the sample corrected by the instrument work function due to the contact potential. Additionally, the decay of the electrons from the higher-energy level to the inner-shell vacancy, created upon photoemission, results in energy emission released in the form of a photon or transferred to another electron (Auger electron). Both photoelectrons and Auger electrons are observable in XPS spectra.

XPS is a near-surface sensitive technique widely used for both qualitative and quantitative analysis of the surface composition and studies of the local chemical environment of the respective elements. Analysis is stepwise: one firstly collects the spectrum over the whole energy range, selects the energy ranges of the interest, and then, collects the high-resolution spectra in each range. For the graphene-covered polycrystalline Cu, we aimed to study the oxidation state of Cu surface that underwent structural changes by collecting $Cu2p_{3/2}$, CuLMM Auger, and O1s spectra (Figure 2.9 b)), where CuLMM spectra are highly sensitive to Cu oxidation.[65,66] The conclusions on the oxidation state were deducted from the analysis of all three spectra. Graphene stability was examined through analysis of the C1s peak.

Short inelastic mean free path of the photoelectrons in ambient conditions limit XPS measurements to the UHV environment. Quasi *in situ* XPS thus indirectly addresses the questions on the chemical composition of the species present on the sample after the reaction, while relying on stepwise sample transfer from the electrochemical cell to the UHV environment and XPS chamber. Transfer through an air-free environment is of great importance for Cu-based CO_2RR catalysts that are highly prone to oxidation, recently highlighted in a benchmark report on the protected transfer of polycrystalline Cu from the electrochemical cell to XPS chamber.[67] An ideal solution is coupling the electrochemical system with the XPS system, so that the samples electrochemically prepared in oxygen-free environment are transferred through the UHV transfer system to the XPS chamber.

Experimental details

The XPS experiments were conducted during a research visit to the group of Professor Klaus Kern at Max-Planck Institute for Solid State Research, Germany in collaboration with Dr. Patrick Alexa and Dr. Rico Gutzler. Dr. Fernando Cometto performed the data analysis.

Set-up. The samples were prepared in a home-built UHV-electrochemistry transfer system (Figure 2.10 a)), further details reported in references 68 and 69). Electrochemical sample preparation was carried out in a single-compartment cell with the working electrode in the hanging-meniscus configuration, while directly coupled to the transfer chamber. This set-up allows the electrochemical experiment in the controlled atmosphere (here, in CO_2 atmosphere). The samples were transferred from the UHV-electrochemistry system to XPS chamber by using a vacuum suitcase (Ferrovac). The suitcase (Figure 2.10 b)) consists of a small vacuum chamber ($p = 10^{-9}$ mbar) that accommodates two samples and an ion pump (NexTorr D-100-5, Ferrovac) running on batteries. The XPS characterization was conducted on a commercial Kratos AXIS Ultra system with a monochromatic Al Kα source ($h\nu$ =1487 eV).

XPS data analysis. All spectra were referenced against the Cu^0 in Cu2p spectra at 932.6 eV.[70] The peaks were fitted using Voight functions after Shirley type background subtraction.

2.3 Complementary techniques

2.3.1 Electrochemical characterization

Electrochemical methods employ the measurements of potential, current, or charge to characterize the electrochemical activity of a sample. Here, we employ cyclic voltammetry to characterize electrochemical behavior of the model system and constant-potential (chronoamperometric) polarization to perform CO_2RR electrolysis.

Experimental details

Set-up. Electrochemical characterization was performed in two electrochemical cells using either VersaSTAT 4 (Ametek) potentiostat or VSP-300 (BioLogic). We used a home-built, single-compartment, bottom-mount electrochemical cell made out of Teflon and a

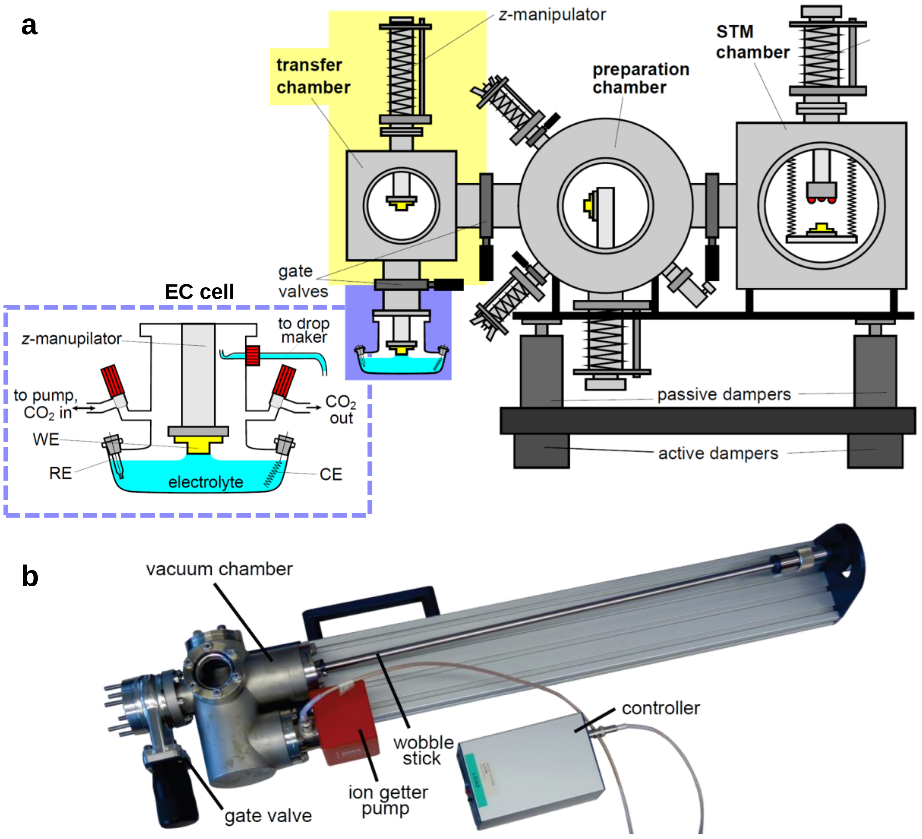
a
z-manipulator
STM chamber
transfer chamber
preparation chamber
EC cell
gate valves
z-manupilator
to drop maker
to pump, CO_2 in
CO_2 out
WE
RE
electrolyte
CE
passive dampers
active dampers
b
vacuum chamber
controller
wobble stick
ion getter pump
gate valve

Figure 2.10 – **Quasi *in situ* X-ray photoelectron spectroscopy set-up.** (a) Scheme of the UHV-electrochemistry set-up used for the preparation of the samples for XPS measurements. To avoid air exposure, the sample was prepared in the electrochemical cell and stored in the transfer chamber until the vacuum suitcase was mounted. The preparation and STM chambers were not used in these experiments. Inset: Electrochemical cell with the working electrode in the hanging-meniscus configuration. Two ground Teflon joints and the drop maker are not shown here. (b) Vacuum suitcase used to transfer the samples between UHV-electrochemistry system shown in (a) and XPS spectrometer. Adapted from references 68 and 69.

single-compartment, bottom-mount electrochemical cell (Graphene BM EC cell, redox.me). Ag/AgCl electrodes immersed in 3 M KCl solutions (ProSense) were used as the references electrodes, coiled Au or Pt wires were used as the counter electrodes. Before each experiment, the electrolyte was purged for at least 20 minutes with CO_2 or N_2 gas.

2.3.2 CO_2RR product analysis

In situ surface studies of CO_2RR electrocatalysts rely on the knowledge of their catalytic performance, including the catalytic activity and product selectivity. Here, we employ graphene-covered polycrystalline Cu as a model system (Section 2.4). Neither this model system nor similar systems covered with 2D materials have been studied as CO_2RR catalysts. We thus performed electrocatalytic characterization through quantitative product analysis.

Experimental details

Product analysis experiments were conducted during a research visit to the group of Professor Marc T.M. Koper at the University of Leiden, Netherlands in collaboration with Stefan J. Raajiman and Chunmiao Ye.

Set-up. CO_2RR electrolysis was carried out in a home-built, two-compartment electrochemical cell coupled with GC and controlled by SP-300 potentiostat (BioLogic) coupled with EC-Lab software (BioLogic). G-Cu was used as the working electrode, leakless Ag/AgCl reference electrode immersed in 3.4 M KCl (model ET072, eDAQ) was used as the reference electrode, coiled Au wire was used as the counter electrode. Each compartment accommodates 8 mL of the electrolyte, two compartments were separated by Nafion membrane. CO_2 gas (Linde, purity 4.5) was purged through both compartments during each experiment. The gas flow was regulated using High-Tech mass flow meter (E-7000, El-Flow series, Bronkhorst High-Texh B.V.).

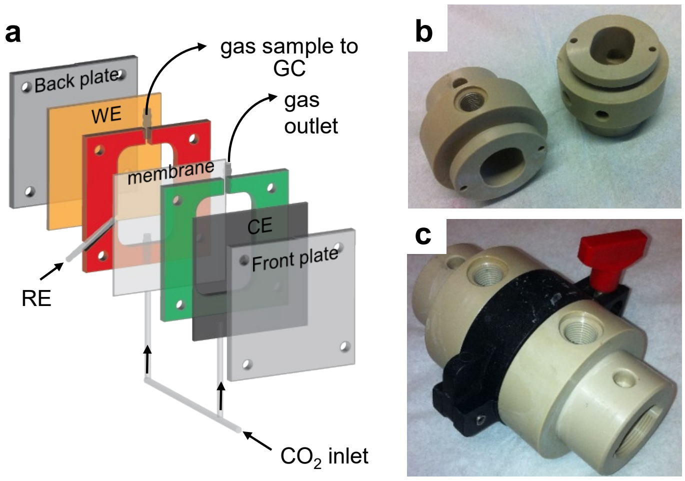

Figure 2.11 – **On-line gas chromatography set-up.** (a) Generic scheme of the electrochemical cell for on-line gas chromatography. Adapted from 35. Photographs of the (b) disassembled and (c) assembled electrochemical cell for on-line gas chromatography.

CO_2RR products were analyzed using gas chromatography (GC) and high-performance liquid chromatography (HPLC), where the liquid products were analyzed from the aliquots taken from the catholyte once the CO_2RR finished. GC consists of GC-2010 Plus Gas Chromatograph (Shimadzu), flame ionization detector, and thermal conductivity detector. Helium was used as the carrier gas through the gas chromatography columns (Rtx-1 column, Restek for thermal conductivity detector and ShinCarbonST Micropacked, Restek for flame ionization detector). A high-performance liquid chromatography system (Prominence HPLC, Shimadzu) was coupled with an autosampler (model Sil-20A, Prominence). 5 mM H_2SO_4 was used as the eluent; the oven temperature was kept at 45 °C; Aminex-75H was the column used for the analysis. More details on HPLC set-up can be found in reference 71.

Workflow. Before each experiment, the glassware and the electrochemical cell were either soaked in a 1 g L^{-1} acidic $KMnO_4$ solution or boiled in a mixture of concentrated H_2SO_4

and 30% H_2O_2. If soaked overnight in $KMnO_4$, the glassware and the cell were rinsed with Milli-Q water and then submerged in a diluted, acidic H_2O_2 solution. The final cleaning step is the same for both procedures: the glassware and the cell were three times boiled in Milli-Q water. Once the cell was assembled, CO_2 gas was purged for $\approx$ 20 minutes. The blank gas sample was analyzed by injecting gas aliquot from the cathodic gas compartment to GC, while keeping WE at open circuit potential. Also, the blank liquid phase sample was taken from the catholyte and later analyzed by HPLC. Uncompensated resistance ($\approx$40–50 Ω) was determined using potentiostatic electrochemical impedance spectroscopy. The potentiostat corrected for 85% of as-determined resistance value during each experiment and another 15% was post-corrected.

The electrolysis was carried out upon chronoamperometric (constant potential) polarization for $\approx$1 hour during which three gas aliquots were injected into GC using an automatic sampling loop. For the measurement at $-1.1\,\mathrm{V}$ vs RHE, the electrolysis was carried out for 20 minutes.

Data analysis. The steady-state currents, used for the calculations of the faradaic efficiencies, were calculated based on the average current between 5th and 60th minute. Average values of faradaic efficiencies and their standard deviations reported for each potential data point in Figure 3.2 were calculated based on three gas samples injected to GC at $\approx$10, $\approx$30, and $\approx$60 minutes.

2.4 Surface science studies: Model systems

Discussion on the surface science techniques presented in the previous Sections together with the introductory notes on the variety of the Cu-based CO_2RR catalysts underlines the importance of the model systems to be used for further *in situ* studies.

Two potential candidates were tested as model systems: i) 44 nm-edge length Cu nanocubes (NCs) prepared by colloidal chemistry method and supported by freshly cleaved highly oriented pyrolytic graphite (HOPG) and ii) graphene-covered polycrystalline copper surface. The suitability of both systems for scanning probe microscopy studies was analyzed through a stepwise characterization. In the first step, we evaluated the sample roughness and homogeneity by AFM. Samples that had surface features higher than 50 nm are discarded for (EC-)STM studies. Pre-selection based on homogeneity was motivated by the workflow of the STM experiments, where one starts with the small scale images (*e.g.*, 50×50 nm^2) and inspects the surface areas up to 800×800 nm by zooming-out. Such workflow limits STM observations to small surface areas without any possibility of pre-selection. If the object of the studies is not homogeneously distributed on the surface, an experimentalist has to rely on the trial-and-error method by blindly inspecting 800×800 nm^2 surface areas until finding the object. As we shall see in the example of CuNCs, this method is highly time-consuming and rarely successful. In the second step, we perform STM characterization at the air/solid interface. If characterization in both steps proved to be satisfactory for further *in situ* studies, the model system was characterized by cyclic voltammetry. Finally, CV characterization allows us to choose the optimal potential for EC-STM studies. For the studies of Cu-based CO_2RR catalysts, we chose the potentials in the potential region beyond the peak of Cu-oxide reduction.

Model system-1: Cu nanocubes on HOPG

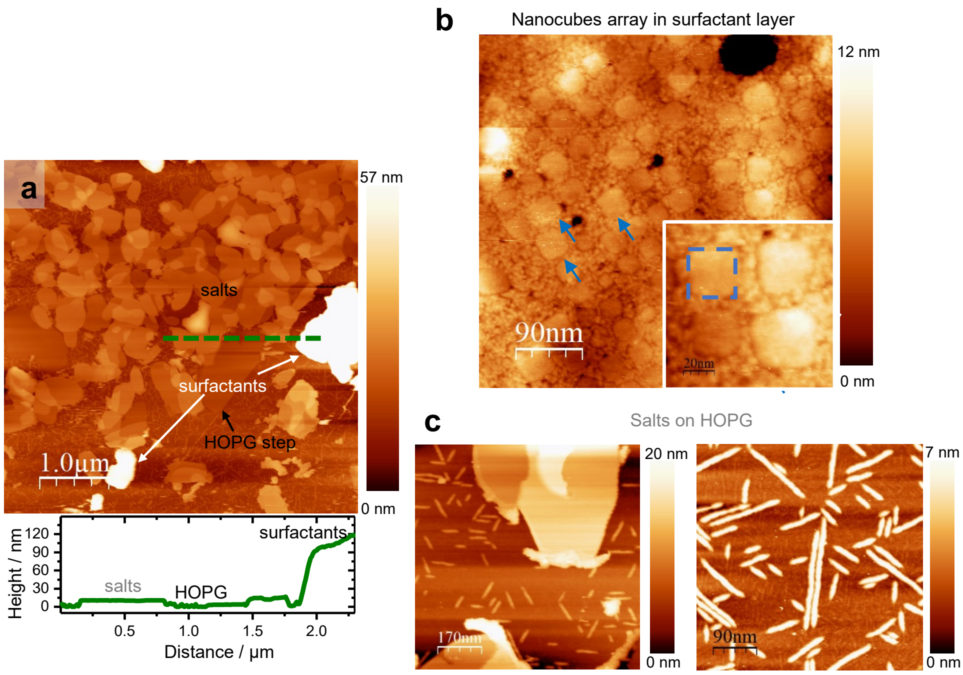

Figure 2.12 – **Model system-1: Cu nanocubes on HOPG.** AFM characterization of 44 nm-edge length CuNCs prepared by colloidal chemistry and supported by HOPG. (a) Large scale AFM image showing a 5×5 µm^2 surface area of HOPG substrate covered with salts and a layer of surfactants. (b) AFM image showing CuNCs. Blue arrows denote individual cubes. Inset: Nanocubes embedded in the surfactant layer. (c) AFM images of salts and self-assembled surfactant chains on HOPG.

The first model system was 44 nm-edge length CuNCs synthesized by colloidal chemistry in the group of Professor Raffaella Buonsanti (Institute of Chemical Sciences and Engineering, EPFL). Details on the synthesis can be found in reference 35 and 46. Looking back on the classification of Cu-based CO_2RR catalysts proposed by Nitopi *et al.*,[30] as-synthesized CuNCs belong to the class of nanoparticles. For the purposes of surface science studies, CuNCs were drop-casted on freshly cleaved HOPG.

AFM images of HOPG/CuNCs samples (Figure 2.12) reveal three features: HOPG substrate covered with self-assembled surfactant molecules, flat plateaus, and >60 nm-high irregular features. The plateaus are of irregular shape and have lateral sizes up to 1 µm and heights between 20 nm and 70 nm, depending on whether they grew on the bare HOPG surface (lower plateaus in dark brown hue) or on top of earlier-formed plateaus (higher ones in light brown hue). We speculate that these plateaus are salt deposits formed upon solvent evaporation. Irregular features randomly distributed along the surface and covering <10% of 5×5 µm^2 surface area are composed of the surfactant molecules embedding regular assemblies of the CuNCs. Such a sample is a typical example of an inhomogeneously functionalized sample unsuitable for SPM studies. Despite extensive efforts spent on optimization of the drop-casting protocol, we were not able to obtain homogeneous HOPG/CuNCs samples. Therefore, the CuNCs model system was discarded due to the difficulties encountered in producing reproducible and homogeneous samples.

Model system-2: graphene-covered Cu

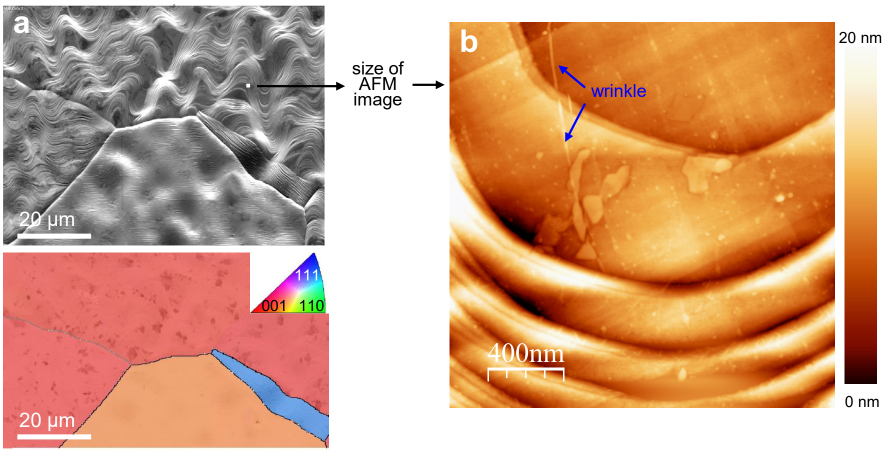

Figure 2.13 – **Model system-2: graphene-covered polycrystalline Cu.** Microscopy characterization of G-Cu. (a) SEM image of G-Cu together with the corresponding electron back-scattered diffraction map. (b) AFM image of G-Cu. Blue arrows denote graphene wrinkles.

The second model system was a polycrystalline Cu surface covered by a graphene monolayer (G-Cu). Here, we used G-Cu samples (1×1 cm^2) purchased from Graphenea. The graphene monolayer was directly grown on hydrogen-annealed polycrystalline Cu by chemical vapor deposition. As-grown graphene is of high quality: graphene covers $> 95\%$ and has a grain size up to 20 µm.

In general, graphene-covered metals are extensively used model systems for the studies of surface phenomena such as intercalation and molecular self-assembly.[72] The broad knowledge gained through the studies in ultra-high vacuum, in gas environments, and at the liquid/solid interface gives a unique pole-position to the G-Cu model system. For *in situ* surface science studies under CO$_2$RR conditions, we focus on the evolution of the Cu surface underneath graphene. The main advantages of G-Cu model system would thus be:

- anticorrosive properties of graphene protecting Cu surfaces toward oxidation[73] allowing us to avoid any pre-cleaning steps and to start with oxide-free polycrystalline Cu surfaces
- >1 mm-wide, flat Cu(100) crystalline grains[74,75] facilitating STM studies,
- confinement effects[76] at the interface between graphene and Cu.

Preliminary microscopy characterization reveals that the Cu surface underneath graphene is mostly composed of (100) crystalline grains with lateral sizes larger than 1 mm (Figure 2.13 a)). (100) grains are stabilized upon slow recrystallization in the presence of graphene.[75] The terraces expand over more than 100 nm with the spacings between single Cu atomic steps larger than 20 nm (Figures 2.13 a) and 2.14 c)). As indicated in the introductory paragraph of this Section, such surface is an example of a smooth and flat surface suitable for SPM studies. It should be noted that, even though graphene is not visible on the large scale SEM and SPM images, it is present and it crosses the Cu grain boundaries and step edges. Comparison of G-Cu model system with Cu(100) single crystal prepared upon sputtering-annealing cycles in UHV and electropolished polycrystalline Cu confirms the morphological similarity between G-Cu and Cu(100) single crystal surface prepared in UHV (Figure 2.14). Therefore, G-Cu model system is a unique substrate allowing *in situ* surface science studies on Cu(100) surfaces.

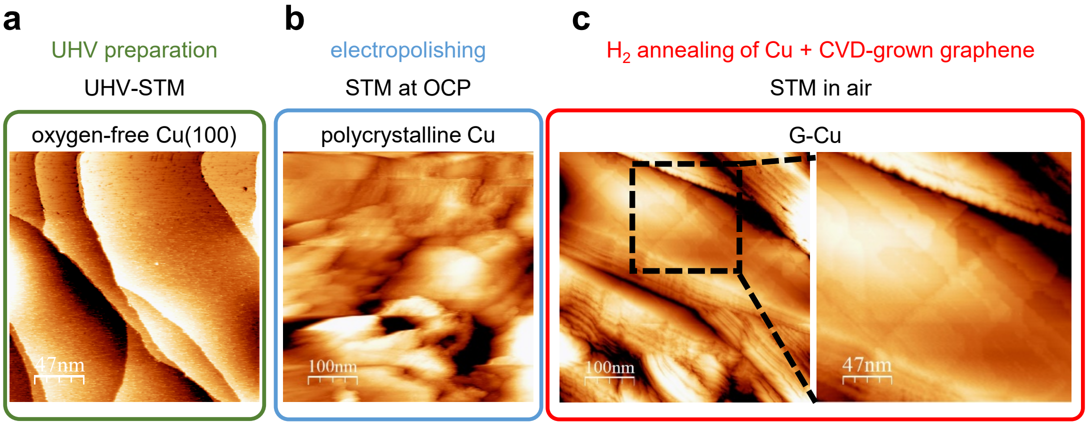
a
UHV preparation
UHV-STM
oxygen-free Cu(100)
47nm
b
electropolishing
STM at OCP
polycrystalline Cu
100nm
c
H_2 annealing of Cu + CVD-grown graphene
STM in air
G-Cu
100nm
47nm

Figure 2.14 – **Scanning tunneling microscopy: Cu surfaces.** STM characterization of Cu surfaces prepared by different pre-treatments and acquired under different conditions. (a) UHV-STM image of Cu(100) single crystal cleaned by sputtering-annealing cycles. Courtesy of Daniel Salinas Hurtado and adapted from reference 77. (b) STM image of electropolished polycrystalline Cu obtained under open circuit conditions. (c) STM images of G-Cu obtained in air.

Part II

Surface evolution

3 Emergence of Cu nanocuboids during CO_2RR

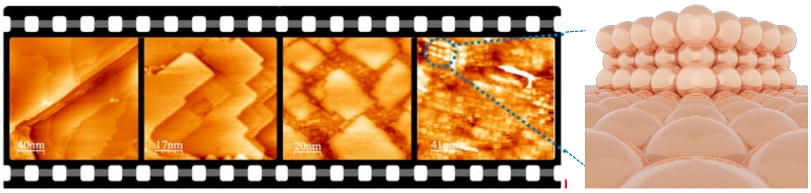

The electroreduction of CO_2 is a promising strategy towards sustainable fuels. Cu is the only Earth-abundant and pure metal capable of catalyzing CO_2-to-hydrocarbons conversion with significant faradaic efficiency; yet, its dynamic structure under *in situ* CO2RR conditions remains unknown. In this Chapter, we employ electrochemical scanning tunneling microscopy and Raman spectroscopy to study the evolution of Cu-based CO_2RR catalysts *in situ*. EC-STM studies reveal the structural evolution of polycrystalline Cu surfaces and the formation of Cu nanocuboids. If the Cu surface is covered by a graphene monolayer, smaller cuboids can be prepared. The graphene-protecting layer softens the 3D morphological changes that Cu-based catalysts suffer when exposed to aggressive electrochemical environments and allows us to track the kinetic roughening process. Nanocuboids can be found over a wide range of potentials, polarization times, and electrolyte compositions. Our results indicate that nanocuboid formation is a universal phenomenon for Cu-based CO_2RR catalysts. A synergy of EC-STM and *in situ* Raman spectroscopy supported by DFT calculations reveals that Cu nanocuboids form upon potential-driven re-organization of metallic Cu atoms.

This Chapter presents the results published in the form of a Communication in reference 28: Thanh Hai Phan[†], **Karla Banjac**[†], Fernando P. Cometto, Federico Dattila, Rodrigo García-Muelas, Stefan J. Raaijman, Chunmiao Ye, Marc T. M. Koper, Núria López, and Magalí Lingenfelder*, “Emergence of Potential-Controlled Cu-Nanocuboids and Graphene-Covered Cu-Nanocuboids under Operando CO_2 Electroreduction”, *Nano Letters* 21, 2059–2065 (2021), [†] equal contribution. Supplementary data to this Chapter is presented in Appendix

B. I complement the results reported in reference 28 with unpublished studies of the electrolyte effect on the *in situ* structural evolution (Section 3.3).

I acknowledge Dr. Federico Dattila, Dr. Rodrigo García-Muelas, and Professor Núria López (Institute of Chemical Research of Catalonia, Spain) for the theoretical model, Stefan J. Raaijman, Chunmiao Ye, and Professor Marc T. M. Koper (University of Leiden, The Netherlands) for extensive help with the product characterization experiments during research visit to their laboratory.

3.1 Introduction

The electrochemical reduction of CO_2 into hydrocarbons is a highly promising solution for the production of renewable fuels. One of the drawbacks of this technology is that most catalysts are not selective towards energy-rich C_{2+} fuels, and therefore, their efficiency is limited. Cu is the only earth-abundant, pure metal CO_2RR catalyst capable of converting CO_2 into hydrocarbons.[78] Initial optimization towards enhanced ethylene production relies on a morphology-selectivity relationship highlighting (100) facets as ideal geometry for C-C coupling.[33,79] This reflects in an outstanding interest in the synthesis of (100)-rich catalysts (*i.e.*, Cu nanocubes) through colloidal chemistry,[35] electrodeposition,[80] electrochemical cycling,[81] and reduction of thermally[82] or electrochemically grown[83] Cu oxides. The first three synthesis approaches rely on additive-assisted nanocube stabilization: colloidal chemistry employs organic surfactants,[35,84] whereas electrochemical NCs synthesis exploits chloride-containing electrolytes.[36,81,85]

However, this morphology-selectivity trend based on *ex situ*, post mortem studies ignores the morphological evolution of the catalysts during CO_2RR. As discussed in Section 1.3, Cu-based catalysts are highly dynamic. Nanoparticle catalysts undergo fragmentation[86] and coarsening,[46] while surface reconstructions[47] at the atomic scale occur on all Cu catalysts. These morphological changes greatly affect the catalysts' long-term stability (in terms of their catalytic activity and product selectivity).

The goal of *in situ* studies investigating surface dynamics is thus three-fold:

- to gain insight into *in situ structural transformation*
- to study the changes in the *oxidation states*
- to correlate such transformations with the trends reported in product evolution over time

3.2 Experimental details

EC-STM. EC-STM measurements were performed using the set-up reported in Section 2.1.1. G-Cu was used as the working electrode, two Pt wires were used as a pseudo-reference and counter electrodes. A new EC-STM tip and a new G-Cu sample were used for each measurement. The structural evolution of Cu surface underneath graphene was followed upon constant-potential polarization at the potentials beyond Cu_xO reduction peak under the conditions reported in Table 3.1.

AFM. *Ex situ* AFM characterization was performed on bare Cu foils and G-Cu after potentiostatic polarization in 0.1 M CO_2 saturated $KHCO_3$ at $-0.03\,V$ *vs* RHE for 8 hours. As-prepared samples were washed by water and dried with N_2 flow. FastScan-B (Bruker) probes were used.

Raman spectroscopy. *Ex situ* and *in situ* Raman spectroscopy experiments were performed using the set-up reported in Section 2.2.1, 488 nm laser, and a grating of 2400 lines/mm. *Ex situ* Raman spectra were collected using 100× objective (Leica). Raman spectra were

Table 3.1 – **Experimental conditions for EC-STM studies.**

electrolyte	gas	pH_{bulk}	potential *vs* Pt pseudo-RE
0.1 M H_3PO_4+0.1 M KH_2PO_4	N_2	2.2	-0.5 V
0.1 M $NaHCO_3$	CO_2	6.8	−1 V
0.1 M $KHCO_3$	CO_2	6.8	−1 V, −1.6 V, and −1.8 V
0.1 M $CsHCO_3$	CO_2	6.8	−1 V
0.1 M K_2CO_3	N_2	8.5	−1 V and −1.1 V
0.1 M KOH	N_2	13	−1 V

firstly collected on the pristine G-Cu. The same sample was then used for preparation of the nanocuboids (protocol: potentiostatic polarization in 0.1 M CO_2 saturated $KHCO_3$ at −0.03 V *vs* RHE for 4 hours). As-treated sample was rinsed with toluene and Milli-Q water, dried with N_2, and then, characterized by Raman spectroscopy. Accumulation time was 6 (10) seconds for the G-Cu (G-Cu after nanocuboid formation) spectra. *In situ* Raman spectra were collected on G-Cu during nanocuboid formation (same electrochemical protocol as for *ex situ* Raman studies). Figure 3.5 a) shows the representative Raman spectra of the Raman map collected over $5 \times 5\,\mu m^2$ surface area. Figure B.7 shows the average Raman spectra of the Raman map collected in a Stream Line Mode over $25 \times 100\,\mu m^2$ surface area.

Product analysis. Product analysis was performed in a custom-made, two-compartment electrochemical cell, where the gas compartment of the working electrode compartment was connected via an automatic sampling loop to the gas chromatograph (Section 2.3.2). G-Cu was used as the working electrode; leakless Ag/AgCl reference electrode immersed in 3.4 M KCl (model ET072, eDAQ) was used as the reference electrode; a coiled Au wire was used as the counter electrode. A new sample was used for each measurement. Products dissolved in the electrolyte were analyzed from the aliquots taken from the catholyte once the chronoamperometry finished. The electrolysis was carried out upon constant-potential polarization for ≈ 1 hour, during which three gas aliquots were injected into gas chromatography at ≈ 10 minute, ≈ 30 minute, and ≈ 60 minute using an automatic sampling loop. For the measurement at −1.1 V *vs* RHE, the electrolysis was carried out for 20 minutes. The steady state currents, used for the calculations of the faradaic efficiencies, were calculated based on the average current between the 5th and 60th minute. Average values of faradaic efficiencies and their standard deviations reported for each data point in Figure 3.2 b) were calculated based on gas samples injected at ≈ 10 minute, ≈ 30 minute, and ≈ 60 minute. Figure 3.2 b) reports only the major products.

3.3 Results

Structural evolution: emergence of Cu nanocuboids

Figure 3.1 shows the dramatic structural transformation that polycrystalline Cu surfaces undergo during potentiostatic polarization in a halide-free electrolyte at CO_2RR potentials over, at least, 4 hours. The Cu surface is covered by cuboidal features that are up to 400 nm in width. Surprisingly, nanocuboids were also found underneath graphene, in G-Cu samples

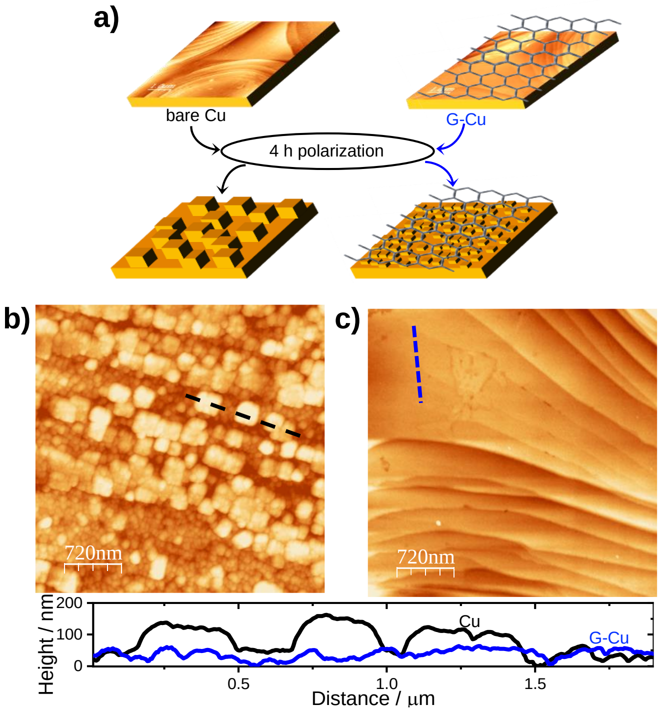

Figure 3.1 – **Structural evolution of Cu surfaces under CO_2RR conditions: nanocuboid formation.** (a) Scheme of the nanocuboids formed on bare, polycrystalline Cu and G-Cu after CO_2RR in 0.1 M CO_2 saturated $KHCO_3$ at $-0.03\,V$ *vs* RHE for, at least, 4 hours. AFM images of the nanocuboids on (b) bare, polycrystalline Cu and (c) G-Cu formed under CO_2RR conditions in a) together with the corresponding height profiles.

after the same electrochemical treatment (Figure 3.1 c)). These findings suggest *in situ* formation of the nanocuboids under CO_2RR conditions, in agreement with the literature on the surface reconstruction of the polycrystalline Cu surfaces to Cu(100).[47,87,88] The nanocuboids on polycrystalline Cu are about 100 times larger than the ones underneath graphene on G-Cu. This size difference implies that graphene act as a 2D protecting layer, softening the 3D morphological changes. Moreover, the fact that the nanocuboids form both on bare, polycrystalline Cu and on G-Cu suggests similar surface processes behind this transformation. We thus use the G-Cu model system to track the morphological evolution *in situ* by EC-STM and Raman spectroscopy.

G-Cu as CO_2RR catalyst

Bare Cu surfaces and Cu surfaces underneath graphene not only undergo similar structural transformation under CO_2RR conditions, but also perform similarly as CO_2RR catalysts. CO_2RR catalytic performance of G-Cu was benchmarked against bare polycrystalline Cu surface reported by Kuhl *et al.*[89] Potential-dependent product analysis was performed upon constant-potential CO_2RR using gas chromatography and high performance liquid chromatography (Figure 3.2). G-Cu and Cu show significant resemblance both in the catalytic activities and CO_2RR product selectivity. Note that the catalytic activity graph in Figure 3.2 a) shows current densities corrected for geometrical areas rather

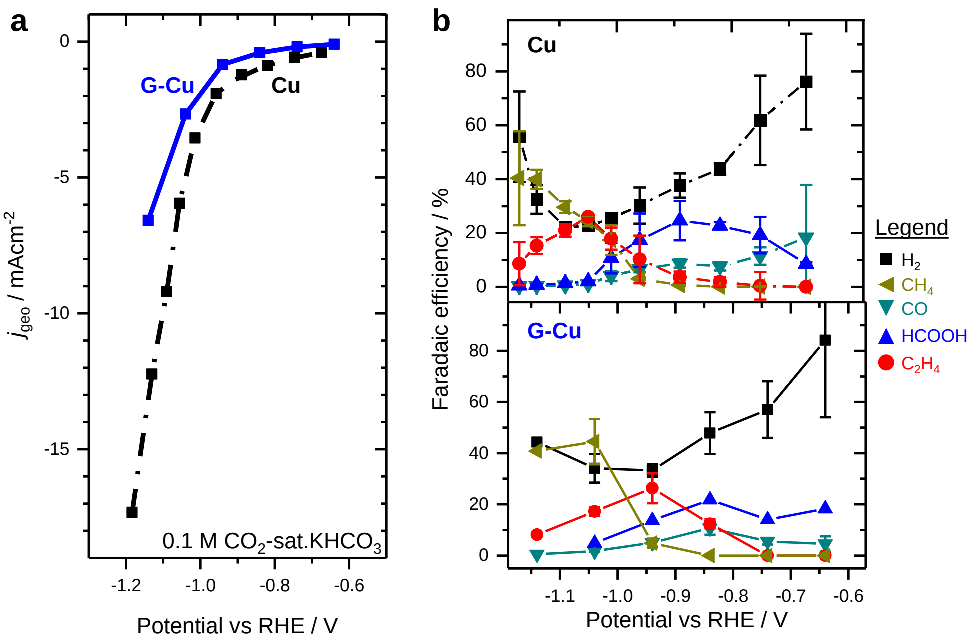

Figure 3.2 – **G-Cu model system: CO$_2$RR catalytic performance.** (a) CO$_2$RR catalytic performance of G-Cu and electropolished polycrystalline Cu foil. (b) Potential-dependent product selectivity. Data points for Cu activity and product selectivity re-plotted from references 30 and 89, respectively.

than for electrochemically active surface area. Following the fact that hydrogen-annealed polycrystalline Cu surface underneath graphene is smoother than electrochemically-polished Cu (*i.e.*, G-Cu has lower ECSA than Cu), we expect similar ECSA-corrected current densities for G-Cu and Cu. It is worth nothing here that this comparison between CO$_2$RR catalytic activity of G-Cu *vs* bare Cu relies on the comparison of the product analysis experiments on Cu and the literature report[89] for Cu. Moreover, we found remarkably similar trends in product selectivity on G-Cu and electrochemically-polished Cu (Figure 3.2 b)), suggesting similar CO$_2$RR pathways on both Cu surfaces regardless if covered by graphene or being bare.

In situ characterization of G-Cu under the conditions of CO$_2$RR performance tests in Figure3.2 reveals that graphene overlayer breaks at -0.6 V *vs* RHE, *i.e.*, at the onset potential for H$_2$ and CO gas bubble evolution (Figure A.1). Gas bubble evolution causes graphene rupture, probably at the positions of the graphene defect that show high catalytic activity due to the local intercalation of electrolyte species (*e.g.*, H$_2$ and CO). Once broken, graphene remains intact over >50% of the surface and it does not detach from Cu surface, even after prolonged CO$_2$RR under harsh bubble evolution at -1 V *vs* RHE (Appendix A).

In situ EC-STM insights

Dynamics of the nanocuboid formation was followed on G-Cu by *in situ* EC-STM. STM offers the unique possibility to monitor preferentially either the graphene layer or the Cu underneath by changing the STM bias conditions (Figure 3.3 a)). The polarization potential, located at a more negative value than the Cu$_x$O reduction potentials, was kept

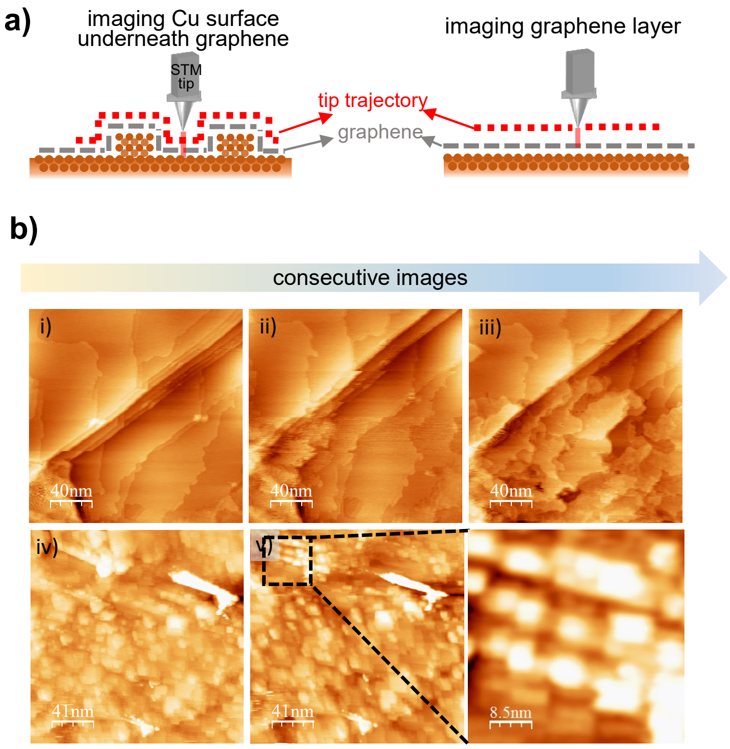

Figure 3.3 – ***In situ* structural evolution of Cu surface during CO_2RR.** (a) Schemes illustrating STM imaging of G-Cu: by changing the STM scanning parameters, we visualize either the Cu surface underneath graphene or the atomic lattice of the graphene overlayer. (b) Series of EC-STM images showing the structural evolution of a polycrystalline Cu surface in 0.1 M CO_2 saturated $KHCO_3$ at $-1\,V$ *vs* Pt pseudo-RE.

constant at the positive edge of CO_2RR and the HER regime to avoid bubble evolution and interference of the faradaic currents with the tunneling current.

We first report the dynamics of the nanocuboid formation in an electrolyte widely used for CO_2RR: 0.1 M CO_2 saturated $KHCO_3$. Dynamic EC-STM studies reveal the different stages of the surface nanostructuration, where the small-cuboid features gradually grow on top of the Cu(100) crystalline facets. Interestingly, the nanocuboids are (100) facet multilayers, *i.e.* mounds (Figure B.1). Their size and the kinetics of formation can be tuned by changing the potentiostatic polarization time or the polarization potential: the nanocuboid size decreases for long potentiostatic polarization and/or more negative potential (Figures B.2 and B.3).

Electrolyte effect

Next, we performed a series of EC-STM experiments in a set of electrolytes covering a wide pH range and containing different cations and anions. We first focus on K^+-containing electrolytes:

- N_2 saturated 0.1 M H_3PO_4+0.1 M KH_2PO_4 (pH_{bulk}=2.2),
- 0.1 M CO_2 saturated $KHCO_3$ (pH_{bulk}=6.8),

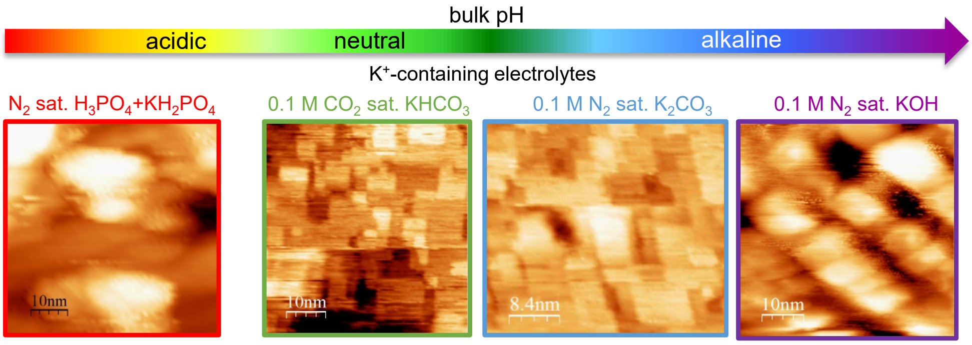

Figure 3.4 – ***In situ* structural evolution at CO_2RR/HER potentials: Effect of pH.** EC-STM images showing nanocuboids formed on G-Cu.

- 0.1 M N_2 saturated K_2CO_3 ($pH_{bulk}=8.5$),
- 0.1 M N_2 saturated KOH ($pH_{bulk}=13$),

which allow us to study the effects of dissolved CO_2, electrolyte pH, and anions. All electrolytes were free of halide anions.

EC-STM images confirm that the nanocuboids form on Cu surfaces under CO_2RR/HER conditions over a wide range of pH and electrolyte compositions. Control experiments in Na^+- and Cs^+-containing electrolytes (0.1 M CO_2 saturated $MHCO_3$, M=Na and Cs) further confirm that multilayer mound formation can eventually be found in all the studied electrolytes (Figure B.4). Interestingly, the nature of the cation seems to affect the kinetics of the nanocuboid evolution. As we will discuss in Chapter 6. The fact that similar structures can be identified over a wide range of electrolyte conditions, points towards a potential driven mechanism, rather than an additive induced reconstruction.

Density functional theory modeling further supports a potential-driven nanostructuring process (Figures B.5 and B.6). The model confirms that Cu(100) facets are stable at negative potentials. Moreover, smaller nanocuboids have a shorter principal radius of curvature and thus, experience a high electric potential across them. This reflects in further reduction of nanocuboids' size over time.

Spectroscopic insights

To study the chemical composition evolution associated with the nanocuboid formation, we used *in situ* Raman spectroscopy. Raman spectra show the absence of Cu oxides during the nanocuboids formation in 0.1 M CO_2 saturated $KHCO_3$ (Figure 3.5 a)). The first spectrum obtained under open circuit conditions exhibit the peaks at $213\,cm^{-1}$, $413\,cm^{-1}$, and $640\,cm^{-1}$ in low spectral regions.[59] These peaks are assigned to native Cu_xO formed upon ambient and/or wet oxidation under open circuit potential. We then started the polarization at $-0.03\,V$ *vs* RHE for 4 hours during which the nanocuboids form. The Raman peaks of Cu_xO are not visible in the spectrum obtained within the first minute of polarization. The disappearance of the Cu_xO peaks suggests reduction to metallic Cu. The prompt reduction of Cu_xO was also confirmed over $25 \times 100\ \mu m^2$ surface areas(Figure 3.5 a)). Moreover, Raman spectra obtained over 4 hours show that Cu remains in the

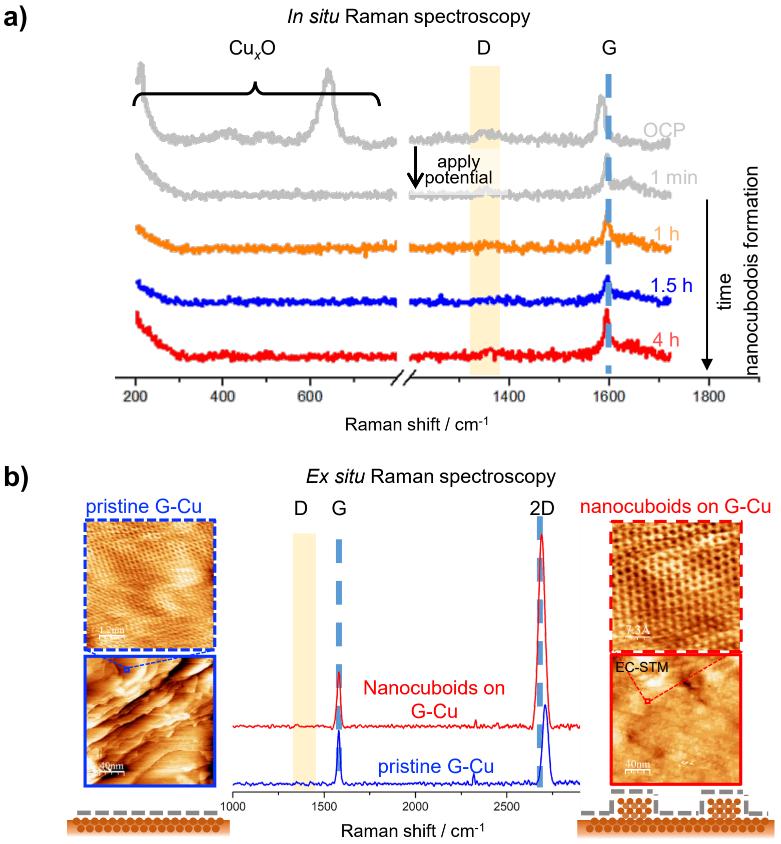

Figure 3.5 – **Raman spectroscopy: nanocuboid formation.** (a) Representative Raman spectrum obtained on air-oxidized G-Cu under open circuit potential and *in situ* Raman spectra obtained during nanocuboid formation in 0.1 M CO_2 saturated $KHCO_3$ at -0.03 V *vs* RHE. The prompt reduction of the native Cu_xO suggests the sole presence of the metallic Cu during nanocuboid formation. (b) *Ex situ* Raman spectra of G-Cu before and after nanocuboid formation together with STM images showing atomic lattices of graphene. Both in a) and b), the graphene's G band and the absence of the defect-induced D band, in the wavenumber region denoted with yellow rectangles, confirm that graphene remains globally intact over the nanocuboids during and after their formation.

metallic state (*i.e.*, oxidation state Cu^0).

Additionally, *in situ* and *ex situ* Raman spectra reveal that graphene remains intact during nanocuboid formation. All spectra exhibit typical graphene peaks at $\approx 1585\,\mathrm{cm}^{-1}$ (the G band) and at $\approx 2696\,\mathrm{cm}^{-1}$ (the 2D band). The absence of the defect-induced D band ($\approx 1350\,\mathrm{cm}^{-1}$) confirms the presence of a defect-free graphene layer before (*i.e.*, on pristine G-Cu), during, and after nanocuboid formation (Figure 3.5 b)).

3.4 Discussion

The results presented above reveal significant evolution of Cu-based catalysts during CO_2RR. EC-STM studies show that multilayer mounds (*i.e.*, nanocuboids) form on Cu surfaces under CO_2RR conditions. *In situ* Raman spectroscopy confirmed the prompt reduction of the (native) Cu_xO layer at $-0.03\,V$ *vs* RHE.

To the best of my knowledge, this study is the first report on the emergence of the nanocuboids under CO_2RR conditions. The nanocuboids form upon *in situ* structural evolution, similarly to *in situ* surface reconstruction of polycrystalline Cu surface to Cu(100).[47] Therefore, nanocuboid formation under CO_2RR conditions defers from the earlier-reported literature on the synthesis of Cu nanocubes.[35–37,80,81,85]

When comparing nanocuboids formed on G-Cu and on bare Cu, the main difference is the nanocuboid size with the general trend being larger nanocuboids on bare Cu than on G-Cu. Unambiguous conclusion on the role of graphene is thus not straightforward because graphene simultaneously acts as a diffusion[90] and short-term anticorrosion[73,91] barrier. Furthermore, recent literature reports similar *in situ* surface reconstructions[87,88]: the *in situ* SEM study discuss the formation of lumps, while the *in situ* GIXRD study reveals reconstructions to (100)-like facets. Our results indicate that both references probably report the same phenomenon, *i.e.*, nanocuboid formation.

In situ EC-STM and Raman studies revealed the dynamics of *in situ* transformations leading to nanocuboid formation. In particular, the nanocuboids are metallic Cu(100) mounds. A detailed analysis of the first steps in the formation of nanocuboids points towards a kinetic roughening process, where the mounds arise as a consequence of step-edge (Ehrlich-Schwoebel) barriers, inhibiting downward transport of adatoms. The fact that these are far-from-equilibrium structures is consistent with the sharp straight step edges along [010] and [001] Cu(001) directions, in contrast to the edge-rounded equilibrium structures seen after homoepitaxy of Cu on Cu(001).[92,93] Moreover, comparison of EC-STM images in Figure 3.3 with the earlier reported (EC-)STM studies on Cu in the presence of OH[94] and CO[95,96] adsorbates further supports that these surface adsorbates are not directly involved in the step shaping process.

Furthermore, nanocuboids form in over a wide range of electrolyte conditions (different pH, cations, and anions). This suggests that potential-driven nanostructuring is a general explanation for *in situ* evolution of Cu catalysts under CO_2RR conditions. Interestingly, even if nanocuboids are present in many different electrolytes, the electrolyte composition might affect kinetics of their formation and evolution over time. This is especially interesting for the studies of the cation effect on CO_2RR suggesting that large cations promote formation of C_{2+} products.[97,98] While in-depth understanding of the cation effect remains elusive, our preliminary studies support that the cations might affect the time needed to observe the nanocuboids, and therefore, might be an additional parameter indirectly affecting CO_2RR product selectivity trends.

In situ evolution to nanocuboids seems to be a different surface phenomenon than the surface reconstruction of polycrystalline Cu to Cu(100)-like surface, denoted as Cu(polycrystalline)→ Cu(111)→Cu(100).[47,99] This premise on the differences between nanocuboid formation and Cu(polycrystalline)→Cu(111)→Cu(100) reconstruction relies on the following experimental observations. First, our EC-STM studies suggests the growth of (100) facets on top of the (100) crystalline grain rather than transformation of polycrystalline Cu to (100) facets. Second and as we shall further discuss in Chapter 6, we have never observed the transformation to (111) facets as the intermediate stage. Third,

(100) facets in reference 47 are much larger than the nanocuboids.

The immediate reduction to metallic Cu was confirmed both over micrometer scale using *in situ* Raman spectroscopy and at the nanometer scale using EC-STM, in agreement with recent *in situ* GIXRD and quasi *in situ* XPS studies.[67,100] Furthermore, EC-STM studies allow us to discard the hypothesis on the stability of the surface oxygen traces: if the oxide species were stable, we would have observed characteristic Cu_xO structures.[101,102] As this was not the case, we conclude that the nanocuboids are composed of the metallic Cu atoms.

The results reported herein break down the misconceptions that the Cu catalysts surfaces are static. We further shed light on the fact that Cu catalysts when normalized by the electrochemically active surface area show similar intrinsic activity[30]; most likely, because the surface morphology (although highly dynamic) under *in situ* conditions are very similar at the atomic scale–the scale where ultimately CO_2RR occurs.

3.5 Conclusion

In conclusion, we show that Cu surfaces undergo a drastic structural transformation upon polarization at CO_2RR potentials. In particular, polycrystalline surfaces evolve to nanocuboids, even in halide-free electrolytes. The size of the nanocuboids can be tuned by the applied potential, polarization time, or pre-covering Cu surfaces by a single graphene layer, as in case of G-Cu. We further benchmarked G-Cu as a CO_2RR catalyst and employed it as model system for *in situ* EC-STM studies, that elucidate the dynamics of the nanocuboid formation in 0.1 M CO_2 saturated $KHCO_3$. Further EC-STM studies, revealing the nanocuboids at CO_2RR/HER potentials using different electrolytes, allowed us to exclude the sole effect of the adsorbates on the nanocuboid formation mechanism. A synergy of EC-STM and *in situ* Raman spectroscopy studies, supported by DFT calculations, show that the nanocuboids form upon potential-driven re-organization of metallic Cu atoms. This study opens new avenues to reinterpret the nanostructuration mechanism of Cu-based CO_2RR catalysts without involving oxidized Cu species or halides as adsorbates during a step pinning process.

Surface chemistry Part III

4 Oxidation of G-Cu

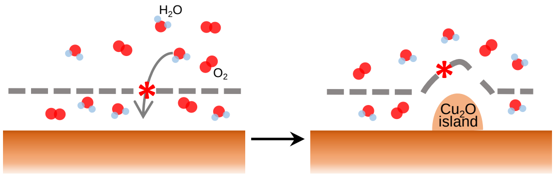

Chapter 3 benchmarks the graphene-covered Cu model system as a CO_2RR catalyst. In this Chapter, we study Cu oxidation to provide insights in the surface chemistry of the Cu surface underneath graphene. In contrast to CO_2RR, oxidation of bare Cu is a well-studied phenomenon explained down to atomistic details. For the first time, we address the oxidation mechanism of Cu underneath graphene through a combination of *ex situ* AFM, (quasi) *in situ* EC-STM, Raman spectroscopy, and XPS. We show that ambient oxidation proceeds through several steps: (i) intercalation of oxygen and water molecules through graphene defects; (ii) adsorption of as-intercalated species to the Cu surface and formation of Cu–$(2\sqrt{2}\times\sqrt{2})R45°$–O superstructures; (iii) local formation of Cu_2O islands underneath graphene defects; (iv) lateral growth of as-formed islands through (ii) and (iii) processes. Formation of nanometer-sized Cu_2O islands and spatial inhomogeneity in oxide formation over micrometer length scales is thus the main oxidation process for G-Cu. Moreover, a quasi *in situ* EC-STM study reveals rapid re-oxidation of Cu underneath graphene once the CO_2RR experiments stop. The resemblances in Cu surface oxidation processes between bare Cu and Cu underneath graphene highlight a unique surface chemistry of Cu surfaces. Knowledge on oxidation of Cu underneath graphene is of paramount importance for the interpretation of *in situ* surface studies in Chapters 5 and 6.

This Chapter discusses the unpublished work on the oxidation of G-Cu. The results are currently presented in the manuscript: Karla Banjac*, Thanh Hai Phan, Fernando P. Cometto, Patrick Alexa, Yunchang Liang, Rico Gutzler, and Magalí Lingenfelder, “Surface chemistry of copper micro- and nanocubic catalysts for electrochemical CO_2 reduction”.

4.1 Introduction

Cu oxidation was a central research topic for decades.[103,104] The development of scanning tunneling microscopy, that allows direct observations of oxidation process in a controlled ultra-high vacuum environment, revealed the oxidation mechanisms.[101,102,105,106] The surface oxidation of Cu(100) proceeds via four steps[101]: (i) dissociative adsorption of O_2; (ii) formation of Cu–$(2\sqrt{2} \times \sqrt{2})R45°$–O surface reconstruction at the coverage of 0.5 monolayer; (iii) formation of the Cu_2O islands; (iv) formation of the highly-corrugated CuO islands. The Cu–$(2\sqrt{2} \times \sqrt{2})R45°$–O reconstruction formed in step (ii) is one of the most studied reconstructions in surface science.[107,108] The pattern arising from this reconstruction is the characteristic signature of the oxygen adsorbates and thus, allows the STM community to readily distinguish the Cu surfaces with oxygen adsorbates *versus* oxygen-free surfaces.

While bare Cu surfaces are highly prone to ambient oxidation,[109] one expects that oxidation is suppressed if a protecting layer covers the Cu surface. An example of such an overlayer is graphene that acts as a gas-impermeable membrane.[110] The ability of graphene to protect Cu against ambient oxidation has been demonstrated for polycrystalline Cu up to 4 hours and for Cu(111) single crystal up to 20 days.[66,73] However, numerous studies testing the protective role of graphene contradict these findings, even showing that the oxidation kinetics seems to be faster in the presence of graphene than it is on a bare Cu foil.[111] These two contradictory findings rise questions on the mechanism of Cu oxidation under graphene.

This Chapter presents fundamental studies of ambient and wet Cu oxidation. Oxidation under these conditions might affect the interpretation of *ex situ* studies of the same model system under CO_2RR conditions. Therefore, we aim to:

- benchmark the oxidation behavior of the G-Cu model system,
- understand the differences in ambient and wet oxidation,
- gain understanding on atomistic details on oxidation, which allow us to close the knowledge gap on the surface physics processes between the ultra-high vacuum and high-pressure studies on oxidation of Cu single crystals, and ambient and wet Cu oxidation under realistic conditions.

By doing so, we gain the knowledge on the oxidation behavior of G-Cu. As the reader shall see, it is especially important to perform these studies on G-Cu samples used in Chapters 3, 5, and 6 because oxidation of Cu underneath graphene depends on the Cu substrate crystallinity, graphene quality, and preparation procedure.

4.2 Experimental section

Scanning probe microscopy. Hydrogen-annealed polycrystalline Cu foils and G-Cu were purchased from Graphenea. The samples were transferred in air-evacuated bags and characterized at the air/solid interface by AFM.

STM images of air-oxidized samples were obtained on: (i) G-Cu sample that was treated by electrochemical cycling between $-1.1\,\mathrm{V}$ and $+0.5\,\mathrm{V}$ *vs* RHE in 0.1 M CO_2 saturated $KHCO_3$ for 2 cycles and then, stored in air for 10 days (Figure 4.3 a)) and (ii) G-Cu that was stored in the glove box for more than 2 weeks (Figure 4.3 b) and c)).
Quasi *in situ* STM images of G-Cu in Figure 4.4 were obtained on G-Cu under open circuit potential conditions using EC-STM set-up. The images were obtained in 0.1 M CO_2 saturated $KHCO_3$ after stopping the CO_2RR experiment at $-1\,\mathrm{V}$ *vs* Pt pseudo-RE.

XPS. XPS spectra were obtained on hydrogen-annealed polycrystalline Cu foils and G-Cu purchased from Graphenea in air-evacuated bags. The samples were mounted on the sample holder in air and characterized without any pre-cleaning. The XPS characterization was conducted on a commercial Kratos AXIS Ultra system with a monochromatic Al Kα source ($h\nu$ =1487 eV).

XPS analysis. All spectra were referenced against the Cu^0 in Cu2p spectra at 932.6 eV.[70] The peaks were fitted using Voight functions after Shirley type background subtraction.

Raman spectroscopy. Details on *in situ* Raman spectroscopy set-up, workflow, and spectra analysis can be found in Chapter 2. Quasi *in situ* Raman spectra were obtained on G-Cu using the water immersion objective (Leica) in line illumination mode (laser focused in $\approx 12\,\mu\mathrm{m}$-long line) over $74\,\mu\mathrm{m}^2$ surface area. Exposure time was 35 seconds per four spectra. Spectra were collected over the same surface area, while the sample was in contact with 0.1 M CO_2 saturated $KHCO_3$ under open circuit potentials. For the studies of the wet oxidation over time, Raman spectra were collected on air-oxidized G-Cu. For the studies on the electrochemical oxidation, Raman spectra were collected on G-Cu sample on which the native Cu_xO was reduced at negative potentials.

4.3 Results

4.3.1 Ambient oxidation

The first evidences that graphene protects the underlying Cu from oxidation are visible from AFM images obtained at the air/solid interface (Figure 4.1). We compare the surface morphologies of bare polycrystalline Cu foil and graphene-covered polycrystalline Cu foil. For both samples, polycrystalline Cu foils were cleaned by annealing in hydrogen atmosphere, the samples were transferred in air-evacuated bags, and characterized by AFM several days after annealing. AFM images of Cu foil show Cu_xO layer, *i.e.*, Cu_xO nanoparticle-like islands, with diameters $\approx 20 - 40$ nm and heights up to 12 nm, formed upon ambient oxidation. In contrast, AFM images of G-Cu show mostly oxide-free Cu surface and a few hundred-nanometer-wide Cu_xO islands underneath graphene wrinkles. Only two Cu_xO islands were found across a $2 \times 2\,\mu\mathrm{m}^2$ surface area (Figure 4.1 b)).

The oxidation degree of air-oxidized Cu was analyzed by XPS (Figure 4.2). Cu2p and CuLMM spectra of bare Cu reveal the presence of Cu^+ and Cu^{2+}. Cu2p spectrum displays the peaks of Cu^0/Cu^+ at 932 eV and the strong satellites of Cu^{2+} at ≈ 943 eV, while CuLMM spectrum exhibit a strong peak at ≈ 917 eV arising from Cu^+ and Cu^{2+} species

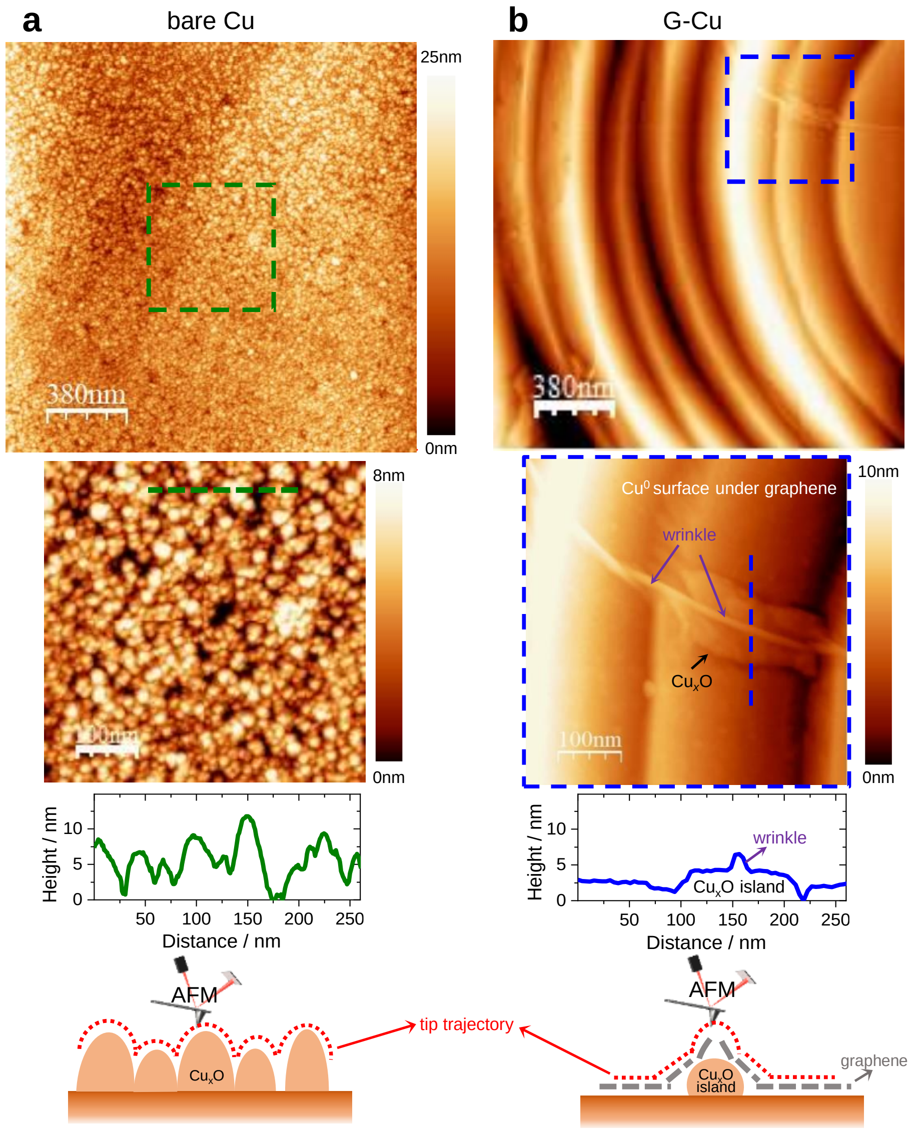

Figure 4.1 – **Ambient oxidation of bare Cu *vs* G-Cu: AFM.** (a) AFM images of air-oxidized polycrystalline Cu foil that was pre-cleaned by hydrogen annealing. (b) AFM images of G-Cu showing Cu step-edge bunches free of Cu_xO layer and a Cu_xO island formed underneath a graphene wrinkle.

at 916.5 eV and 917.8 eV, respectively.[70] These results suggest fast oxidation of bare Cu surfaces, in agreement with earlier reports.[109]

XPS of G-Cu confirms that the fresh G-Cu is mostly free of the oxides (Figure 4.2 b)). Cu2p spectrum of G-Cu shows strong peak of Cu^0/Cu^+ at 932 eV together with the weak satellite of Cu^+, whereas CuLMM spectrum displays an intense peak of metallic Cu at 918.4 eV and the small peak of Cu^+ at 916.5 eV.[70] Neither Cu2p nor CuLMM spectra have any signatures of Cu^{2+} species. Moreover, C1s peak (Figure C.5) confirms high quality of graphene. The peak component of graphene's sp^2 carbon is shifted for -0.4 eV with respect to graphene grown and characterized in UHV.[65] This shift suggests that graphene is not in direct contact with underlying Cu, further implying intercalation of ambient water

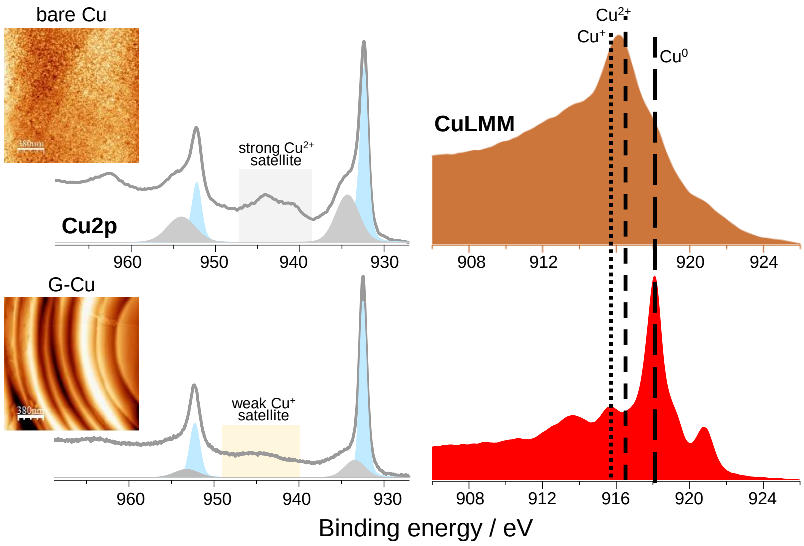

Figure 4.2 – **Ambient oxidation of bare Cu *vs* G-Cu: XPS.** XPS Cu2p and CuLMM peaks of air-oxidized polycrystalline Cu foil and G-Cu.

and oxygen through graphene defects.[112,113]

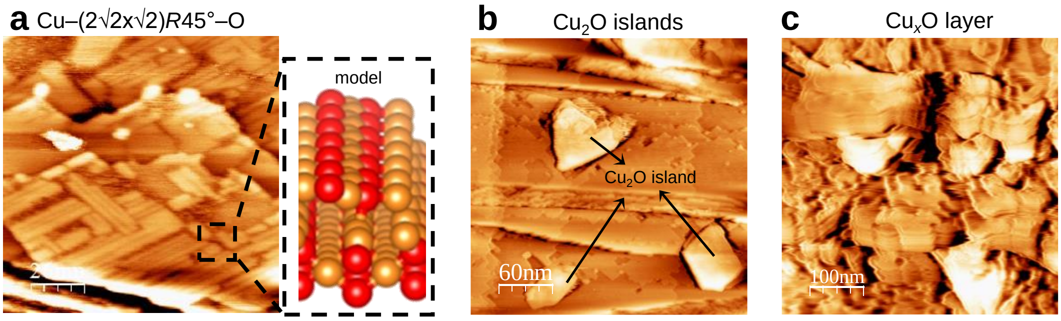

Figure 4.3 – **Cu oxidation under graphene.** Representative STM images showing three different degrees of Cu oxidation on G-Cu. (a) Cu–$(2\sqrt{2} \times \sqrt{2})R45°$–O reconstruction characteristic for initial stages of Cu oxidation. (b) Cu_2O islands grown on a metallic Cu surface. (c) Rough Cu_xO layer. STM images in b) and c) were obtained on the same G-Cu sample. Model in b) adapted from 114.

STM characterization of air-oxidized Cu under graphene shows the great similarities in the oxidation pathway for bare Cu and Cu under graphene. In particular, we found the surface motifs characteristic for each oxidation stage: Cu–$(2\sqrt{2} \times \sqrt{2})R45°$–O reconstruction, Cu_2O islands grown on Cu surfaces, and rough Cu_xO layers. These motifs often co-exist along the G-Cu sample (Figures 4.3 b) and c)). This goes in line with AFM images showing that Cu_xO islands form on the patches of Cu surface that are either uncovered or underneath graphene's defects.

4.3.2 Oxidation in contact with electrolyte

Oxidation at open circuit potential

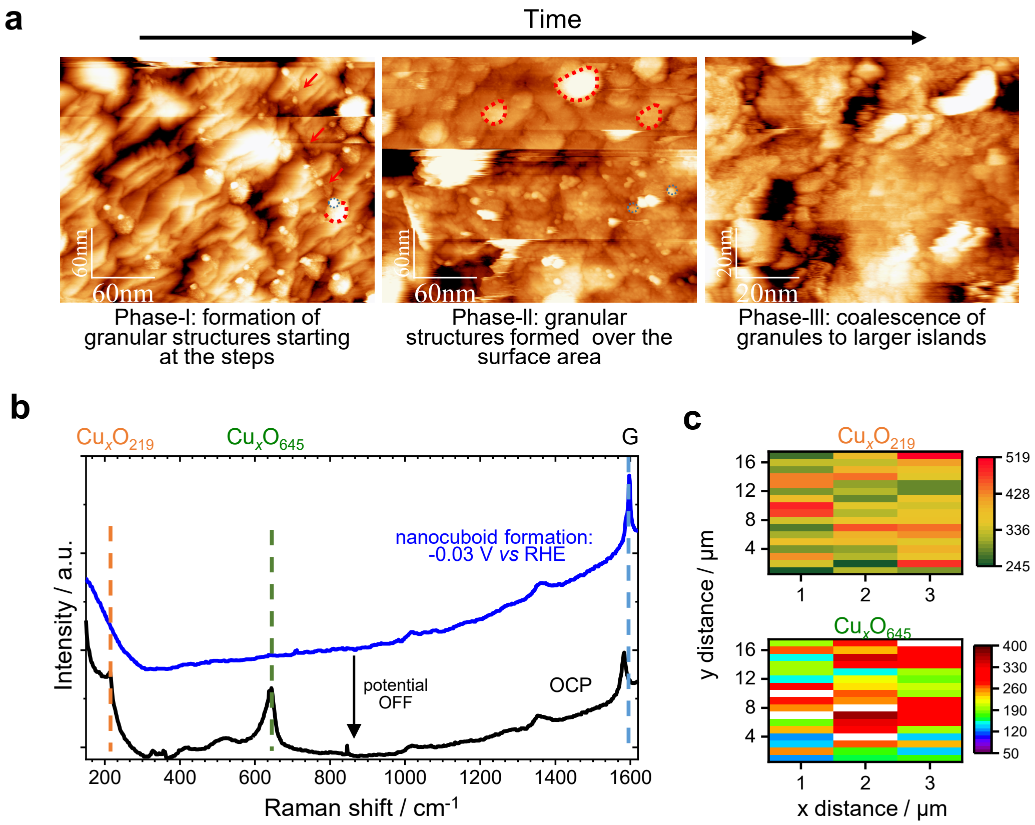

Phase-I: formation of granular structures starting at the steps

Phase-II: granular structures formed over the surface area

Phase-III: coalescence of granules to larger islands

Figure 4.4 – **Wet oxidation of Cu underneath graphene in contact with an electrolyte.** (a) Series of STM images showing Cu oxidation underneath graphene layer at open circuit potential after stopping polarization at -1 V *vs* Pt pseudo-RE. The red circles denote the areas where the graphene layer is decoupled due to the electrolyte intercalation; the red arrows denote graphene wrinkles spreading perpendicular to the step edges. The noisy appearance of the features denoted with red circles are related to the oxidation of the underlying Cu surface. (b) *In situ* Raman spectra showing fast Cu oxidation under open circuit conditions after stopping polarization at -0.03 V *vs* RHE. Raman spectra calculated as an average of Raman collected over $3{\times}17$ µm^2 surface area (c) Raman maps of the Cu_xO peaks at 219 cm^{-1} and 645 cm^{-1} shown in b). Electrolyte for both a) and b): 0.1 M CO_2 saturated $KHCO_3$.

Figure 4.4 a) shows STM images of G-Cu in contact with 0.1 M CO_2 saturated $KHCO_3$ over several minutes. The images were obtained at open circuit potential on the sample that was initially polarized at CO_2RR potential; they show the morphological evolution related to wet $Cu^0 \rightarrow Cu_xO$ oxidation.

Bright, round features first appear along the steps (Figure 4.4, left image). Their distribution along the surface is non-uniform, implying inhomogeneous wet oxidation. As-formed Cu_xO islands are embedded in ill-defined features of the near-round shape (denoted with the red circle in Figure 4.4). It is interesting to note that some of these features are interconnected by thin, neck-like connections that spread perpendicular to the step edges, similarly as for the graphene wrinkle in Figure 4.1 a). Similarities in the fine structure of the interconnections and the ill-defined features suggests that these features are similar, where the noise in these regions might be due to the dynamics of the oxidation process. Additionally, this noise might be due to poor conductivity of these regions, originating from a combination of the oxidation process and local graphene decoupling characteristic for the areas where an electrolyte intercalates.

We also observe heterogeneity in the surface appearance at $t_0 + 2\,\text{min}$. The surface area, that was metallic at t_0, is now covered with larger, noisy features, whereas the surface area with Cu_xO islands at t_0 is fully oxidized. As-formed Cu_xO islands have a diameter of (5.5 ± 0.4) nm and apparent height of (1.1 ± 0.3) nm. The whole surface is homogeneously covered with an ill-defined layer embedding a few bright, fuzzy blobs at $t_0 + 5\,\text{min}$. This layer has no resolvable inner structure. We were unable to follow the later stages of oxidation due to the STM instabilities, that arise due to the high roughness and poor conductivity of Cu_xO layers.

Fast oxidation under open cirucit potential conditions was further confirmed over micrometer scale by Raman spectroscopy. Similar as in EC-STM, Raman maps collected after stopping polarization at $-0.03\,\text{V}$ *vs* RHE show that Cu_xO layer forms within minutes (Figure 4.4 b)).

Wet oxidation beyond Cu_2O over long-term

The oxidation state of the native Cu_xO layer formed under open circuit conditions was studied by Raman spectroscopy. We aimed to answer the following questions: (i) Is the native Cu_xO layer formed under OCP conditions Cu_2O or CuO? and (ii) If it is Cu_2O, does it oxidize further to CuO when left under OCP conditions for few hours? Both questions are of great importance for the interpretation of the *ex situ* and quasi *in situ* studies in Chapter 5.

To mimic the realistic work flow of a typical CO_2RR experiment, where the samples often remain in the contact with an electrolyte for at least a few minutes until the electrochemical cell is disassembled, we follow the oxidation of G-Cu in contact with 0.1 M CO_2 saturated $KHCO_3$ over 2 hours. Figure 4.5 a) shows average Raman spectra of G-Cu calculated from 25 spectra collected over 5×5 μm^2. The first spectrum recorded at t_0 displays the peaks at $149\,\text{cm}^{-1}$ and $645\,\text{cm}^{-1}$. All three peaks characteristic for Cu_2O formed upon ambient or wet oxidation during the time the sample was in contact with an electrolyte, *i.e.*, between assembling the cell and setting-up the EC Raman experiment. No new peaks appear on Raman spectra recorded after 1 and 2 hours, suggesting on the sole existence of Cu_2O. While qualitative analysis of Cu_xO layer is limited by the overlap of Cu_2O and CuO peaks, both at $\approx 645\,\text{cm}^{-1}$, the insignificant variations of the position of the peak at $644\,\text{cm}^{-1}$ further confirm that this peak arises from Cu_2O. Additionally, insignificant variations of the Cu_2O peaks intensities imply the constant thickness of the Cu_2O layer.

Electrochemical oxidation of Cu surface underneath graphene

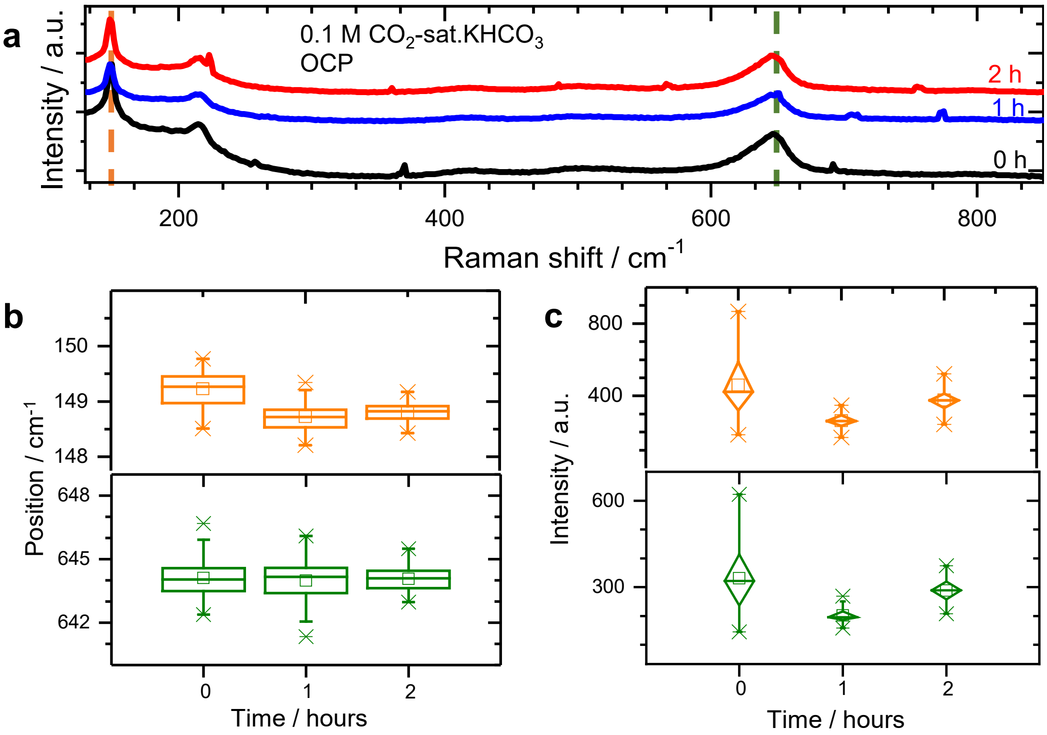

Figure 4.5 – **Wet oxidation of Cu underneath graphene in contact with an electrolyte over several hours: Raman spectroscopy.** (a) Average spectra showing wavenumber region of Cu_xO peaks. (b) Correlation between the position of the Cu_2O peaks centered at 149 cm^{-1} and 644 cm^{-1} and time. (c) Correlation between the intensity of the Cu_2O peaks centered at 149 cm^{-1} and 644 cm^{-1} and time. Electrolyte: 0.1 M CO_2 saturated $KHCO_3$.

We turn now to the electrochemical oxidation of Cu surface underneath graphene. *In situ* Raman spectroscopy allows us to simultaneously follow the Cu oxidation state and graphene integrity. We thus first perform LSV scan over Cu oxidation potentials. As soon as LSV ends, Raman spectra were then collected at open circuit potential.

Figure 4.6 a) shows electrochemical data of the above-described experiments. All three LSV curves are similar regardless of the upper potential limit. The anodic peak at +0.75 V *vs* RHE corresponds to $Cu \rightarrow Cu_2O/Cu(OH)_2/CuO$ oxidation. Corresponding Raman spectra are featureless in wavenumber region where one expects the Cu_xO peaks.[115] These results imply that graphene protects the underlying Cu surface against electrochemical oxidation. Simultaneously, the presence of the G band and the absence of the defect-induced D band in 1250–1650 cm^{-1} region confirm global integrity of graphene over the same surface area. Therefore: the anodic peaks are due to the oxidation of Cu areas that are exposed to the electrolyte, whereas the Cu surface underneath graphene remains metallic.

4.4 Discussion

The results presented in this Chapter provide us insights in the oxidation of Cu underneath graphene. Resemblances into the oxidation between high-pressure studies of bare Cu and

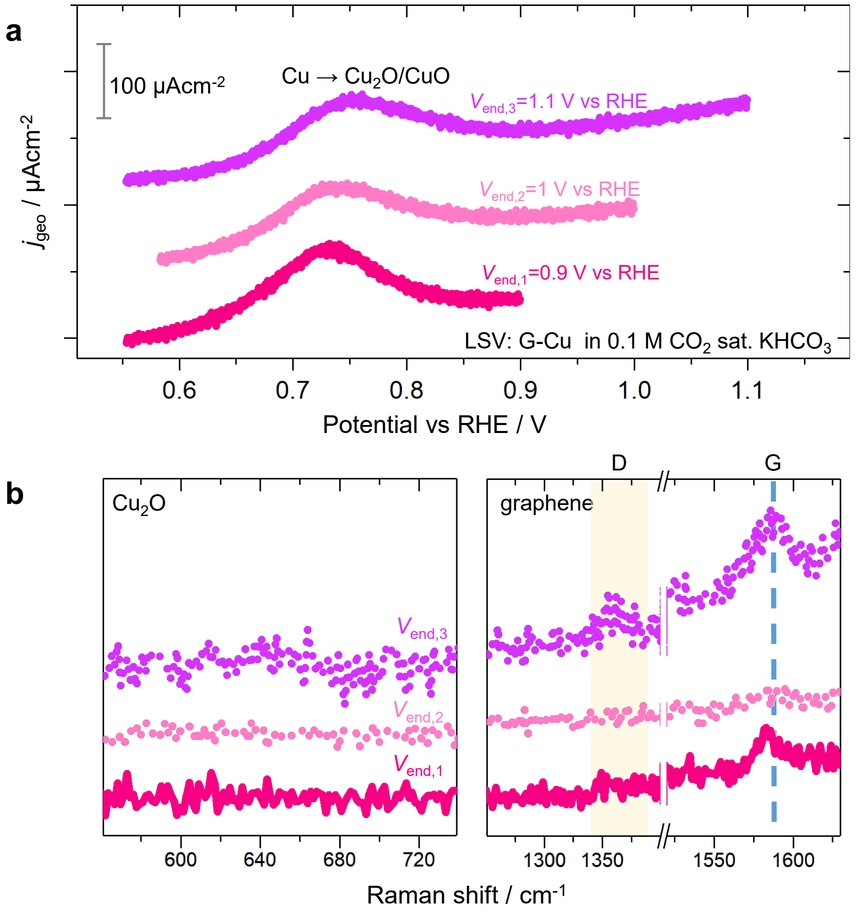

Figure 4.6 – **Quasi *in situ* Raman spectroscopy: electrochemical Cu oxidation underneath graphene.** (a) Linear sweep voltammograms of G-Cu in 0.1 M CO_2 saturated $KHCO_3$ with three upper potential limits of +0.9 V, +1 V, and +1.1 V *vs* RHE. Anodic peaks at +0.75 V *vs* RHE correspond to Cu→Cu_2O/CuO oxidation. (b) Raman spectra obtained after LSVs shown in a). The absence of the peaks in wavenumber region of Cu_xO implies that Cu surface remains metallic, whereas the G band together with the absence of the D bands suggest that graphene remains intact.

Cu underneath graphene serve as a surface science benchmark for the G-Cu model system. Furthermore, a combination of *ex situ* and *in situ* scanning probe microscopies, Raman spectroscopy, and XPS reveals the details on how the oxidation proceeds.

Bare Cu rapidly oxidizes under ambient conditions. XPS reveals that native oxide layer is composed of Cu_2O/CuO, where Cu_2O is the inner layer formed in the first stage of oxidation and CuO is the outer layer.[109] Such fast kinetics challenges direct studies of the first oxidation stages. On the contrary, graphene prevents direct adsorption of ambient oxygen and water on the Cu surface.[116] AFM and STM show that Cu underneath graphene oxidizes locally at the points close to the graphene defects and uncovered Cu areas. Examples are the graphene wrinkles that are not only rich in defects, but also act as water reservoirs.[117]

An idealistic, perfect graphene layer would prevent the direct adsorption of ambient oxygen

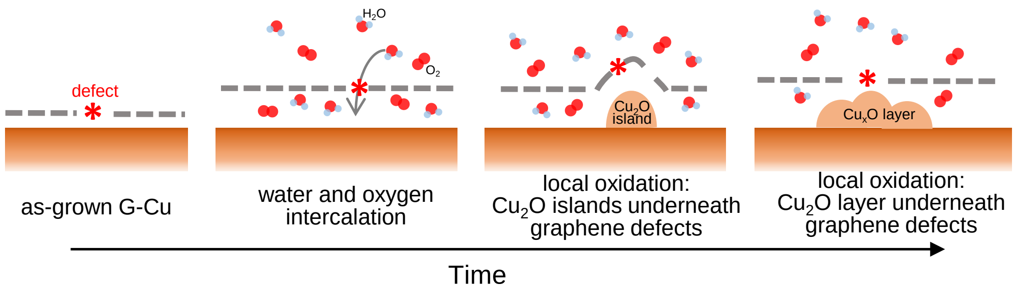
defect
H₂O
O₂
Cu₂O island
Cuₓ O layer
as-grown G-Cu
water and oxygen intercalation
local oxidation: Cu₂O islands underneath graphene defects
local oxidation: Cu₂O layer underneath graphene defects
Time

Figure 4.7 – **Local oxidation of Cu underneath graphene.** Scheme showing the oxidation of polycrystalline Cu surface under graphene. Initially, graphene is in close contact to metallic Cu. As soon as G-Cu is exposed to air, ambient oxygen and water vapor intercalate underneath graphene through defects and graphene decouples from Cu. Adsorption of oxygen and water species on Cu surface leads to local Cu oxidation. Further diffusion of the intercalated species across the interface between graphene and Cu results in lateral expansion of the oxidation front. The red asterisk denotes the graphene defect.

and water on the Cu surface.[116] However: in reality, graphene overlayers always have defects through which oxygen and water intercalate. Once intercalated, their adsorption on Cu surface underneath the defect triggers a local oxidation event. Further oxygen/water diffusion across the graphene/Cu interface governs the lateral expansion of the oxidation front leading to the final situation where Cu_2O can grow over the whole surface.

While the above-described processes vaguely illustrate the general oxidation process of Cu underneath graphene, STM reveals the similarities in the atomistic oxidation processes between ambient oxidation of polycrystalline Cu underneath graphene and Cu(100) single-crystal oxidation at high oxygen pressures.[101,102] In both cases, formation of well-ordered arrays of nanometer-sized Cu_2O islands is found to be the step preceding the growth of three-dimensional Cu_2O islands. By appreciating the similarities on the atomistic details of oxidation between Cu oxidation at high pressure and ambient Cu oxidation underneath graphene, we conclude that the main difference between oxidation of bare Cu and G-Cu is that Cu oxidation underneath graphene initiates through the local events related to the intercalation of ambient oxygen and water through graphene defects.

Intercalation/oxidation events also describe wet Cu oxidation. Direct studies confirming this hypothesis are experimentally challenging using STM and Raman spectroscopy because both techniques require to start with the samples in contact with an electrolyte/water. Wet oxidation, proceeding on G-Cu during the time that the electrochemical cell is assembled and the set-ups are optimized, results in formation of Cu_2O islands underneath graphene defects or thin Cu_2O layers. As-formed Cu_2O islands/layers get reduced once the potential is more negative than the potential of $Cu_xO \rightarrow Cu$ reaction, essentially during the first cathodic scan to CO_2RR potentials.[118]

Alternative studies on wet oxidation rely on observations after stopping *in situ* experiments at reductive potentials, while the Cu samples rest at open circuit potential. For G-Cu, STM reveals the formation of the Cu_xO islands within a few minutes. Their nucleation at the step edges and further growth over the surface terraces again resemble the formation of Cu_2O islands in high-pressure studies. As further discussed in Chapter 5, such a fast oxidation under open circuit conditions necessarily leads to detection of Cu_xO in *ex situ* and quasi *in situ* spectroscopic studies of Cu-based CO_2RR catalysts. Contrary to fast oxidation after stopping the polarization at negative potentials, quasi-*in situ* Raman studies on electrochemical Cu oxidation show that Cu underneath graphene remains metallic, even after sweeping the potential beyond Cu oxidation potential. This suggests that the water and oxygen de-intercalate during anodic scans. Potential-driven (de-)intercalation processes have been reported for Li-ion batteries and recently confirmed for G-Cu.[119,120]

Finally, Raman spectroscopy confirms that graphene remains intact during ambient and wet oxidation. In both cases, intercalation of the ambient and electrolyte species leads to decoupling, *i.e.*, formation of interfacial space.[65,121] This demonstrates that graphene is not a rigid overlayer, but rather flexible membrane readily responding to the environmental changes and external stimulants (such as potential).[120] Implications on the potential-driven intercalation opens an interesting possibility for investigating the effect of confinement on catalytic processes,[122–126] especially appealing to be investigated for CO_2RR where selective tunneling of protons through graphene[127] to the nanoconfined reaction reactor holds a promise to facilitate the formation of C_{2+} products.

4.5 Conclusion

This Chapter introduces graphene-covered polycrystalline Cu as a model system for surface science studies. A combination of scanning tunneling microscopy and Raman spectroscopies reveals that a high-quality graphene overlayer efficiently protects Cu from oxidation in the short-term. Oxidation starts at the local points underneath graphene defects through which oxygen and water species intercalate; further oxidation proceeds upon diffusion of as-intercalated species over the graphene/Cu interface and lateral expansion of the oxidation front. This knowledge on local oxidation of Cu underneath graphene on the fresh samples set the experimental baselines for utilization of G-Cu model system.

For both ambient and wet oxidation, STM studies reveal significant similarities in early oxidation stages between surface physics processes in ultra-high vacuum, gas, and aqueous environments. This information sets up the pathway toward closing the knowledge gaps currently standing between traditional surface science and *in situ* studies under electrochemical conditions.

5

In situ surface chemistry: Cu nanocuboids *versus* Cu_2O nanocubes

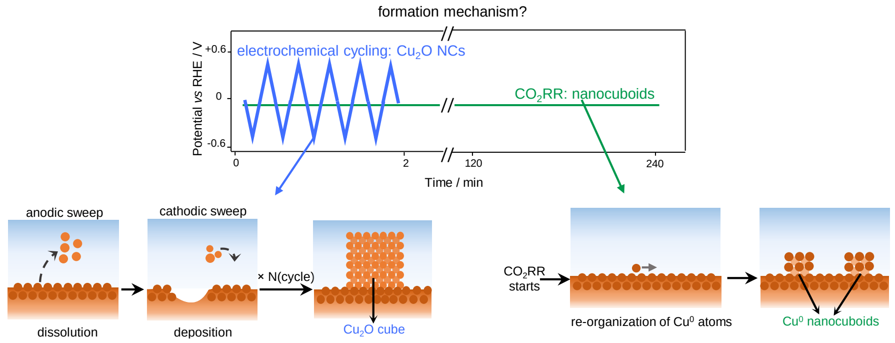
formation mechanism?
Potential vs RHE / V
+0.6
0
-0.6
electrochemical cycling: Cu_2O NCs
CO_2RR: nanocuboids
0
2
120
240
Time / min
anodic sweep
dissolution
cathodic sweep
deposition
× N(cycle)
Cu_2O cube
CO_2RR starts
re-organization of Cu^0 atoms
Cu^0 nanocuboids

Poor understanding of atomic processes at electrified interfaces hinders further advances in electrocatalysis. This is especially evident for Cu-based CO_2RR catalysts that are highly prone to *in situ* structural transformations. An example of such evolution, presented in Chapter 3, is the formation of nanocuboids. Here, the nanocuboid formation is compared with the growth of Cu nanocubes on Cu surfaces through electrochemical cycling in Cu-free solutions. A synergy of electron and scanning probe microscopies, quasi *in situ* X-ray photoemission, and *in situ* electrochemical Raman spectroscopy reveals the differences in the morphologies and chemical compositions of the nanocuboids formed at CO_2RR potentials *versus* Cu nanocubes prepared upon electrochemical cycling. These dramatic differences, together with the knowledge on Cu oxidation (Chapter 4), allow us to conclude on distinct mechanisms leading to the stabilization of their cubic shapes. The nanocuboids form upon polarization-driven re-organization of metallic Cu atoms. In contrast, Cu_2O nanocubes form upon Cu (electro-)dissolution/deposition cycles. The dissolution step can be enhanced in the presence of chloride additives, leading to larger cubes. Electrochemical cycling thus stabilizes Cu_2O cubic shape through surfactant-free thermodynamic crystal growth. The understanding of the Cu_2O nanocubes formation upon electrochemical cycling in Cu-free solutions opens the path for optimization of their synthesis. This comparative study elucidates the key factors for the formation of both nanocuboids and Cu_2O nanocubes and allows us to discard the hypothesis that the nanocuboid formation during CO_2RR is due to (electro)dissolution/deposition.

The results presented in this Chapter have been prepared in the form of a manuscript with the following working title: Karla Banjac*, Thanh Hai Phan, Fernando P. Cometto, Patrick Alexa, Yunchang Liang, Rico Gutzler, and Magalí Lingenfelder*, "Surface chemistry of copper micro- and nanocubic catalysts for electrochemical CO_2 reduction". Supplementary material is presented in Appendix C.

I acknowledge Dr. Fernando Cometto for his help with the analysis of XPS data, Dr. Patrick Alexa and Dr. Rico Gutzler (Max Planck Institute for Solid State Research, Germany) for their help with XPS measurements, and Dr. Yunchang Liang for helpful discussions on the interpretation of the electrochemical measurements.

5.1 Introduction

The formation of nanocuboids under CO_2RR conditions could be imagined as the growth of a few-nanometer large nanocubes from the Cu surface. Such surface transformation implies two possible scenarios – growth due to re-arrangement of the surface atoms or growth via electrodeposition.

The nanocuboids might form upon the re-arrangement of the atoms. Such atomic re-organization might vaguely be called surface reconstruction. Literature overview of UHV surface science on surface reconstruction reports no transformations of polycrystalline surfaces to the nanocuboids (or (100) facets in general).[128,129] Therefore, it is clear that the exposure of Cu to CO_2RR conditions is somehow related to nanocuboid formation. The first step toward the understanding of nanocuboid formation mechanism is thus to test the hypothesis on (electro)dissolution/deposition.

Electrodeposition is the formation of metal film on the substrate due to the reduction of dissolved metal species. Overviewing this definition in the context of nanocuboid formation, one realizes that such a process is possible only if dissolved Cu species were present in an electrolyte solution, as in the case of metal salt electrolytes. The premise that nanocuboids form during constant-potential CO_2RR upon electrodeposition seems implausible, especially as nanocuboid formation was observed *in situ* in Cu-free electrolytes (Chapter 3). What cannot be discarded is that Cu species form during CO_2RR due to dissolution or disintegration of Cu surface. Insurmountable obstacles to experimentally study the chemical composition of the electrical double layer and/or to detect Cu species therein (if any) motivate us to indirectly test this hypothesis by comparing the nanocuboids with electrochemically synthesized Cu nanocubes from Cu-free solutions.

The only NC synthesis method relying on sole electrochemical nanostructuration of polycrystalline Cu surfaces in Cu-free solutions is electrochemical cycling.[81,85,130] The cycling protocols employ polycrystalline Cu surfaces and chloride-containing electrolytes assuming that the NC precursor is CuCl. Cubic CuCl, presumed to be formed during an anodic scan, converts to Cu_2O NCs.[81,130] This hypothesis on CuCl→Cu_2O NCs transformation holds for CuCl nanoparticles precipitation in liquid-phase Cu_2O NC synthesis based on a hydrolysis approach[131]; however, it disagrees with the fact that chloride anions enhance anodic Cu dissolution. An alternative NC formation mechanism, proposed by Eilert *et al.*,[132] suggests that NCs form upon direct oxidation of Cu rather than upon CuCl precipitation, where a slow anodic ramp (*i.e.*, linear sweep voltammetry at low scan rate) is crucial for breaking the thin, interfacial passivation layer. Both mechanisms fail to explain the stabilization of the cubic morphologies.

Here, we conducted a comparative study of the morphologies and chemical compositions of the nanocuboids formed during CO_2RR and the nanocubes formed upon electrochemical cycling. A synergy of electrochemical characterization, microscopies, and *in situ* spectroscopies provides an insight into the complex interfacial processes over different lateral and depth scales, while simultaneously overcoming resolution and detection limits inherent to each individual technique.[133] Following the results on the anticorrosive properties of graphene towards electrochemical oxidation presented in Chapter 4, the G-Cu model system allows us to spectroscopically distinguish the differences in chemical composition between the Cu_2O NCs and the underlying Cu substrate, expected to remain metallic upon electrochemical cycling. Our results establish that the nanocuboid formation is due to the potential-driven re-organization of metallic Cu atoms. Moreover, we show that cubic morphology is inherent to cycling protocols that lead to Cu dissolution in the anodic scans and subsequently, to electrodeposition in the cathodic scans. Our findings discard the hypothesis that chloride-based scaffolds are needed for NC stabilization.

5.2 Experimental details

Sample preparation. Polycrystalline Cu samples annealed in a hydrogen atmosphere (for XPS measurements only) and graphene-covered polycrystalline Cu samples were purchased from Graphenea. Cu nanocuboids were prepared on G-Cu upon constant-potential polarization in 0.1 M CO_2 saturated $KHCO_3$ at −0.03 V *vs* RHE. Cu_2O NCs were prepared in 0.1 M CO_2 saturated $KHCO_3$ and 4 mM KCl/0.1 M CO_2 saturated $KHCO_3$ on G-Cu and polycrystalline Cu foils by electrochemical cycling in a potential window between −0.6 V and +0.6 V *vs* RHE or up to +0.9 V *vs* RHE at a sweep rate of 50 mV/s for five, twenty or 101 cycles.

Microscopies. More details on the set-ups and the workflows can be found in Chapter 2.

Image analysis. SEM images were used without any image processing. NC size was determined using Digimizer Software (MedCalc). For NCs shown in Figure 5.5 a), only NCs bigger than 25 nm were considered for the size analysis. Statistical analysis, shown in Figure 5.5, was performed based on three SEM images taken at three different positions along the same sample.

Quasi in situ XPS. To minimize sample oxidation, the samples, that were characterized by XPS, were prepared in the controlled environment and transferred to XPS through an air-free transfer system. A home-built sample transfer system between UHV and electrochemical environment[134] was implemented (Chapter 2). The samples were transferred to the XPS using a vacuum suitcase (Ferrovac). The XPS was conducted on a commercial Kratos AXIS Ultra system with a monochromatized Al Kα source with a base pressure in the lower range.

Workflow. XPS measurements were performed on G-Cu and hydrogen-annealed polycrystalline Cu foils purchased from Graphenea. For both G-Cu and Cu, we performed XPS characterization of four samples: (i) pristine, as-purchased sample, (ii) the sample after contact with an electrolyte, (iii) sample with nanocuboids, (iv) the sample after electrochemical cycling (Cu_2O nanocubes). XPS characterization for (i) and (ii) was conducted on the same sample. The sample was characterized by XPS, transferred back to the UHV-electrochemistry set-up using the vacuum suitcase, contacted with an electrolyte, transferred to XPS set-up, and characterized again.

The samples were first mounted on the sample holder[68] in air and then introduced to the transfer chamber with base pressure of 10^{-10} mbar. For the experiments on the samples that were in contact with an electrolyte (samples (ii), (iii), and (iv)), the electrochemical cell was mounted on the UHV-electrochemistry set-up, evacuated to $p \approx 10^{-2}$ mbar, and purged with argon. The electrolyte (0.1 M CO_2 saturated $KHCO_3$), counter electrode (coiled Pt wire), reference electrode (Ag/AgCl in 3 M KCl), and the drop maker were introduced into the cell, while purging with Ar. CO_2 was purged through a pre-saturated electrolyte in the as-assembled cell for 30 minutes. A drop of the electrolyte was formed on the sample using the drop maker; the meniscus was formed by lowering the sample with the drop close to the electrolyte surface. Once the experiment ended, the sample was washed by pushing Milli-Q water through the drop maker, dried with argon, and transferred to the transfer chamber with the base pressure of 8×10^{-8} mbar where it resided until transferred to the vacuum suitcase. For the samples that were in contact with an electrolyte without any electrochemical treatments, the sample was left in contact with an electrolyte for 10 minutes at open circuit potential.

Raman spectroscopy. All Raman spectra were collected with an inVia Raman spectrometer (Renishaw) coupled with a confocal microscope using 488 nm laser and 2400 lines/mm gratings. More details on the set-ups and the workflows can be found in Chapter 2.
Ex situ Raman spectra were collected using 50× objective (Leica) in the point map mode over 10×10 µm^2. Accumulation time was 5 seconds per spectrum. The spectra were collected in the following wavenumber ranges: range-1: 202–1700 cm^{-1} and range-2: 1500–2818 cm^{-1}.
For *in situ* electrochemical Raman experiments, spectra were collected using a water immersion objective (Leica, 64×) in line illumination mode (line length of ≈12 µm) in the spectral range 93.1–1629.6 cm^{-1}. Eight spectra in total were collected over 74.4 µm^2 surface area. Exposure time was 35 seconds per four spectra. *In situ* Raman spectra shown in Figure 5.4 were recorded during cycling voltammetry.

Data analysis. Spectra presented in Figure 5.4 were baseline corrected and smoothed. Fitting of the baseline was performed using an Intelligent fitting algorithm in the WiRE software (Renishaw): the backgrounds were fitted with a polynomial value of 11 and noise tolerance of 1.50. Polynomials of order 11 fit well for all spectra.

5.3 Results

5.3.1 Morphology differences

Figure 5.1 compares the morphologies of the nanocuboids formed during constant-potential CO_2RR and the NCs prepared upon electrochemical cycling. The nanocuboids were prepared upon constant-potential polarization of G-Cu in 0.1 M CO_2 saturated $KHCO_3$. AFM images showing G-Cu after the nanocuboid formation reveal that the initial flat Cu surface becomes granular (Figures 2.13, 3.1, and 5.1). High-resolution EC-STM images of the Cu surface underneath graphene reveal Cu nanocuboids as (100) facet multilayers with lateral sizes between 4 nm and 30 nm. These findings show that the nanocuboids form on the Cu surface rather than on top of graphene.

When turning to the electrochemical cycling protocol, NCs were synthesized by electrochemical cycling of G-Cu in 0.1 M CO_2 saturated $KHCO_3$ (Figure 5.1). After five cycles, NCs with ≈ 25 nm edge-length are sparsely distributed along G-Cu sample. NCs are on top of graphene. Their high mobility during AFM imaging suggests that as-prepared NCs weakly

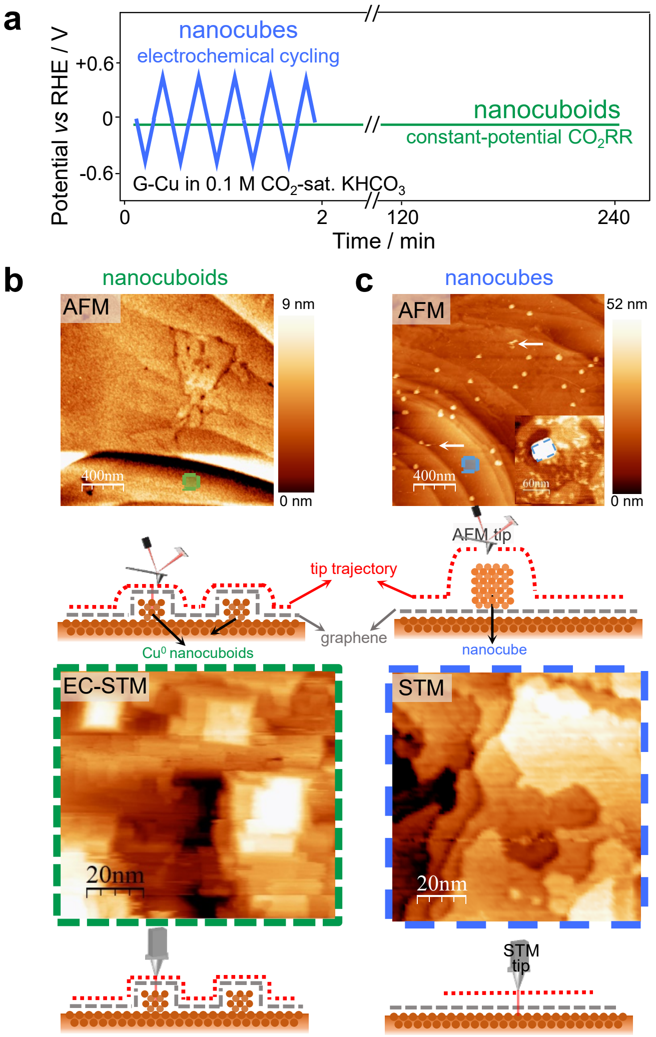

Figure 5.1 – **Morphology of Cu nanocuboids formed under CO_2RR conditions *versus* NCs prepared upon electrochemical cycling.** (a) Comparison of electrochemical conditions for the formation of Cu nanocuboids and NC synthesis through electrochemical cycling. For Cu nanocuboids: constant-potential polarization at -0.03 V *vs* RHE. For NC synthesis: electrochemical cycling of G-Cu between -0.6 V and $+0.6$ V *vs* RHE. An electrolyte in both protocols: 0.1 M CO_2 saturated $KHCO_3$. (b) Morphology of the nanocuboids: AFM and EC-STM images together with the corresponding schemes. (c) Morphology of NCs prepared upon electrochemical cycling: AFM height image with white arrows denoting the scan lines in which the AFM tip moved the NCs. Inset: AFM image showing a single NC. STM image shows the polycrystalline Cu underneath graphene after cycling up to 0.9 V *versus* RHE in 0.1 M CO_2 saturated $KHCO_3$. The regions marked on AFM images with squares are superimposed to highlight the size differences between AFM and STM images.

interact with graphene. STM reveals that the Cu surface underneath graphene remains flat and polycrystalline after five cycles (Figures 5.1 and C.1), further supplementing *in situ* Raman results on anticorrosion properties of graphene for electrochemical Cu oxidation.

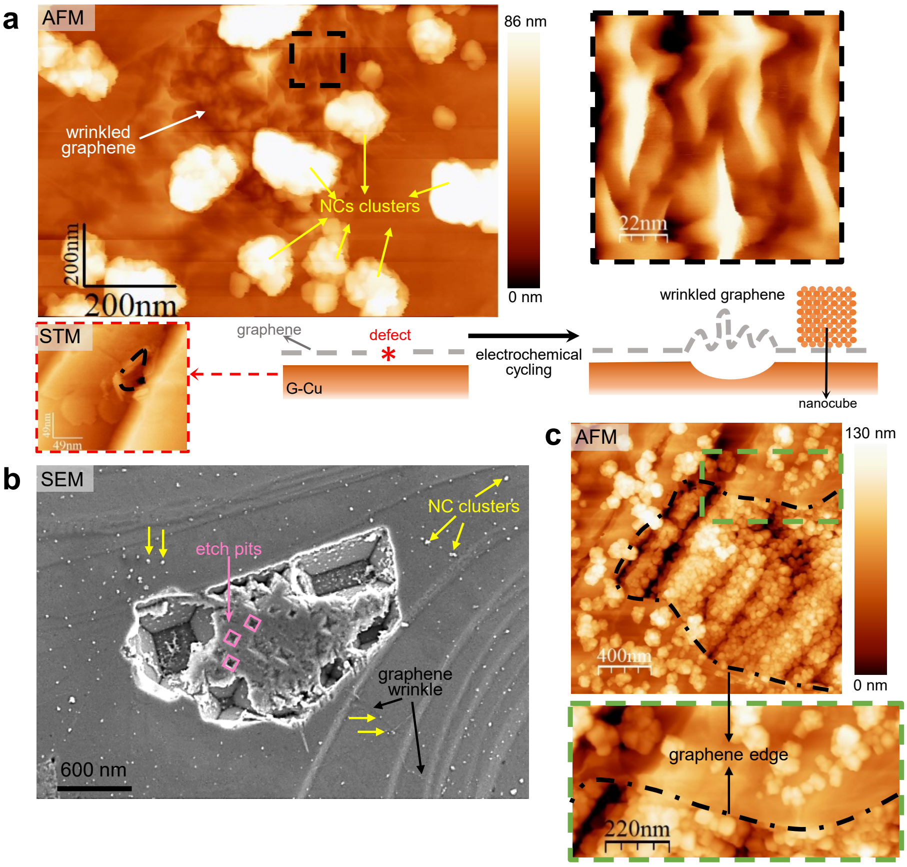
a
AFM
wrinkled graphene
NCs clusters
200nm
200nm
86 nm
0 nm
22nm
STM
49nm
graphene
defect
G-Cu
electrochemical cycling
wrinkled graphene
nanocube
b
SEM
etch pits
NC clusters
graphene wrinkle
600 nm
c
AFM
130 nm
0 nm
400nm
graphene edge
220nm

Figure 5.2 – **Nanocube clusters prepared upon electrochemical cycling on top of graphene.** (a) AFM image of NC clusters and the wrinkled graphene together with the corresponding scheme. NC clusters form on top of graphene around on undulation in the Cu surface covered with wrinkled graphene. Bottom: STM image showing the patch of exposed Cu surface and unfolded graphene (denoted with dotted line). (b) SEM images showing the NC clusters and the etch pits formed on G-Cu. (c) AFM images showing NC clusters on top of graphene and around the graphene edge.

Any changes in the cycling protocol significantly affect NC size and coverage, both increase with the number of the cycles. Also, the well-defined etch pits formed on Cu after 101 cycles suggest that NC formation is closely associated with surface dissolution of uncovered Cu areas and through graphene defects (Figure 5.2). Furthermore, the increase in the oxidation vertex potentials results in NCs clusters rather than stand-alone NCs that form for oxidation vertex potentials up to +0.6 V *vs* RHE (Figure 5.2). These clusters are situated around wrinkled graphene areas, likely formed upon relaxation of graphene over the shallow Cu etch pit. Additional AFM images of NCs clusters confirm that NCs preferentially form close to the graphene defects (Figure 5.2 c)).

The key parameter for electrochemical cycling is the anodic scan. No NCs were formed when restricting the potential window below the Cu dissolution potential: for example, in an attempt to prepare NCs through electrochemical cycling between −0.7 V and +0.2 V *vs* RHE (Figure C.2).

5.3.2 Chemical composition differences

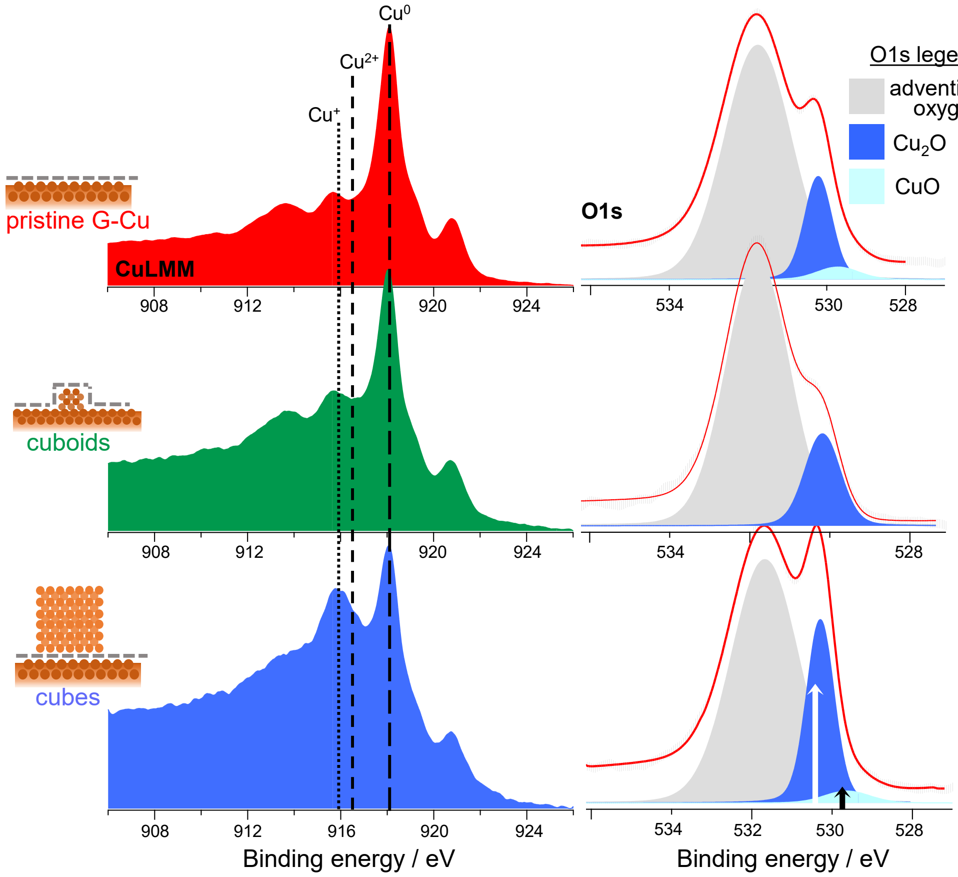

Figure 5.3 – **(Quasi) *in situ* XPS: Cu nanocuboids *versus* Cu_2O NCs prepared upon electrochemical cycling.** Quasi *in situ* XPS spectra of as-received G-Cu, G-Cu sample after Cu nanocuboid formation, and the NCs prepared on G-Cu upon electrochemical cycling. Left panel: Cu LMM Auger spectra. Right panel: O1s spectra. The arrows denote the increase in Cu_2O and CuO components of the O1s peak for Cu_2O NCs.

The chemical composition of G-Cu before and after being in contact with the electrolyte, the Cu nanocuboids, and NCs prepared upon cycling were studied by quasi *in situ* XPS (Figure 5.3). The UHV-electrochemistry set-up[134] allows control over the atmosphere conditions during the sample preparation (conducted inside the UHV-compatible electrochemical cell saturated with CO_2), direct sample transfer to the UHV environment, and air-free transfer to the XPS set-up.

The Cu LMM Auger spectra were used to determine the occurrence of Cu^{2+}/Cu^{+} species (predominant peaks at 918.4 eV, 916.5 eV, and 917.8 eV are related to metallic Cu, Cu^{+}, and Cu^{2+}, respectively), while the O1s spectra were employed to assess the presence of the oxygen-containing species (Table C.1).[70,135] The O1s peak centered at ≈ 532 eV (marked in grey) remains constant for all treatments; it is related to adsorbed H_2O/OH species[136] with a minor contribution from intrinsic graphene defects[65] (consistent with the C1s spectra in Figure C.5, showing a dominant C sp^2 peak and minor contributions from C=O and C–O). On the other hand, the O1s peaks at 530.2 eV and 529.7 eV are attributed to the presence of Cu_2O and CuO, respectively.[65,70] Further discussion on XPS assignment is reported in Section C.

The pristine G-Cu sample is slightly oxidized with a dominant Cu LMM signal from metallic Cu and a minor amount of Cu^+ species. As discussed in Chapter 4, Cu_2O forms upon air oxidation through the intrinsic graphene defects (Figure 4.7). After constant-potential polarization (*i.e.*, Cu nanocuboids), the CuO species are fully reduced and the amount of Cu_2O decreases. This is consistent with *in situ* Raman spectra showing the complete reduction of Cu_xO during the formation of Cu nanocuboids (Figure 3.5 a)). The small amount of Cu_2O in the O1s signal in Figure 5.3 probably formed upon washing with non-degassed Milli-Q water. In agreement with AFM (Figure 5.1 a)), STM results, and Raman spectra, the C1s spectrum obtained on G-Cu after Cu nanocuboid formation confirms that this potentiostatic treatment creates no additional defects in graphene (Figure C.5). The nanocuboids are thus metallic and fully covered by graphene. In contrast, XPS CuLMM spectrum of NCs prepared upon electrochemical cycling shows a decrease in metallic Cu *vs* Cu^+ ratio. A simultaneous increase in the Cu_2O and a small CuO O1s components after the cycling protocol confirms the formation of Cu_2O NCs.

As a control experiment aiming to test the role of graphene on the chemical identity of Cu_2O NCs, we performed the same experiments on hydrogen-annealed polycrystalline Cu foils without the graphene (Figure C.6). The Cu surface remains mostly metallic upon the nanocuboid formation, while similar trends in the increase of the Cu_2O component in the O1s spectra and the Cu *vs* Cu^+ ratio decrease observed after electrochemical cycling confirm differences between the chemical compositions of the nanocuboids formed during CO_2RR *vs* Cu_2O NCs prepared upon electrochemical cycling.

To gain further insights into Cu_2O NCs formation upon electrochemical cycling, we tracked the changes in the chemical state of G-Cu during the first cycle using *in situ* Raman spectroscopy (Figure 5.4). Characteristic Raman signatures of Cu_2O and graphene allow us to investigate simultaneously the oxidation state of Cu and the stability of graphene. Raman spectra were recorded at different potentials as G-Cu electrode was cycled in 0.1 M CO_2 saturated $KHCO_3$ between $-0.6\,V$ and $+0.9\,V$ *vs* RHE. The spectra acquired without applied electrical potential (*i.e.*, at open circuit potential) reveal the presence of the Cu_2O band[137,138] ($645\,cm^{-1}$) and the G band of graphene at $1585\,cm^{-1}$. This result, together with XPS results for the G-Cu before and after the contact with an electrolyte (Figure C.4), suggests that pristine G-Cu is slightly oxidized due to air oxidation. The native oxide gets fully reduced during the cathodic scan at potentials less negative than $-0.1\,V$ *vs* RHE. As discussed in Chapter 5, Cu under graphene remains metallic for LSV sweeps up to $+0.9\,V$ *vs* RHE. Simultaneous appearance of the anodic CV peaks suggests oxidation of Cu surface exposed through graphene defects (*e.g.*, STM image in Figure 5.2 a)).

5.3.3 Effect of chloride on Cu_2O cube formation

Literature reports that Cu_2O cubes form from the CuCl cubic scaffolds.[36,81] To investigate this hypothesis, we examined the effect of chloride additives on Cu_2O cubes preparation. NCs were prepared upon electrochemical cycling between $-0.6\,V$ and $+0.9\,V$ *vs* RHE in chloride-free 0.1 M CO_2 saturated $KHCO_3$ (Figure 5.5 a)) and in 4 mM KCl/0.1 M CO_2

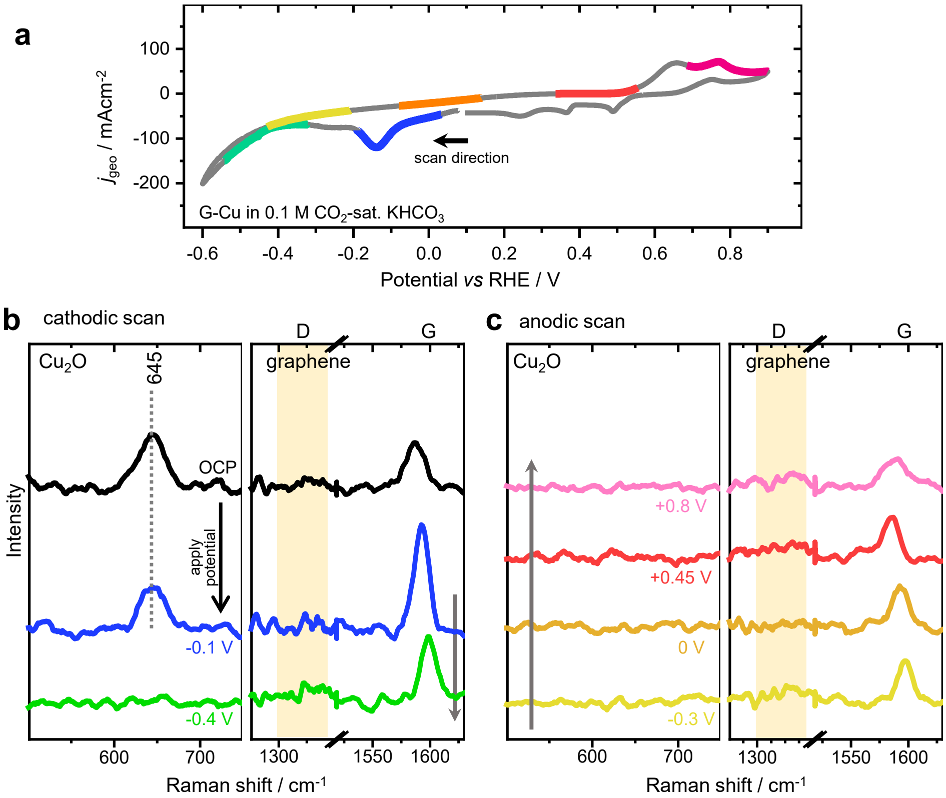

Figure 5.4 – ***In situ* Raman spectroscopy insights during the electrochemical cycling protocol.** (a) Cyclic voltammetry of G-Cu in 0.1 M CO_2 saturated $KHCO_3$ recorded at 5 mV/s. Different colors denote the potential range at which the Raman spectra, shown in (b) and (c), were recorded. b) Raman spectra obtained at open circuit potential (OCP) and during cathodic scan. (c) *In situ* Raman spectra obtained in anodic scan. All spectra are background subtracted and vertically shifted. The potentials are reported on the RHE scale.

saturated $KHCO_3$ (Figure 5.5 b)). SEM was used to characterize the NCs prepared on polycrystalline Cu foils after 101 cycles, AFM was used to visualize the NCs prepared on G-Cu after five cycles.

Nanoparticle cubic contours are discernible on both Cu foil and G-Cu cycled in the chloride-free electrolyte, which suggests that nanoparticles are formed upon cycling regardless of the electrolyte composition. Both SEM and AFM reveal that NCs synthesis in the chloride-containing solutions yields high coverage of large, well-defined NCs.

5.4 Discussion and conclusions

The combination of electron and scanning probe microscopies characterization with (quasi) *in situ* spectroscopy highlight the morphological and composition differences between Cu nanocuboids and NCs prepared upon electrochemical cycling. Moreover, we employ G-Cu as a model system that allows us to distinguish the differences in surface processes leading to formation of Cu nanocuboids during CO_2RR *versus* the ones resulting in Cu_2O NC

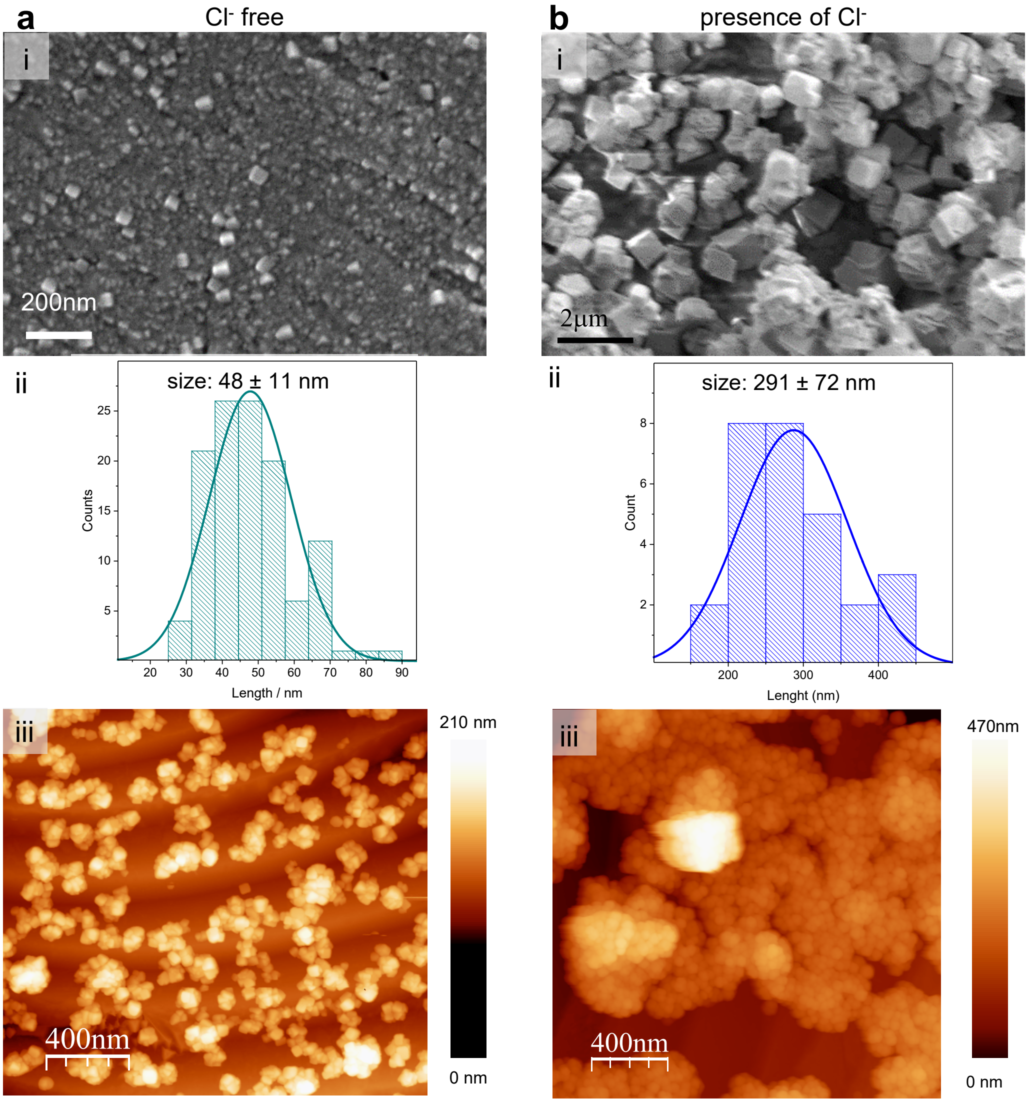
a
Cl- free
b
presence of Cl-
i
200nm
i
2µm
ii
size: 48 ± 11 nm
Counts
5
10
15
20
25
20
30
40
50
60
70
80
90
Length / nm
ii
size: 291 ± 72 nm
Count
2
4
6
8
200
300
400
Lenght (nm)
iii
400nm
210 nm
0 nm
iii
400nm
470nm
0 nm

Figure 5.5 – **Effect of chloride on the Cu_2O NC formation.** (a) Cu_2O NCs synthesized in a chloride-free electrolyte. (b) Cu_2O NCs synthesized in a chloride-containing electrolyte. Panels *i*: SEM images of the Cu_2O NCs prepared upon electrochemical cycling of polycrystalline Cu foils. Panels *ii*: Cu_2O NC size distribution. Panels *iii*: AFM images of Cu_2O NCs on graphene synthesized upon electrochemical cycling.

formation on top of graphene upon cycling. This approach gives an unprecedented insights into both formation mechanisms.

Cu-based CO_2RR catalysts enrich in Cu nanocuboids during CO_2RR (Figure 5.6). Nanocuboids are (100) facet multilayers with lateral dimensions smaller than 100 nm. Their heights and lateral sizes strongly depend on the initial state of the surface and CO_2RR conditions (electrolyte, potential, polarization time). Nanocuboids lose their square contours upon air oxidation and thus, appear as the granular structures in *ex situ* AFM studies (Figures 3.1 and 5.1). This highlights the importance of the *in situ* surface-sensitive studies for understanding the nanocuboid formation during CO_2RR.

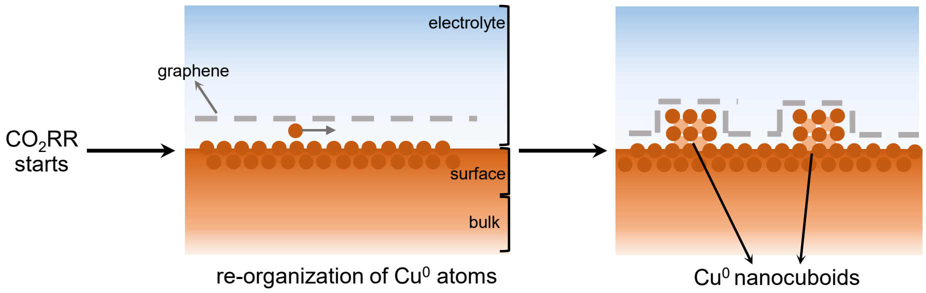

Figure 5.6 – **Cu nanocuboid formation under CO_2RR conditions.** Scheme showing the formation of Cu nanocuboids on G-Cu under CO_2RR conditions.

Both (quasi-) *in situ* XPS (near-surface sensitive) and Raman (far-surface sensitive) spectroscopy, presented in Chapter 3, confirm that nanocuboids are metallic Cu(100) facet multilayers (*i.e.*, mounds). It should be noted here that our main conclusion on the nanocuboid metallicity relies on EC-STM and *in situ* Raman studies (Chapter 3). Metallicity of Cu top-most surface layers after CO_2RR at the potentials less negative than 0 V *vs* RHE is further confirmed by a recent XPS study,[139] where the main differences between experimental procedures reported here and in reference 139 are washing steps and transfer procedures. This further demonstrates fast oxidation of the nanocuboids and highlights the importance of controlled sample transfer.[67] Additionally, the nanocuboids form underneath graphene if using G-Cu. These results suggest that the nanocuboids form upon potential-driven re-organization of metallic Cu atoms, in agreement with *in situ* GIXRD studies[100] reporting on enrichment of polycrystalline Cu with Cu(100) as a surface phenomenon occurring within 2.5 nm in depth from the top surface and *in situ* SEM studies[88] revealing surface reconstruction under CO_2RR conditions.

When turning to the electrochemical cycling protocol, we demonstrate the preparation of the Cu_2O NCs both in the chloride-free and chloride-containing electrolyte. This finding is in the agreement with the recent reports by Arán-Aris *et al.*[140] and Grosse *et al.*,[141] who reported on the Cu_2O NCs formation upon cycling in the chloride-free and chloride-containing electrolyte.[132] These results disprove the hypothesis that CuCl determine the cubic morphology of the as-formed NCs.[36,81]

From the above results, we propose the formation mechanisms of Cu_2O NCs on G-Cu as shown in Figure 5.7. In the anodic sweep, the Cu exposed to the electrolyte through graphene defects dissolves,[142] while Cu underneath graphene remains mostly metallic due to the anticorrosive properties of graphene. This suggests that the exposed Cu areas act as the local Cu ions sources, while Cu underneath defect-free graphene remains Cu^0. Reduction of Cu ions, formed upon dissolution, results in electrodeposition of the nuclei on top of graphene in the cathodic sweep.

This mechanism also describes well Cu_2O NCs formation on a Cu foil. Our results suggest that the stabilization of Cu_2O(100) facets upon dissolution/electrodeposition[37] cycles seems more likely than the direct oxidation to Cu(II) carbonate-hydroxide NCs as suggested in the reference 132. The same mechanism also explains the formation of Cu_2O NCs prepared upon cycling to oxidation potentials >+0.8 V *vs* RHE, where Cu dissolution

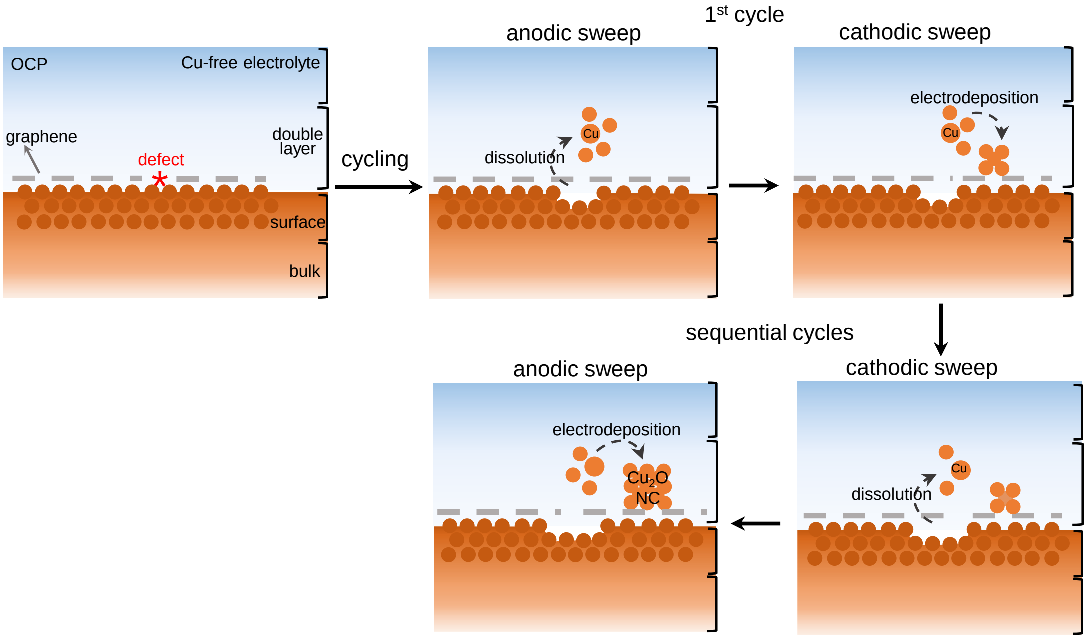
1st cycle
anodic sweep
cathodic sweep
OCP
Cu-free electrolyte
graphene
defect
double layer
surface
bulk
cycling
dissolution
Cu
electrodeposition
Cu
sequential cycles
anodic sweep
cathodic sweep
electrodeposition
Cu$_2$O NC
dissolution
Cu

Figure 5.7 – **Formation of Cu_2O NCs during electrochemical cycling.** Scheme showing local dissolution of Cu species in the anodic sweep followed by electrodeposition in the cathodic sweep. Sequential stripping/electrodeposition cycles stabilize cubic morphology of the crystals.

to Cu^{2+} ions leads again to the electrodeposition in the cathodic sweep. We highlight that complex oxidation processes[143] occurring under different experimental conditions, including different scan rates and cycling potential ranges,[140] might change the formation mechanism as well as the observed nanoparticle morphology. Moreover, NCs growth from Cu surface suggests direct electrodeposition, homoepitaxial growth of the first layer, and the stability of as-grown NCs towards detachment.

Our observations rule out the exclusive role of chloride in the Cu_2O NCs formation. Chloride, often used as additive in electrochemical cycling protocols, changes the oxidation mechanism and enhances the dissolution in the anodic scan.[144] High concentration of as-dissolved Cu species in the double layer leads to a situation similar as if starting with Cu^{2+}-containing solution reported in references 140 and 141. In both cases, Cu nuclei deposited in the cathodic scan grow in each sequential anodic scan. Cube morphology is a direct consequence of the thermodynamic stability of the $Cu_2O(100)$ facets, where the surface energies of Cu_2O increase in the following order: $(100) < (111) < (110)$.[145] Therefore, Cu_2O NC synthesis upon electrochemical cycling is an example of a thermodynamically controlled scenario. This further demonstrates that the NC morphology is inherent to the cycling protocols. Similarities in the NCs formation mechanism prepared upon the electrochemical cycling protocols in Cu-free and Cu-containing solutions[140] allow further optimization of NC synthesis.[141]

Surface physics Part IV

6 *In situ* surface physics: Mechanism of Cu nanocuboid formation during CO_2RR

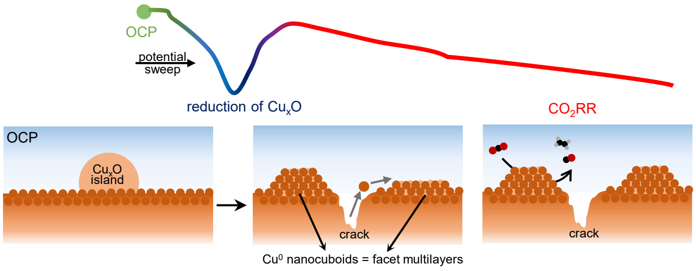

Chapter 3 shows that Cu-based CO_2RR catalysts undergo a dramatic evolution resulting in the reduction of (native) Cu oxide and the emergence of Cu nanocuboids. Surface chemistry insights in Chapters 4 and 5 revealed that the nanocuboids form upon potential-driven re-organization of metallic Cu atoms. Here, we explain the surface physics behind their formation. *In situ* EC-STM studies show that surface cracking followed by nanocuboid formation is the main structural transformation related to the reduction of (native) Cu oxide. By disclosing the similarities in the atomistic details between the nanocuboid formation and homoepitaxial mound formation through kinetic roughening, we present a unique framework for the interpretation of *in situ* structural transformations associated to Cu_xO reduction. These results, taken together with the literature on oxide-derived Cu catalysts, suggest that Cu mounds are the active sites for CO_2RR. This study further supports the hypothesis on the active sites formation during preparation or testing of Cu catalysts, agrees with the available *in situ* studies on the surface reconstruction, and encourages future fundamental theoretical and experimental studies addressing open questions on the correlation between surface evolution and Cu-catalyzed CO_2RR.

The content of this Chapter has been adapted from the manuscript in preparation: **Karla Banjac***, Thanh Hai Phan, Fernando P. Cometto, and Magalí Lingenfelder, “Homoepitaxy processes during CO_2 electroreduction on polycrystalline Cu surfaces”.

I acknowledge Stefan J. Raaijman and Chunmiao Ye for their help with the CO_2RR product analysis experiments conducted in the laboratory of Professor Marc Koper at University of Leiden, Professor Marc Koper for his collaborative support, Dr. Da-Jiang Liu (Iowa State University, U.S.), Professors James Evans (Iowa State University, U.S.) and James De Yoreo (Pacific Northwest National Laboratory, and University of Washington, U.S.) for fruitful discussions on the formation mechanism.

6.1 Introduction

Chapter 3 introduced the structural transformation that polycrystalline Cu surfaces undergo under CO_2RR conditions. Cu nanocuboids form upon potentiostatic polarization at potentials beyond Cu_xO reduction. EC-STM studies revealing the *in situ* dynamics of the nanocuboid formation show that the nanocuboids are Cu(100) facet multilayers, *i.e.* mounds. The appearance of mounds implies a kinetic roughening process.

Kinetic roughening is a special case of multilayer growth, in which a barrier at the step edge (Ehrlich-Schwoebel barrier[146,147]) inhibits transport of the adatoms across the descending step-edge. Inhibition of downward transport causes a mass transport in the uphill direction. This growth instability leads to the formation of island multilayers, *i.e.* mounds. Three microscopic phenomena are characteristic for kinetic roughening. First, nucleation and transformation of the as-formed adatom nuclei into two-dimensional islands. Second, island coarsening proceeding either via Ostwald ripening or via Smoluchowski ripening. In Ostwald ripening, the adatoms dissociate from the small islands and re-attach to the large island.[148,149] In Smoluchowski ripening, for the first time confirmed in Ag/Ag(100)[150–152] and Cu/Cu(100)[153] homoepitaxy studies, the islands composed of several hundreds atoms diffuse along the surface until colliding and combining with another island. Third, simultaneous growth-induced coalescence, rapid reshaping, and multilayer growth.

This Chapter presents an EC-STM study showing the process of nanocuboid formation. High-resolution EC-STM images show the diffusion of Cu species from surface cracks at t_0. This mass transport event leads to the formation of (100) facet multilayers, *i.e.* mounds, on the terraces surrounding the cracks. EC-STM images obtained over 14 minutes show the atomistic details of the mound formation, greatly resembling kinetic roughening. Literature overview, together with the results presented in Chapters 3 and 4, suggest that the mass transport event at t_0 might be triggered by the reduction of native Cu_xO. We therefore conclude that the mound, formed upon $Cu_xO \rightarrow Cu$ reduction, are universal CO_2RR active sites present on all Cu catalysts under reduction potentials.

6.2 Experimental procedures

EC-STM. EC-STM images were obtained on G-Cu in 0.1 M CO_2 saturated $KHCO_3$ during potentiostatic polarization at $-1\,\text{V}$ *vs* Pt pseudo-RE.

Image analysis. To quantify the mass transport event and correlate it with the mound formation, a surface groove was chosen as the point of reference for the analysis. Depths of the surface groove were estimated from the apparent height profiles drawn in the direction perpendicular to the scan lines. The apparent height profiles shown in Figure 6.2 were drawn in the direction of the scan lines. For consistency, the apparent heights of the terraces were determined as the differences of the apparent heights measured at the lowest point of the groove ($x_{1,\text{groove}}$) and $x_{0,\text{left}} = 5\,\text{nm}$ ($x_{0,\text{right}} = 45\,\text{nm}$) for the left (right) edge. Quantitative analysis correlating the mass transport with the mound formation was performed from the relative changes of the apparent heights of the terraces above the groove. The number of mound layers was then calculated by dividing the relative changes of the apparent heights of the terraces by the Cu(100) interlayer spacing (1.8 nm). Relative change in surface areas during mound formation were calculated using Ironed surface area algorithm in WSxM software.[51]

We labeled mound layers by an index i=0, 1, 2, ... with i=0 denoting the substrate. If the substrate layer was imperceptible, the mound layers were labeled by an index i=n, n+1, n+2, ... , with n denoting the first distinguishable mound layer. Moreover, the images denoted with t_0 are the first ones in the set of the EC-STM images showing the selected surface area.

Product analysis. Before each experiment, the glassware and the electrochemical cell were either soaked in a $1\,\mathrm{g\,L^{-1}}$ acidic $KMnO_4$ solution or boiled in a mixture of concentrated H_2SO_4 and 30% H_2O_2. If soaked overnight in $KMnO_4$, the glassware and the cell were rinsed with Milli-Q water and then submerged in a diluted, acidic H_2O_2 solution. The final cleaning step is the same for both procedures: the glassware and the cell were three times boiled in Milli-Q water. Gas product analysis was conducted custom-made, two-compartment electrochemical cell, where the gas compartment of the working electrode compartment was connected via an automatic sampling loop to the gas chromatograph (Section 2.3.2). Hydrogen-annealed polycrystalline Cu foil and G-Cu (both purchased from Graphenea) were used as the working electrodes; leakless Ag/AgCl reference electrode immersed in 3.4 M KCl (model ET072, eDAQ) was used as the reference electrode; a coiled Au wire was used as the counter electrode. The electrolyte (0.05 M $KHCO_3$) was purged with CO_2 (Linde 4.5) for at least 20 minutes before each experiment. A set of seven chronoamperometric CO_2RR electrolyses, each run at $-0.03\,\mathrm{V}$ *vs* RHE for 1 hour, was conducted on the same working electrode. After each electrolysis, the sample was kept under open circuit potential conditions and an aliquot of the gas sample from the cathodic compartment was analyzed using gas chromatography. The electrolyte was then re-purged with CO_2, and CO_2RR was re-started at $-0.03\,\mathrm{V}$ *vs* RHE. This sequence was repeated seven times.

6.3 Results

6.3.1 Mound formation over hundred-nanometer scale: Implications of the mechanism

In situ EC-STM studies reveal that the nanocuboids are Cu mounds. The mounds generally have square contours; they also appear as elongated rectangles. In both cases, their near-square shape indirectly implies that they are (100) facet multilayers. Moreover, triangular (111) mounds are very rarely observed and correspond to mounds formed on (111) crystalline grains of the Cu substrate (Figure D.1). To investigate whether they form uniformly

the G-Cu sample (Figure 6.1 a)). The mounds were usually found at several positions along the sample, whereas many areas of the Cu surface remained unchanged with respect to the initial morphology. Interestingly, the areas in which the mounds were not found often remained unchanged over several hours (see, for example, the Cu step edge bunches in Figure D.2). This result implies that the mounds do not form uniformly over the whole surface. Their formation is thus a local phenomenon.

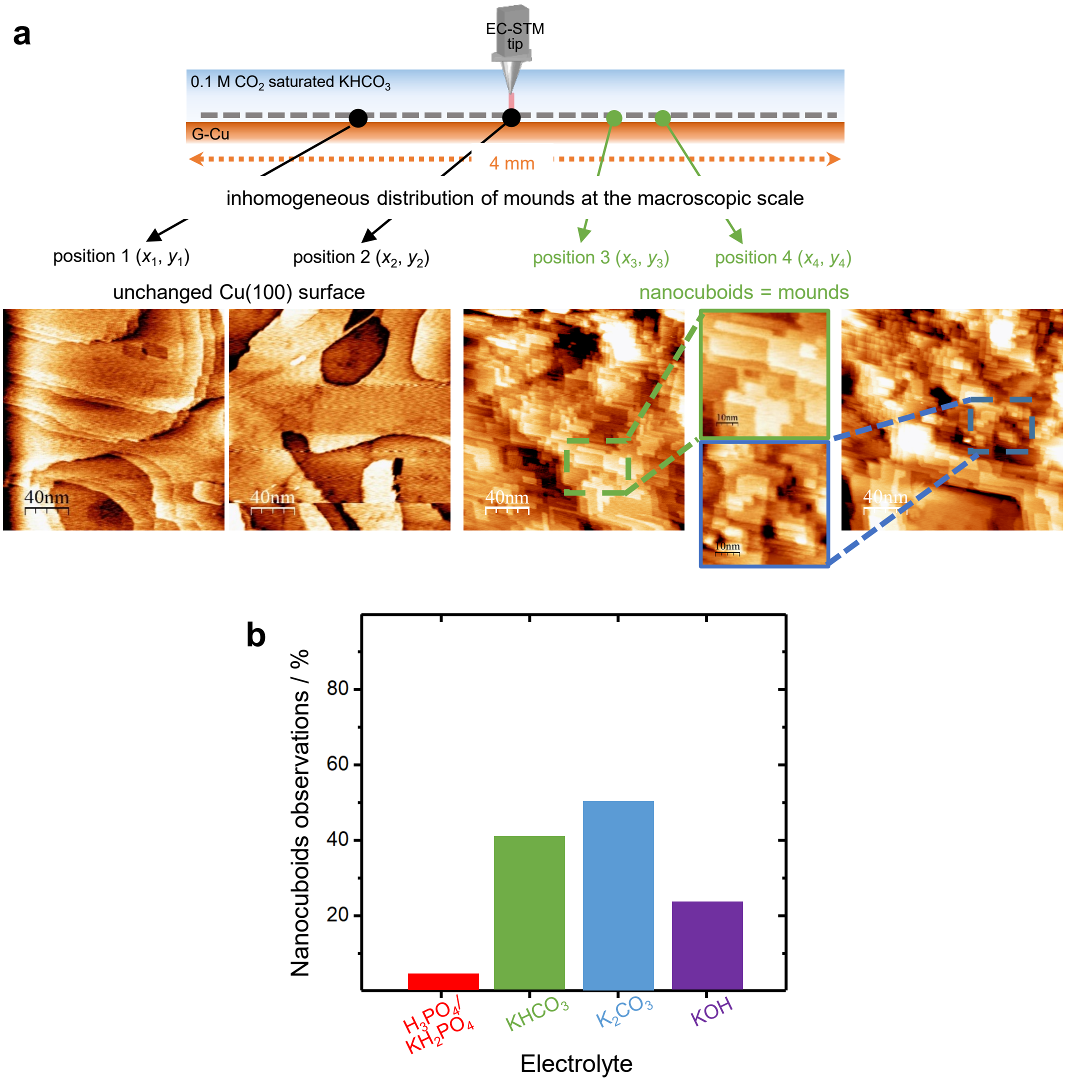

Figure 6.1 – **Inhomogeneous spatial distribution of Cu mounds**. (a) Scheme of EC-STM imaging at four (x, y) positions along the G-Cu sample and the corresponding EC-STM images. The images on the left are examples of surface areas (positions 1 and 2) that remain unchanged, whereas those on the right show surface areas (positions 3 and 4) where the mounds are found. EC-STM images were obtained along the same G-Cu sample upon constant-potential CO_2RR in 0.1 M CO_2 saturated $KHCO_3$ at $-1\,V$ *vs* Pt pseudo-RE. (b) Success rate of the EC-STM observations of Cu mounds, calculated as the ratio of the number of times that the mounds were observed and the total number of EC-STM measurements performed on G-Cu in each electrolyte.

To quantitatively illustrate this phenomenon, we count the successful EC-STM observations, *i.e.*, EC-STM experiments in which we observed nanocuboids, and the unsuccessful ones (Figure 6.1 b)). We define the successful mound observations as those in which the mound contours are clearly visible. The success rates were then calculated as the ratios of the number of times that the mounds were observed and the total number of EC-STM measurements performed on G-Cu in each electrolyte. The mounds were found in less than 50% of the experiments (Figure 6.1 b)) with the lowest number of the mound observations in H_3PO_4/KH_2PO_4, also connected with the fact that high resolution imagining is more challenging at low pH due to the instability of coined metals.

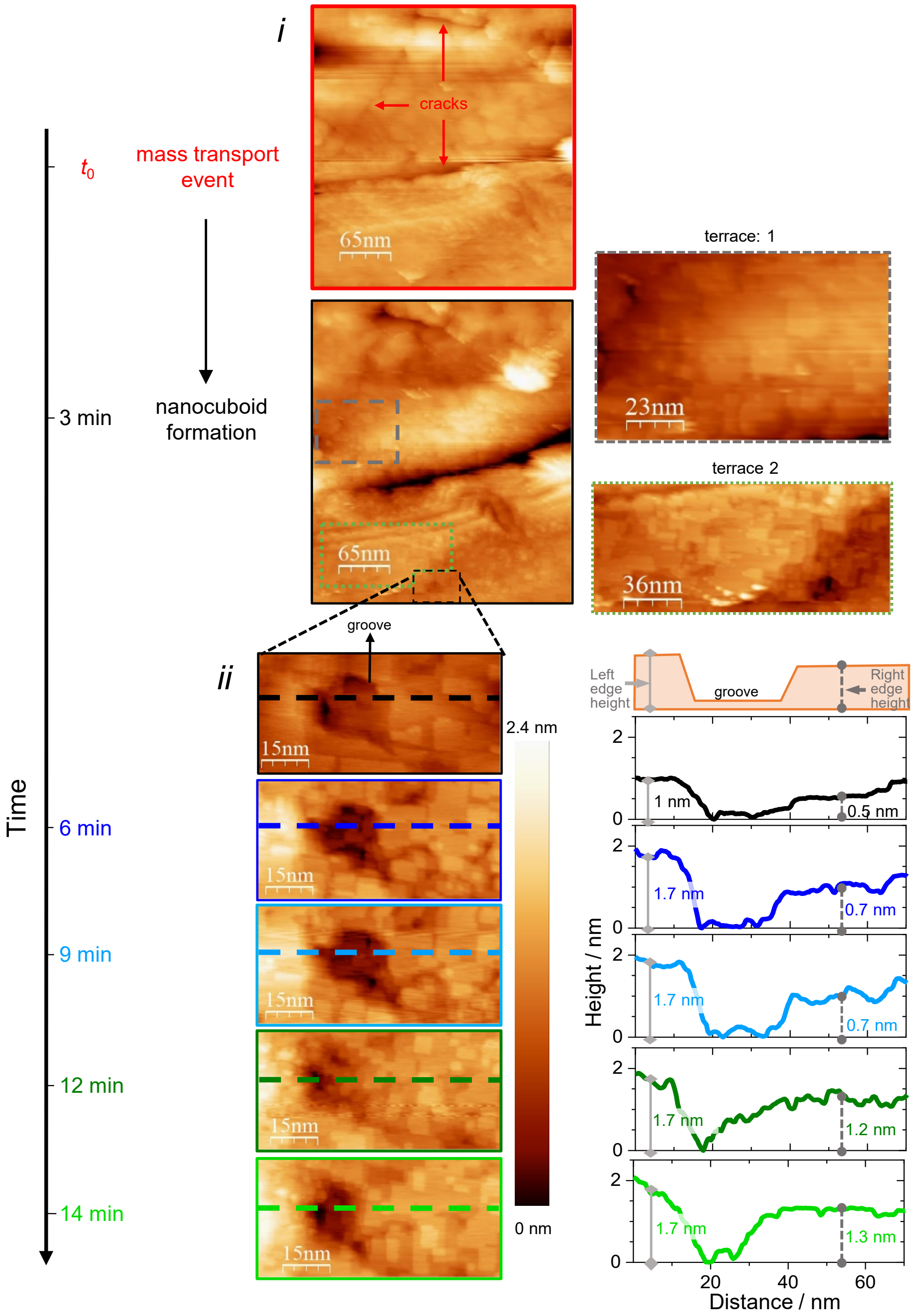
i
cracks
65nm
t0
mass transport event
nanocuboid formation
3 min
terrace: 1
23nm
terrace 2
36nm
65nm
groove
ii
15nm
2.4 nm
0 nm
Time
6 min
9 min
12 min
14 min
Left edge height
groove
Right edge height
1 nm
0.5 nm
1.7 nm
0.7 nm
1.7 nm
0.7 nm
1.7 nm
1.2 nm
1.7 nm
1.3 nm
Height / nm
0
2
20
40
60
Distance / nm

Figure 6.2 – **Initial stages of Cu mound formation.** Consecutive EC-STM images showing the mound formation. Panel *i*: EC-STM images showing the mass transport event at t_0 and the mounds on the adjacent terraces. Panel *ii*: EC-STM images showing the formation of mounds above the groove and corresponding apparent height profiles. Images were scaled to the same color scale.

A detailed analysis of the cases where the mounds were found allowed us to identify that mounds form close to surface cracks. For example, EC-STM image obtained at t_0 shows three cracks 1.5 nm to 6 nm deep and meeting at an angle of $\approx 60°$ (Figure 6.2). This image appears blurry due to significant mass transport from the cracks. Consequent images, obtained over the next 12 minutes, reveal the formation of mounds on terraces adjacent to the cracks. Any further changes of the surface crack, including its deepening, its broadening, and nanostructuring of its internal walls, are untraceable by EC-STM due to the instabilities caused by rough surfaces and high mass transport. We thus focus our further analysis on the small surface groove. This position is taken as a reference point to correlate the mass transport event with the mound formation, where the mounds grow above the groove's edges.

Mass transport events from the cracks across the Cu surface lead to the evolution of the surface groove and the formation of mounds (Figure 6.2, panel *ii*). First, the groove itself shrinks as the mounds form during 12 minutes: its lateral size goes from ≈ 15 nm to ≈ 5 nm. This shrinkage is mostly due to growth of the mounds on the terraces above the groove's right edge. Second, the initially featureless sidewall turns into a nanostructured one, again due to the mound formation. This is especially evident from the EC-STM image at $t_0 + 12$min and corresponding apparent height profile, which exhibits angstrom-high perturbations along the sidewalls. The terraces above the groove's edges appear brighter on EC-STM images as the mounds are formed on them. Such increase in brightness is due to the increase of their respective apparent heights. In other words: assuming that the substrate layer is stable and always of the same height, adatom mass transport and decrease of the groove size is related to the epitaxial growth of mounds.

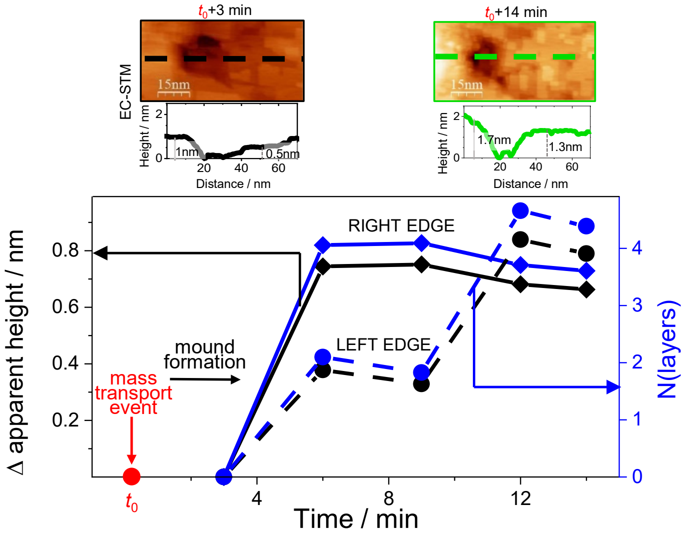

Figure 6.3 – **Evolution of the surface groove during mound formation.** The apparent heights of the terraces surrounding the surface groove as a function of time and correlation with the number of surface layers that get deposited. The first and the last EC-STM images obtained at $t_0 + 3$ min and at $t_0 + 14$ min are same as in Figure 6.2.

To correlate the mass transport event and the mound formation, we analyzed the apparent heights of the terraces above the groove during mound formation (Figure 6.3). The changes in the apparent heights of the terraces are correlated with the number of surface layers that get deposited. Rapid mound formation above groove's left edge corresponds to the deposition of four surface layers over three minutes. Mound growth over the groove's right edge proceeds at a slower rate: first, two layers are deposited over first three minutes and then, two additional layers are deposited between 9th and 12th minute. Differences in the growth rates might be related to the fact that the terraces over the groove's left edge are closer to the cracks, *i.e.*, the source of Cu adatoms.

6.3.2 Mound formation on sub-nanometer scale: Atomistic insights through qualitative description

The snapshots of EC-STM images in Figure 6.2 reveal the dynamic nature of mound formation. Here, we discuss the underlying surface physics processes through the time perspective of kinetic roughening including examples of nucleation, coarsening, growth-induced coalescence, island reshaping, and kinetic roughening. Therefore, we follow an ideal time-frame of the mound formation through homoepitaxy, discuss several processes in parallel, and use surface science terminology.

1. Nucleation

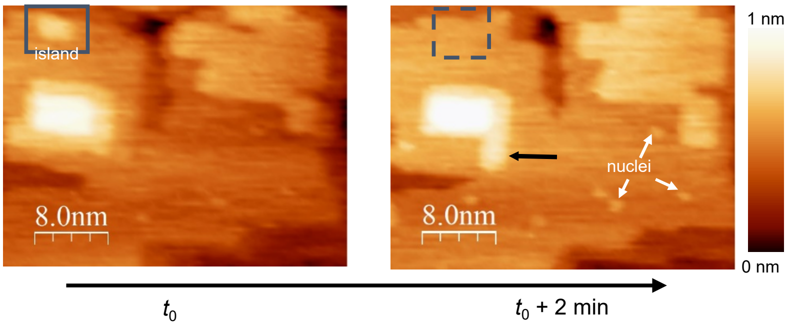

Figure 6.4 – **Nucleation of the mounds.** EC-STM images showing adatom nuclei. The square denotes the sudden disappearance of an island, implying Smoluchowski ripening.

The first step in mound formation is nucleation. Intense mass transport event limits us to follow the nucleation of the first two mound layers. We thus analyzed the nuclei in the third mound layer (Figure 6.4). Nuclei are situated at the center of the terrace and far from the nearest ascending and descending step-edges, implying adatom depletion around the island edges. Diameter of these nuclei is (1.2 ± 0.2) nm. The nuclei size is in agreement with the theoretical prediction of Cu/Cu(100) homoepitaxy from classical nucleation theory $(r \approx 1.5\,\mathrm{nm})$.[95,154,155]

2. Coarsening

An implication of Smoluchowski ripening is shown in Figure 6.4. We observed sudden disappearance of the small (100) island in the top-most mound layer, simultaneously with the lateral growth of the large adjacent (100) facet. Blurriness of the small facet, just before it disappears, might be related to its motion. Unusual dynamics of the large (100) facets was also observed in late growth phase when the mass transport was poorer (Figure

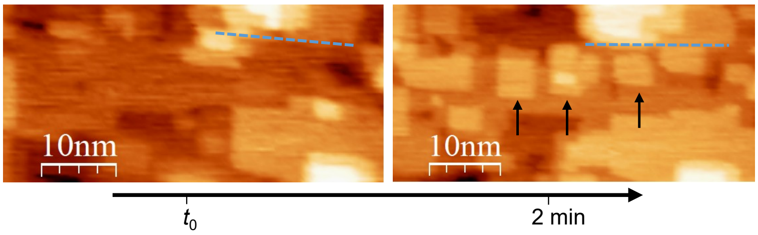

Figure 6.5 – **Smoluchowski ripening.** EC-STM images showing sudden appearance of (100) facets denoted with black arrows. Note that these two images were obtained within 2 minutes. The blue lines, denoting the edges of the same (100) facet, serve as visual guide for drift correction.

6.5). In particular, (100) facets with the edge lengths of ≈ 5 nm suddenly appear. Because such rapid nucleation and growth in the late stages seem unlikely, we conclude that these facets diffused as intact islands. Further evidence comes from the fast side-to-side collision of two facets, without any signs of growth-induced coalescence (Figure 6.7 b)).

3. Growth-induced coalescence, reshaping, and kinetic roughening

EC-STM images in Figure 6.6 show how the mounds form. As earlier, EC-STM images obtained at t_0 appear blurry due to significant mass transport from the crack. Despite this blurriness, we spot the rectangular (100) facets elongated along x-axis. Their apparent heights (1.7 Å) are consistent with the expected Cu step height (1.8 Å).[156] Consecutive images show facets with the apparent heights of 3.6 Å, implying rapid formation of bilayer mounds. Also, the rectangular shape of the bilayers is less discernible. The first mound layers rather resemble the terraces formed upon lateral merge of several rectangular facets. This process is called growth-induced coalescence and is visible in Figure 6.6 c) at 6th and 9th minutes. Taken together, simultaneous growth of the lower mound layers and the nucleation of the upper mound layers is a clear evidence of the kinetic roughening.

The mounds have straight-angled contours. The (100) facets in the top-most mound layers are of near-square shape. The ones in the lower layers have a checkerboard-like pattern of alternating (100) facets and regular pits, both having straight edges meeting at a 90° angle (Figure 6.6). The rapid reshaping to the square shape is also evident upon collision of two growing facets in the same mound layer. Moreover, it is worth noting that the shape of the first mound layer is rectangular. Similar deviations from a perfect square shape are also visible as checkerboard-like patterns (see Figure D.3 at $t_0 + 6$ min).

Another example illustrating mound formation is shown in Figure D.3. This set of EC-STM images was obtained in proximity of the surface area shown in Figure 6.6. The mass transport from the same crack is thus reflected in the similar mound formation kinetics, especially evident in simultaneous nucleation and growth of bilayers within the first three minutes. Mounds consist of between 4 and 11 surface layers. The number of mound layers strongly depends on the position with respect to the source of Cu adatoms (*i.e.*, the surface crack in Figure 6.2). The mounds close to the crack have many layers and are thus higher than the ones that are further away. Furthermore, the number of layers per mound and mound heights decrease over a micrometer scale as the distance from the source increases.

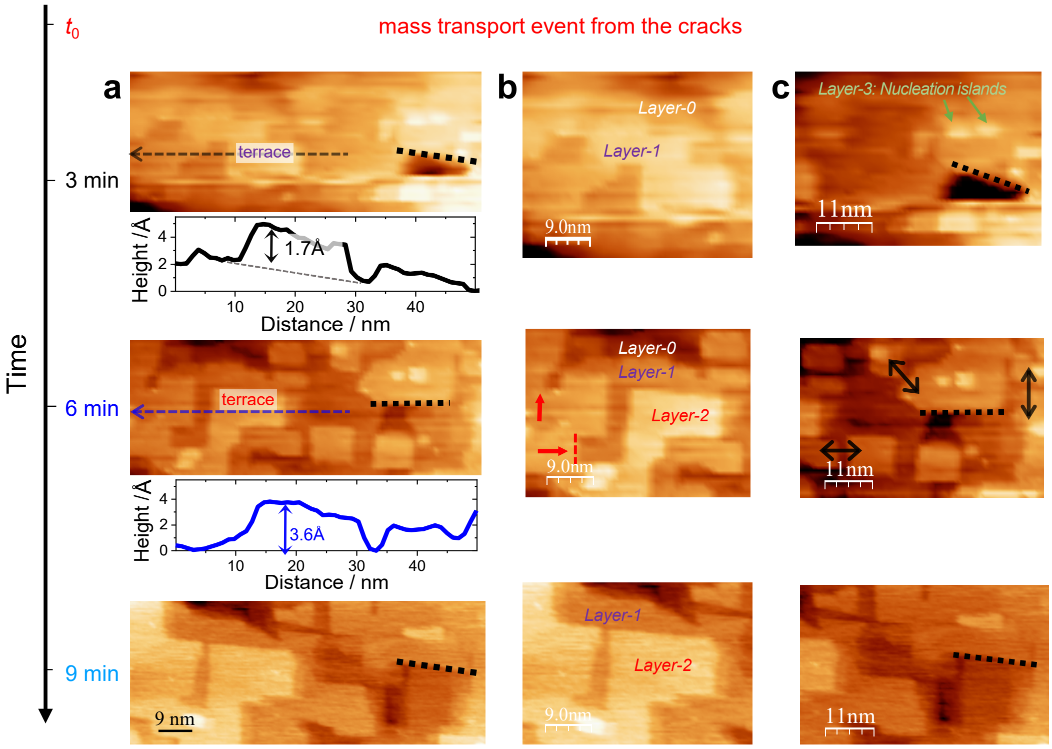
t_0
mass transport event from the cracks
a
b
c
3 min
terrace
Layer-0
Layer-1
Layer-3: Nucleation islands
9.0nm
11nm
Height /Å
1.7Å
0
2
4
10
20
30
40
Distance / nm
Time
6 min
terrace
Layer-0
Layer-1
Layer-2
9.0nm
11nm
Height /Å
3.6Å
0
2
4
10
20
30
40
Distance / nm
9 min
9 nm
Layer-1
Layer-2
9.0nm
11nm

Figure 6.6 – **Growth-induced coalescence and multilayer growth.** (a) Consecutive EC-STM images showing the mound formation through kinetic roughening and corresponding apparent height profiles. (b) and (c) Zoom-ins of EC-STM images in a). In b), lateral growth of the (100) facets in the layer-2 denoted with the red arrows. In c), growth-induced coalescence of the adjacent (100) facets in the layer-2 via side-to-side connection and corner-to-corner connection. The red arrow denote the same step edge: it serves as visual guide for drift correction.

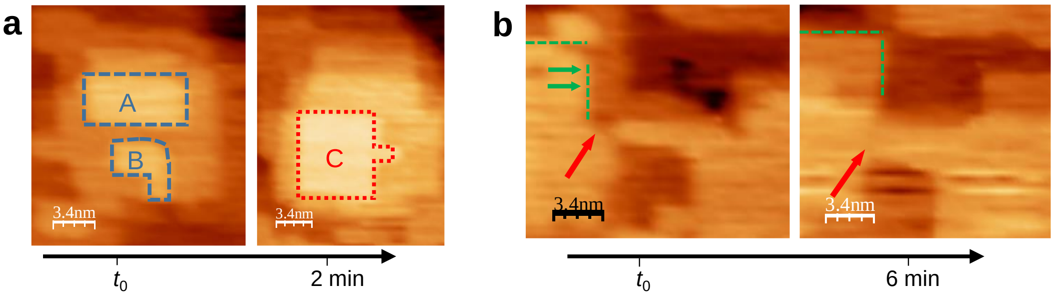
a
A
B
3.4nm
C
3.4nm
t_0
2 min
b
3.4nm
3.4nm
t_0
6 min

Figure 6.7 – **Coarsening mechanisms.** (a) Side-to-side collision of two islands followed by reshaping to near-square shape. (b) Corner-to-corner collision.

Growth-induced coalescence proceeds via two pathways: side-to-side collisions and corner-to-corner collisions (Figure 6.7). Side-to-side coalescence is followed by reshaping to a near-square shape (Figure 6.7 a)). Both collision and reshaping are rapid, occurring in only two minutes. Analysis of the island areas reveals that the sum of the areas of two islands before collision is equal to the area of the fused island,

$$A_{\mathrm{total},t_0} = A(\text{island-A}) + A(\text{island-B}) = 35\mathrm{nm}^2 + 15.2\mathrm{nm}^2 \approx 50\mathrm{nm}^2,$$

while

$$A_{\mathrm{total},t_0+2\mathrm{min}} = A(\text{island-C}) \approx 47\mathrm{nm}^2.$$

These two observations suggest that the islands merge upon rapid collision; it seems that no lateral growth precedes the merge. Alternatively, two (100) facets approaching each other at 45° angle (corner-to-corner collision) form a meniscus-like neck that grows over time into a rectangular connection (Figure 6.7 b)). This implies the enhanced adatom transport along the edges, *i.e.* perimeter diffusion. Both corner-to-corner and side-to-side collision mediated by perimeter diffusion mass transport are characteristic for metal (100) homoepitaxy.[157]

6.3.3 Mound formation during CO_2RR

The *in situ* EC-STM study presented in previous Section shows the surface dynamics during mound formation. The mounds form close to the surface cracks. The surface further away from the cracks remains unchanged, *i.e.* there is no surface restructuring of any kind under the same conditions. This implies that: (i) the mound formation is a local phenomenon; (ii) as the mounds are forming, the ECSA is changing; (iii) mound formation corresponds to simultaneous formation of (100) facets and bunching of [110] steps.

Changes in surface area during mound formation

Any *in situ* structural evolution necessarily induces a change of ECSA. In this context, mound formation leads to an increase in ECSA. To evaluate this change, we estimated the ECSA from EC-STM images shown in Figure 6.2. Relative ECSA changes were calculated with respect to the geometrical surface area (74×34 nm^2) in the EC-STM image obtained at $t_0 + 3$min.

ECSA increases $> 2\%$ with respect the initial surface area at $t_0 + 3$min. The maximum value coincides with the formation of the top-most mound layer and thus, partially reflects bunching of the [110] step edges. Further mass transport, now poorer than initially, contributes to the lateral growth of the mound layers. Therefore, growth-induced coalescence leads to a continuous enlargement of (100) facets and to a consequent increase of the total length of the [110] step-edges. These atomistic processes are reflected in a decrease of ECSA. The final value at $t_0 + 14$ min is, however, higher than the initial (see Figure 6.8). This example shows that local surface dynamics phenomena significantly change the local ECSA, even if the overall surface is largely unchanged.

Strain across mound layers

Mounds undergo strain relaxation through an oscillating in-plane lattice spacing of the top-most layers (Figure 6.9). The oscillatory nature of interlayer spacing suggests alternate contraction and expansion for consecutive layers.[128] Relaxation decays down to the sixth

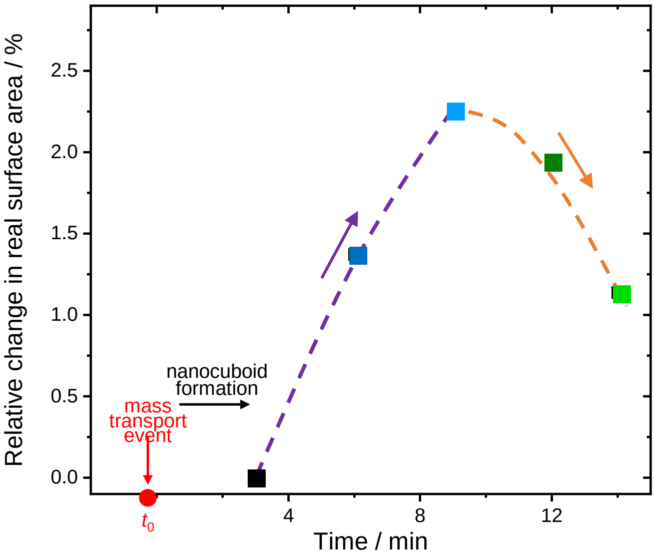

Figure 6.8 – **Surface area changes during mound formation.** Relative change of the surface area estimated from EC-STM images obtained during mound formation and shown in Figure 6.2, panel *ii*. The dashed lines serve as visual guide for qualitative trend.

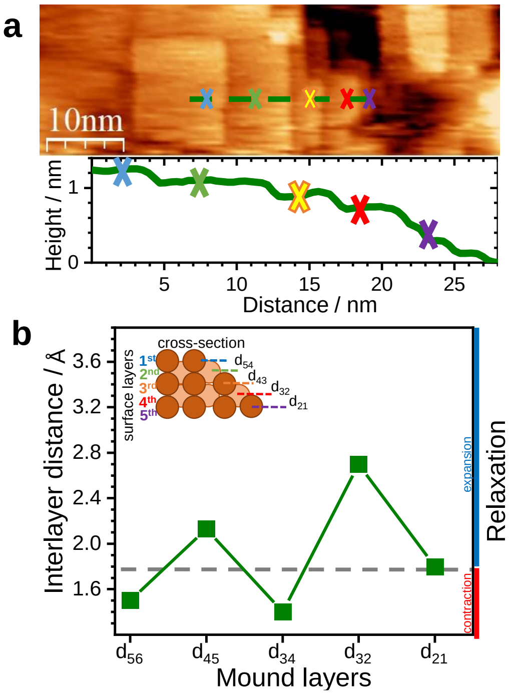

Figure 6.9 – **Strain across the mounds.** (a) EC-STM image of a Cu mound. (b) Interlayer distances across the mound correlated with the oscillatory strain relaxation toward bulk. Inset: cross-sectional view through the mound showing the interlayer distances.

mound layer, where the interlayer spacing equals the bulk spacing of 1.8 Å.

CO_2RR product analysis during the mound formation

To correlate the mound formation with CO_2RR, we performed gas product analysis under the conditions of EC-STM experiment in Figure 6.2. CO_2RR was conducted in 0.1 M CO_2 saturated $KHCO_3$ at $-0.03\,\mathrm{V}$ *vs* RHE for 1 hour after which the gas aliquots were qualitatively analyzed by gas chromatography. A set of seven CO_2RR electrolyses was conducted on the same G-Cu sample. These studies differ from the regular potential-dependent CO_2RR product analysis, where the poor understanding of the surface dynamics greatly challenges unambiguous correlation between the surface morphology and CO_2RR. The fact that we fully understand the surface physics processes at $-0.03\,\mathrm{V}$ *vs* RHE allows us to study the effect of mound formation on CO_2RR.

Qualitative analysis of the gas products during mound formation shows that CH_4 and H_2 were produced. As further discussed in Section D, CO was not detected because its peak overlaps with the peak of the water vapor that was unintentionally injected together with the gas aliquots. However, we speculate that CO also forms during mound formation. This follows from the fact that CO is an intermediate in the reaction pathway toward CH_4.[158] Furthermore, qualitative analysis of the gas aliquots is not fully reliable because the aliquots were not necessarily representative samples of the gas mixture in the cathodic compartment after CO_2RR. The fact that no C_2H_4 was detected does not exclude the possibility that it was produced during CO_2RR on the mounds. These results imply CO_2RR at remarkably low potential, especially interesting for CH_4 that usually starts forming on Cu(100) single crystals at $-0.65\,\mathrm{V}$ *vs* RHE.[98]

6.4 Discussion and conclusion

EC-STM provides insights into the nanocuboid formation mechanism. Mass transport from the surface cracks results in the rapid formation of Cu mounds. Sub-nanometer details of the mound formation greatly resemble the surface physics processes in Cu/Cu(100) kinetic roughening.[159]

Atomistic description of homoepitaxial growth describes well the mound formation. Metallic Cu atoms diffuse from the crack across the surface until they find the adsorption site of minimal energy, in particular the bridge site. Lattice symmetry of the underlying Cu(100) crystalline grain acts as a template driving the formation of the near-square (100) facets.[160] Rapid growth of the first mound layers increases the probability that the incoming adatoms diffuse to their tops. Moreover, they cannot diffuse over the descending step-edge due to the Ehrlich-Schwoebel barrier.[146,147] In this way, inhibited downward transport results in the nucleation of the upper mound layers.

This mechanism further explains the differences in the mound heights. The mounds that formed closer to the cracks have more layers and are higher, whereas those further away from the cracks exhibit less layers and lower heights. This implies that diffusion determines the perimeter of the surface area in which the mounds form. EC-STM studies in Chapter 3 suggest that such areas extend over several micrometers from the cracks. Hence, the observed inhomogeneous macroscopic spatial scale distribution of the mounds on G-Cu imply that only few cracks form across the sample surface.

Cu/Cu(100) homoepitaxy also sheds light on the subtle morphological differences of the mounds. Checkerboard-like patterns are characteristic for mounds with more than 10 layers.[161] Furthermore, UHV studies of the Cu/Cu(100) homoepitaxy suggest that the elongated rectangles form when the adatoms arrive at an oblique angle.[162] This is in line with the our observations that the mass transport events start from the surface cracks. Further overview of Cu/Cu(100) homoepitaxy studies in UHV suggests that the mound morphologies depend on the Ehrlich-Schwoebel barrier, the substrate temperature,[162,163] and the deposition rate.[164] Translation of these parameters to the electrochemical environments is not straightforward, especially because of the influence of the electrochemical potential[165] and water[166] on the Ehrlich-Schwoebel barrier remains obscure.[167]

We highlight the main similarities between kinetic roughening under CO_2RR conditions and Cu/Cu(100) homoepitaxy in UHV. First, the nuclei size is in excellent agreement with the theoretical prediction from classical nucleation theory.[154] Second, the observation of Smoluchowski ripening agrees with Cu/Cu(100) homoepitaxy.[153] However, it is know from UHV studies that temperature induces a transition from Smoluchowski[153] to Ostwald ripening.[93] In a similar way, the ripening mechanism of mound formation under CO_2RR conditions might be affected by the potential, electrolyte composition, and adsorbates. Third, the lateral growth, coalescence, and kinetic roughening phases of the mound formation greatly resemble Cu/Cu(100) homoepitaxy. Fourth, the mounds are highly strained with strain oscillations decaying towards the bulk. Similar strain oscillations with a period of one atomic layer have been reported for small homoepitaxial islands prepared upon deposition in UHV[168] and upon electrodeposition,[169] where strain arises from the differences in the lattice constants between the small islands and the bulk layer (a_0(small island)$<$ a_0(bulk)).[154]

Kinetics of the mound evolution might depend on the potential and is very likely sensitive to the presence of adsorbates. For example, this process might be influenced by enhanced mobility of Cu–CO motifs.[95] It is important to note that it is difficult to decouple the effects of the sole potential from those of the adsorbates. Their interconnection might mislead to a conclusion that the reaction intermediates induce adsorbate-driven surface reconstructions.[46] While this might be the case for other surface dynamics processes, we highlight that the mound formation reported here can only be fully explained by Cu/Cu homoepitaxy.

If considering the Cu/Cu homoepitaxy on Cu(111) crystalline grains, the (111) facets are of hexagonal and/or triangular shapes.[170] This scenario is rarely observed in EC-STM studies of G-Cu because polycrystalline Cu underneath graphene is mostly composed of (100) grains (Figure 2.13). Still, we speculate that the surface cracking followed by mound formation happen both on (100) and (111) surfaces. This hypothesis is further supported by the discussion in the following Section, where we present the correlation between the surface cracking and reduction of Cu_xO. Moreover, Figure D.1 shows an EC-STM study where (111) facets were stable over at least 1 hour. This result allows us to conclude that the mound formation is not equivalent to the surface reconstruction observed by Soriaga *et al.*, where the polycrystalline surfaces reconstruct first to (111) and then, to (100) over 1 hour.[47]

The mound formation indirectly implies locally enhanced CO_2RR activity. This might arise as a consequence of the relationship between the structure and CO_2RR product selectivity, including both the formation of C_{2+} products on (100) facets and the formation of alcohols on [110] steps.[34,171] In addition to these structural features, misfit strain across the multilayers might also be beneficial for C–C coupling.[172] Further indications on CO_2RR activity of the mounds come from the product analysis. It is important to note that the product analysis was conducted mimicking the conditions of EC-STM studies, allowing us simultaneously to understand the mound formation and to exclude the possibility of alternative surface processes. Qualitative analysis reveals H_2 and CH_4 formation on the mounds. H_2 always evolves at low CO_2RR overpotentials[173]: its evolution on G-Cu is likely related to the significant HER activity of large Cu(100) crystalline grains.[174,175] CH_4 production at $-0.03\,\mathrm{V}$ *vs* RHE is rather surprising considering the potential-dependent product selectivity trends,[89,98,173] which suggest that CH_4 on Cu(100) single crystals evolves at potentials more negative than $-0.65\,\mathrm{V}$ *vs* RHE.[98] Additionally, CH_4 evolution is usually preceded by C_2H_4 evolution at higher potentials. CH_4 production at $-0.03\,\mathrm{V}$ *vs* RHE is thus the lowest overpotential ever reported. We speculate that the strain across the mound and [110] step bunches are a beneficial combination for CO_2RR. If so, CH_4 might be one of many CO_2RR products produced on the mounds. It might even be that different geometrical arrangement of the atoms along the mound terraces, steps, and corners are active sites for various CO_2RR products, which would ultimately explain why Cu is the only catalysts allowing conversion to more than 16 intermediates. This hypothesis is yet to be confirmed; however, indirect evidences come from the studies of single-crystalline Cu surfaces that do not produce CH_4 and remain unchanged after CO_2RR only if cleaned in UHV environment and transferred under protective atmosphere.[176,177]

Correlation between Cu_xO reduction and mound formation

Cracks as the source of Cu species are of central interest for deeper understanding of the mass transport events. Figure 6.2 shows the key moment preceding the mound formation: the mass transport event from the surface cracks. Here, we observed the cracks on the surface, but were unable to image the moment of their formation. Their evolution during mound formation is also too drastic to be followed by EC-STM. Therefore, we speculate on their origin based on EC-STM images showing three cracks under the angle of $\approx 60°$ on a $250 \times 250\mathrm{nm}^2$ surface area.

The first hypothesis is that the surface cracks are grain boundaries on Cu surface. However, (100) crystalline grains of Cu surfaces underneath graphene extend over 20 µm (Figure 2.13) and, therefore, finding triple grain boundaries on $250 \times 250\mathrm{nm}^2$ surface areas seems rather unlikely.

The second possibility is that the cracks form upon reduction of Cu oxide. Orientation of the surface cracks resembles both the triple grain boundary junction of graphene[178] and the ridge nodes of graphene wrinkles. Both the graphene grain boundaries and the wrinkles are the local imperfections in graphene under which Cu oxidizes.[179,180] Hence, the Cu surface underneath these regions undergoes fast oxidation. Reduction of Cu_2O islands formed in this region would then induce surface cracking. This premise is further supported by the fact that the nanocuboids inhomogeneously form over G-Cu surface in all electrolytes, which also explains the low success rate of EC-STM observations.

Further evidences that the mound formation is due to $Cu_2O \rightarrow Cu$ reduction follow from environmental TEM studies.[181,182] Reduction of Cu_2O islands, grown on Cu(100) surfaces, leads to simultaneous formation of cracks at the position of the Cu_2O islands and homoepitaxial growth of the surface features on the adjacent terraces.[181,182] Mounds also form on Cu(100) single crystals upon reduction of Cu_2O layer.[156] While the great morphological similarities further imply that the mounds form upon reduction of Cu_2O, the oxide thickness and chemical composition might change the oxide reduction mechanism.[183]

Similar surface cracks form upon reduction of Cu oxide layers on oxide derived Cu catalysts.[184,185] These findings, independently reported for Cu_2O NCs prepared by colloidal chemistry[184] and mixed oxide films prepared through electrochemical and thermal oxidation of polycrystalline Cu surface,[185] imply the crack opening upon Cu_xO reduction of the oxide layers regardless of how the Cu_xO layer was formed. Furthermore, temperature-dependent desorption studies imply that the active sites are the strained and defective structures formed close to the cracks[43] that relax upon annealing in vacuum.[43] Importantly, the latest literature highlights the hypothesis that these features are the active sites, while simultaneously ruling out that OD Cu catalysts' CO_2RR performance is due to the stability of Cu^+ species,[67] increase in ECSA,[186] and the cracks.[175]

Unambiguous conclusion that the mounds formed upon Cu_xO reduction are the active sites for CO_2RR has been hindered by numerous experimental challenges. The mounds rapidly oxidize under OCP conditions, *i.e.*, within a few minutes after stopping CO_2RR (Chapter 4). Oxidized mounds contribute to the rough appearance of the (OD) Cu catalysts in post mortem microscopy studies and increased ECSA, but are undetectable by *ex situ* XRD and electron backscattered diffraction. Furthermore, poor understanding of *in situ* surface dynamics has prevented the identification of active sites for CO_2RR. Only very recent literature exploiting *in situ* surface-sensitive techniques highlights the enrichment of polycrystalline Cu with Cu(100)-like facets.[87,88,100] Interestingly, Velasco-Velez *et al.* suggest that the structural evolution might be correlated with the reduction of Cu_xO. Additional challenges come from the fact that *in situ* surface science studies employed pre-cleaned polycrystalline and single-crystalline surfaces. Here, we overcame this challenge by employing a G-Cu model system. Direct observation of the mound formation close to the surface crack, together with the extensive knowledge on the local Cu oxidation through graphene defects, allowed us to correlate these two processes.

Finally, the fact that Cu catalysts quickly oxidize under OCP potential[87,156] suggests that Cu_2O is present on Cu catalysts before starting CO_2RR experiments.[118] Above, we have shown that surface cracking followed by mound formation is the main structural transformation related to the reduction of (native) Cu oxide facets and have hypothesized that this transformation corresponds to the *in situ* formation of CO_2RR active sites. Such interpretation supports the premise that the overall similarities in CO_2RR catalytic performances for Cu-based catalysts are due to the undercoordinated sites formed during preparation or testing of Cu catalysts.[30]

Part V

The end

7 Final remarks

Conclusion

Electrochemical reduction of carbon dioxide is a central chemical reaction in artificial photosynthesis devices. As such, it also stands out as the only synthetic route to renewable carbon-based fuels and chemicals that could rely on the direct capture of CO_2 from air. Among the catalysts tested so far, copper is the only metal able to convert CO_2 beyond C_{2+} products. A large body of literature on Cu-catalyzed CO_2RR, with more than 2500 papers published since 1986, seeks for the CO_2RR active sites. Here, I present *in situ* surface science studies that allowed us to identify these active sites.

This thesis explores the *in situ* evolution of Cu-based CO_2RR catalysts. I presented the first *in situ* EC-STM studies that revealed the formation of Cu nanocuboids as the main structural evolution under CO_2RR conditions. A synergy of SEM, AFM, and STM provide us further insights into this structural evolution over micrometer scales. Furthermore, I reported *in situ* Raman spectroscopy studies confirming that metallic Cu is the active phase for CO_2RR. Cu catalysts, rapidly oxidized upon exposure to air, necessarily undergo reduction of as-formed Cu oxide when starting CO_2RR. In-depth studies of both structural and oxidation state evolution, described through Chapters 3–6, revealed a unique correlation between these two processes. By disclosing the surface physics processes behind the nanocuboid formation, I concluded that the nanocuboids are the metallic Cu mounds formed upon reduction of Cu oxide. This pioneering work reveals the structural and chemical composition of the CO_2RR active sites, while disclosing the surface physics processes behind their formation.

Chapter 3 introduced the polycrystalline Cu surface covered by a graphene monolayer as the model system for *in situ* surface science studies Cu-based CO_2RR catalysts. By benchmarking its CO_2RR catalytic performance against bare polycrystalline Cu surface, we showed that Cu catalysts have similar intrinsic activities. Our *in situ* EC-STM studies revealed that nanometer-sized cuboids form on Cu surface during CO_2RR either as square (100) facets or as (100) facet multilayers. Further *in situ* EC-STM studies disclosed that the formation of the nanocuboids is a unique structural transformation occurring in aqueous electrolytes over a wide range of pHs. *In situ* Raman spectroscopy revealed that native Cu oxide reduces to metallic Cu when starting CO_2RR.

In situ electrochemical reduction of the native oxides necessarily happens in the first few seconds of CO_2RR. In Chapter 4, we addressed the question of Cu oxidation. I presented nanoscale studies of the ambient oxidation of Cu underneath graphene. By revealing the similarities in the atomistic details between ambient oxidation of our model system and high-pressure oxidation of bare Cu surfaces, we identified a unique surface chemistry process on Cu catalysts. Spatial inhomogeneity in oxidation of Cu underneath graphene, as one of the main findings of this Chapter, allowed us to understand further studies addressing the mechanism behind nanocuboid formation.

Chapter 5 explored the mechanism of the nanocuboid formation. We hypothesized that the nanocuboids grow on the surface upon dissolution and/or electrodeposition. A combination of SEM, AFM, and EC-STM with *in situ* Raman spectroscopy and quasi *in situ* XPS revealed the differences in their morphologies and chemical composition. Nanocuboid formation during CO_2RR was related to the potential-driven re-organization of the metallic Cu atoms. In contrast, Cu_2O nanocubes preparation through electrochemical cycling suggested thermodynamic crystal growth through electrodissolution/electrodeposition cycles. Further investigating the role of halide additives on Cu_2O nanocubes synthesis, we showed that the chlorides enhance electrodissolution in the anodic scans, which results in electrodeposition of higher Cu amounts in the cathodic scan.

Chapter 6 presented an *in situ* EC-STM study showing the atomistic details of the nanocuboid formation. By comparing the nanocuboid formation with the mound formation through Cu/Cu homoepitaxy, we tracked the underlying surface physics processes. These insights imply that the formation of Cu nanocuboids happens locally around the surface cracks that form during the reduction of Cu oxides. By correlating these two evolutions, it is now clear that as-formed nanocuboids necessarily form on all catalysts upon pre-cleaning or in the first potential sweep to CO_2RR potentials. These results bring us to conclude that the active sites for CO_2RR are the metallic Cu mounds formed upon Cu oxide reduction.

Outlook

Artificial photosynthesis holds great promise to be one of the pillars of the carbon-neutral society. Recent progress in artificial leaf devices pinpoints the challenges to be overcome, including optimization of device components, operation conditions, as well as reactor architectures, stability, and scalability. Further addressing CO_2RR research in general, impressive progress has been attained in recent years. The field itself has branched into fundamental theoretical and experimental research, catalyst synthesis, and reactor testing. Here, I provide a short perspective for *in situ* surface science as the gearing point between theoretical modeling and catalyst's optimization.

First, the complexity of practical catalysts implies inhomogeneous catalytic activity across microscopic scales. This issue, also demonstrated in this thesis, urges the studies addressing the correlation among surface structure, local chemical composition, and activity. Here, a combination of local CO_2RR product analysis with *in situ* microscopy and/or spectroscopy would fulfill a long-standing dream for the *operando* community. For example, *in situ* optical second-harmonic imaging allows mapping of electrochemical heterogeneity over micrometer scales.[187] Moreover, electrochemical tip-enhanced Raman spectroscopy allows simultaneous imaging and spectroscopy at the nanoscale.[188] Further advances could rely on combing electrochemical tip-enhanced Raman spectroscopy with noise electrochemical scanning tunneling microscopy, now allowing quantitative mapping of the local catalytic activities.[189,190]

Second, *in situ* microscopies have provided relevant insights into catalysts structural transformations. Recent developments in *in situ* TEM and SEM open a new era for *in situ* electron microscopies; however, electron beam-induced restructuration remains as a considerable issue for metal catalysts. Simultaneously, scanning probe microscopies stand out as non-invasive imaging techniques with atomic resolution. I believe that this field will be of great importance in the years to come. Importantly, it requires the development of gas-tight, electrolyte-flow cells,[191] as well as micrometer-sized reference electrodes[192] and pH meters.[193] I envision that further advances will rely as well on an artificial intelligence-driven approach and advanced image analysis, overcoming the current limitations of case by case image interpretation.[194]

Third, *in situ* spectroscopy provided invaluable insights into the chemical composition of the electrocatalysts. Another research line studies the reaction intermediates, *e.g*, in *in situ* Raman spectroscopy currently limited by the insufficient knowledge on the adsorbates band assignments. This issue could be addressed through a synergy of modeling, *in situ* shell-isolated nanoparticle-enhanced Raman spectroscopy studies on single crystals,[195] and *in situ* surface-enhanced Raman spectroscopy studies on practical catalysts.

Fourth, this thesis calls for three-dimensional Monte Carlo modeling. To this end, I highlight recent literature reporting a coarse-grained kinetic Monte Carlo method for dendritic growth.[196] Further development would provide us with a detailed understanding of the growth during metal deposition, dendritic growth in metal batteries and during *in situ* structural transformation of the metallic electrocatalysts.[197]

In the broader context of *in situ* surface science, Chapter 6 demonstrates that *in situ* evolution is necessarily related to a continuous change of ECSA. This challenges the current concepts of ECSA evaluation, currently relying on spatially averaged ECSA measurements either before the reaction or after the reaction. While ECSA correction is of unquestionable importance, the first step for benchmarking ECSA values would be to evaluate them on single crystal surfaces prepared in UHV, by using electrochemical cells mounted on the vacuum chamber.[198]

This short overview presents only a few perspectives that came along with this thesis. Development and implementation of advances in *in situ* characterization techniques will provide new insights into the electrocatalysis by addressing fundamental questions and elucidating reaction mechanisms, always in synergy with theoretical modeling and testing of practical catalysts.

A Stability of graphene during CO_2RR

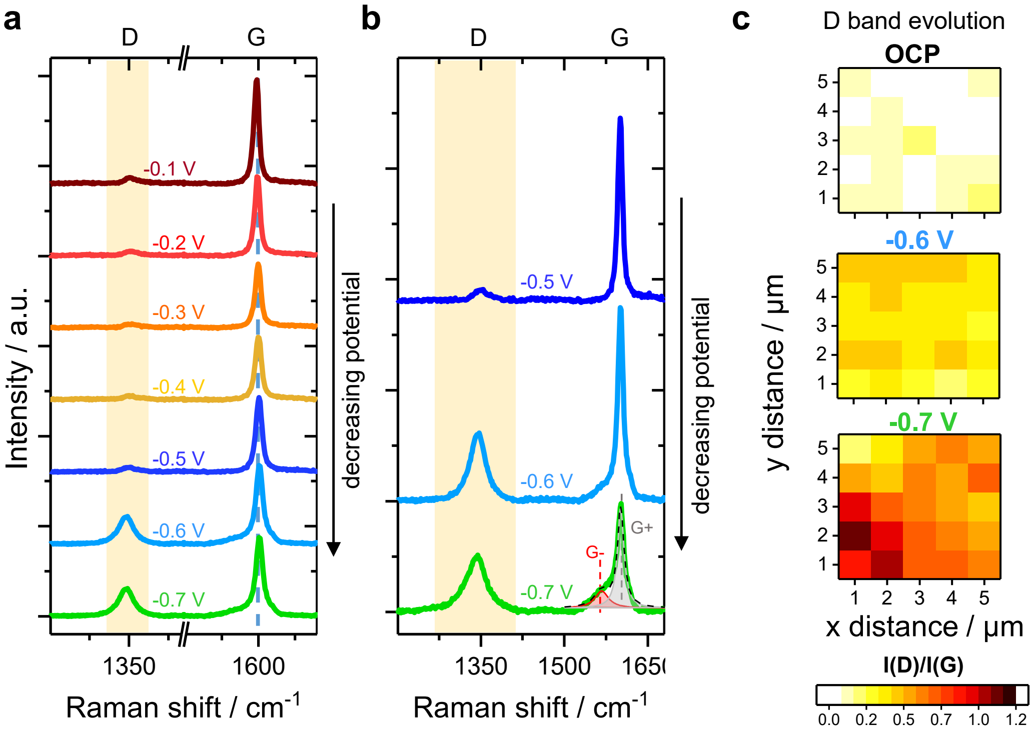

Figure A.1 – *In situ* Raman spectroscopy of graphene during CO_2RR. (a) Potential-dependent *in situ* Raman spectra of graphene for CO_2RR on G-Cu in 0.1 M CO_2 saturated $KHCO_3$. Appearance of the defect-induced D band at −0.6 V *vs* RHE suggest that graphene breaks within a few minutes of polarization at this potential. (b) Spectra of from a) showing the evolution of the D and the G bands together with the deconvolution of the G band for spectra obtained at −0.7 V *vs* RHE. The spectra shown here are average spectra calculated based on the Raman map collected over 5×5 µm^2 surface area. (c) I(D)/I(G) ratio maps showing the D band evolution over 5×5 µm^2 surface area. All spectra were collected between t=1 and 10 minute of the polarization at the respective potential.

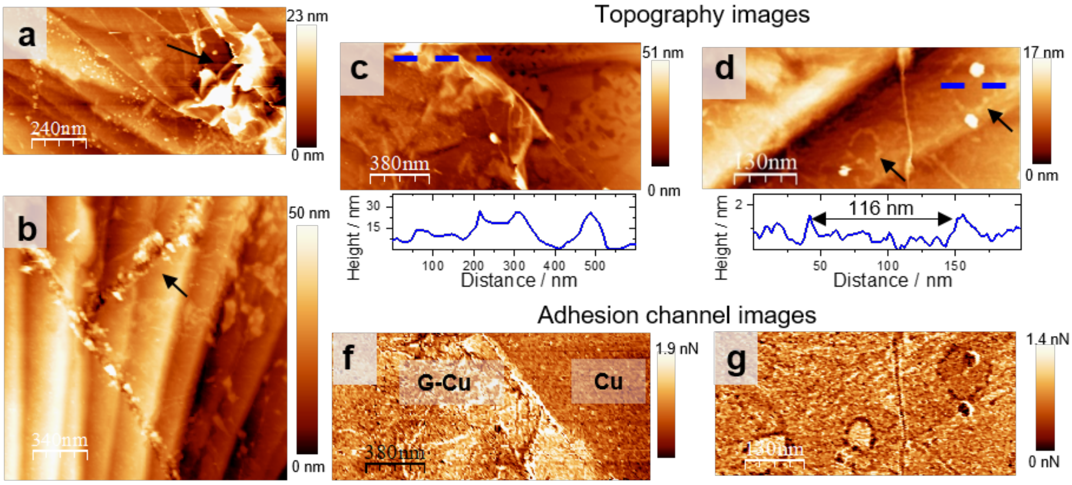
Topography images
a
240nm
23 nm
0 nm
b
340nm
50 nm
0 nm
c
380nm
51 nm
0 nm
Height / nm
30
15
100 200 300 400 500
Distance / nm
d
130nm
17 nm
0 nm
Height / nm
2
116 nm
50 100 150
Distance / nm
Adhesion channel images
f
G-Cu
Cu
380nm
1.9 nN
g
130nm
1.4 nN
0 nN

Figure A.2 – *Ex situ* AFM images showing defects of graphene after CO$_2$RR at −1 V *vs* RHE for 4 h. AFM height images showing (a) crumbled graphene, (b) line defects, (c) folded graphene, and (d) holes in graphene created upon bubble release together with corresponding adhesion channel images.

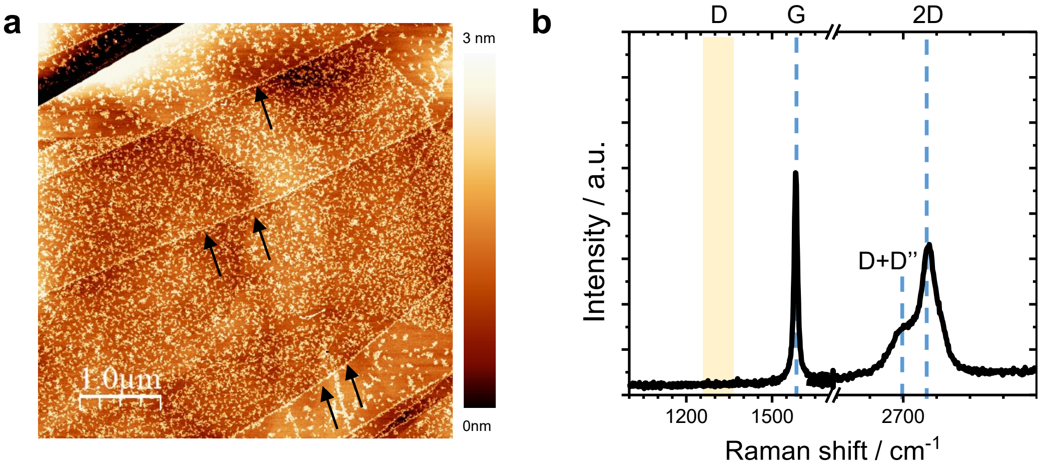

Figure A.3 – Overview of structural damage of graphene after CO$_2$RR on the example of the HOPG as the model system. (a) *Ex situ* AFM images showing HOPG surface after CO$_2$RR at −1 V *vs* RHE for 10 min. Arrows denote the step edges. (b) Raman spectrum of HOPG after polarization at −1 V *vs* RHE. This spectrum represents the average spectrum of the Raman map. The absence of the defect-induced D band (1350 cm^{-1}) implies that no defects were created upon polarization of HOPG.

The stability of graphene at high CO$_2$RR overpotentials was tested by *in situ* Raman spectroscopy and AFM. *In situ* Raman spectroscopy reveals that graphene starts breaking a few minutes after polarization at −0.6 V *vs* RHE. Post mortem AFM characterization of G-Cu after CO$_2$RR (constant-potential polarization at −1 V *vs* RHE for 1 hour) reveal graphene damage. Note that this CO$_2$RR condition is the condition at which the CO$_2$RR product analysis was conducted in Figure 3.2. Interestingly, defected graphene stays intact to the Cu surface under harsh CO$_2$RR conditions, even after 4 hour of CO$_2$RR.

The graphene breakage during CO_2RR is due to the gas bubble release from Cu. To test this hypothesis, we used highly oriented pyrolytic graphite as the model system for graphene supported by electrochemically-inactive substrate (Figure A.3). HOPG is in general pure and ordered form of synthetic graphite; as such, it represents the bulk counterpart of graphene. The top-most graphene layer is thus supported by the multilayer graphene stack. AFM image shows no evidence on the delamination after 10 minute CO_2RR at -1 V *vs* RHE. Delamination usually starts at step edges; however, they appear undisturbed. Additionally, the integrity is also confirmed by the absence of the defect-induced D band in the Raman spectrum obtained after polarization. This suggests that graphene is mechanically robust: it does not break upon surface polarization. We thus suggest that graphene breaks due to the gas bubble release from Cu.

B Supplementary Information: Chapter 3

Additional EC-STM images

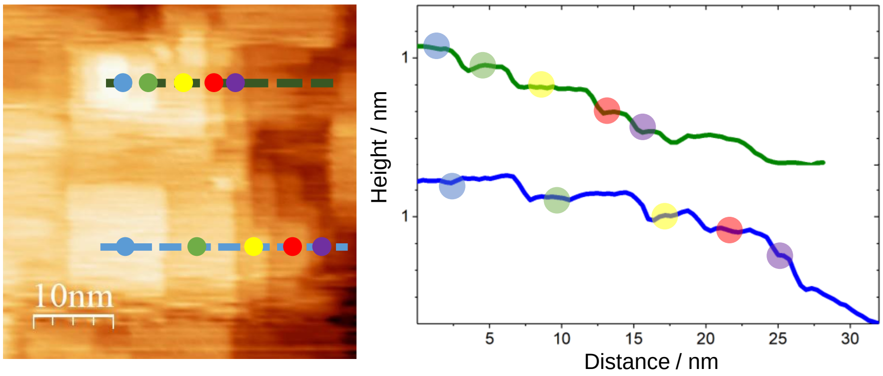

Figure B.1 – EC-STM images showing the multilayer structure of a nanocuboid. The image was obtained upon polarization of G-Cu in 0.1 M CO_2 saturated $KHCO_3$ at $-1\,V$ *vs* Pt pseudo-RE.

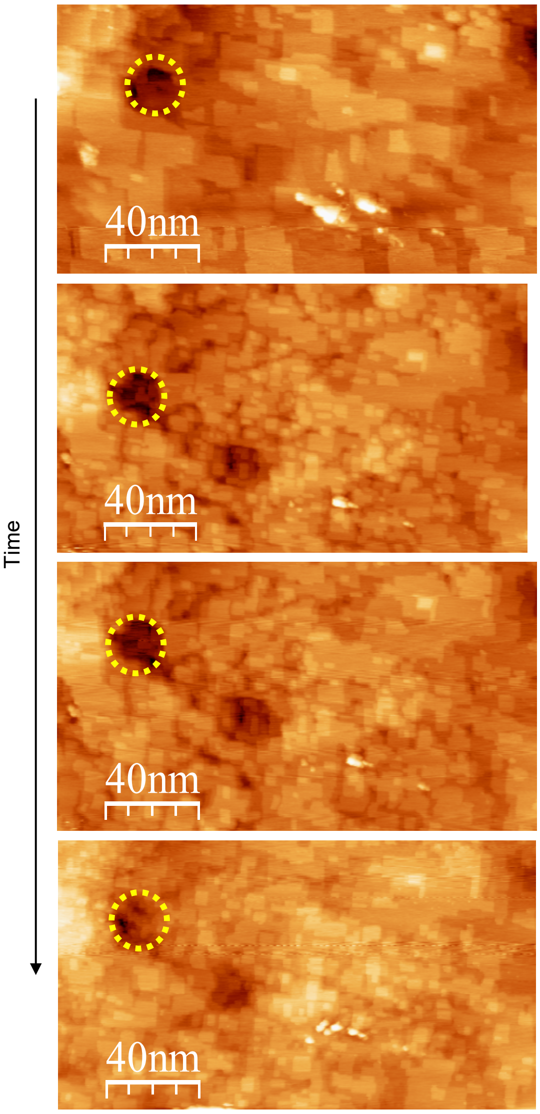

Figure B.2 – EC-STM images showing evolution of Cu nanocuboids over time. The same surface area with the apparent size of the nanocuboids reducing over time at the same potential. Theimages were obtained upon polarization of G-Cu in 0.1 M CO_2 saturated $KHCO_3$ at $-1\,V$ *vs* Pt pseudo-RE.

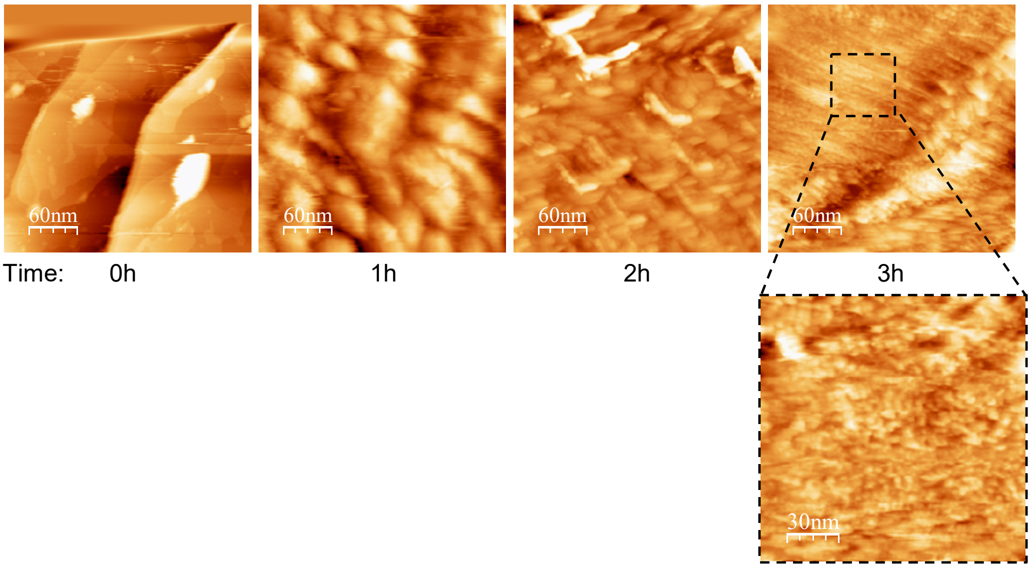
60nm
60nm
60nm
60nm
Time: 0h
1h
2h
3h
30nm

Figure B.3 – EC-STM images showing different stages of the surface nanostructuring in 0.1 M N_2 saturated K_2CO_3. To study the effect of the potential on the nanocuboid formation, the potential was kept at $-1.8\,V$ *vs* Pt pseudo-RE.

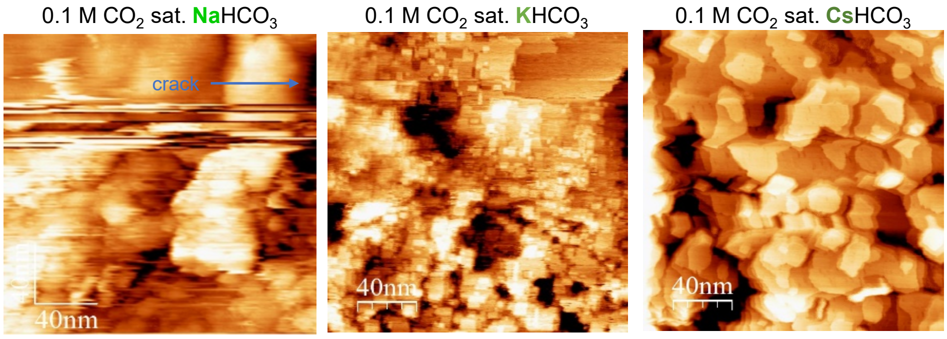
0.1 M CO₂ sat. NaHCO₃
0.1 M CO₂ sat. KHCO₃
0.1 M CO₂ sat. CsHCO₃
crack
40nm
40nm
40nm

Figure B.4 – EC-STM images showing the nanostructuring of Cu surfaces in 0.1 M CO_2 saturated Na^+, K^+, and Cs^+-containing bicarbonate electrolytes. While multilayer mounds can be found in all electrolytes studied, the time needed to observe them at $-1\,V$ *vs* Pt pseudo-RE seems to be faster in Na (1 h) than in K (4 h) than in Cs (8 h). Unfortunately, we could not collect enough data to do a systematic kinetic study on this effect.

Density Functional Theory model

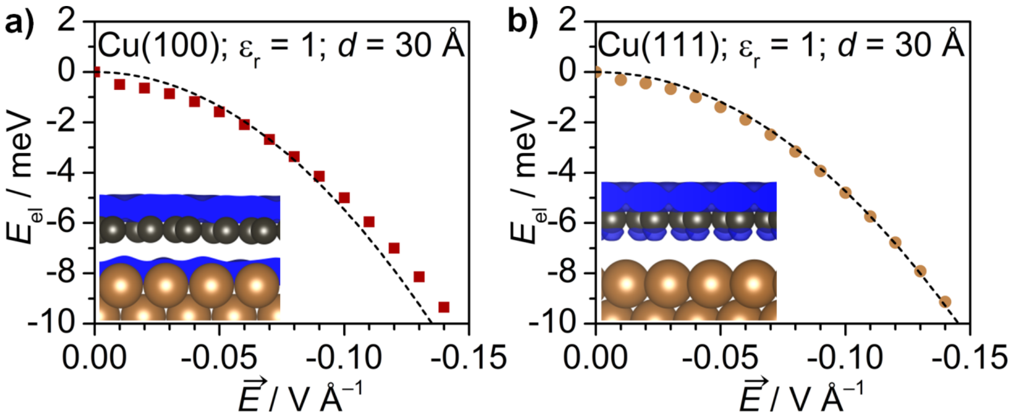

Figure B.5 – Electrostatic energy stored in the slabs for (a) Cu)(100) (dark brown squares) and (b) Cu(111) (light brown circles) for increasing applied electric field. Surface polarization determines higher electronic density shared among the Cu atoms. Therefore, the overall energy of the system decreases. The analytic model in dashed lines agrees with DFT data. Cu(100) has higher polarizability than Cu(111) due to its lower surface coordination number. Charge polarization is thus more significant for Cu(100) facets. Computational details were reported in reference 28.

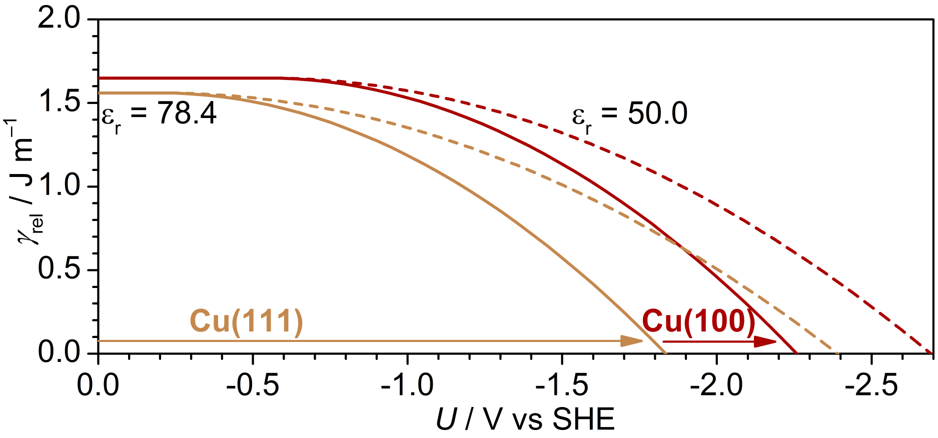

Figure B.6 – Modeled surface energies for Cu(100) (dark brown) and Cu(111) (light brown) facets assuming a dielectric permittivity of the solvent of 78.4 (and 50 in dashed lines) and an Outer Helmholtz Layer thickness equivalent to the distance between Cu and graphene (equation S4 in reference 28).

Supplementary discussion: Absence of surface adsorbates on formation of nanocuboids

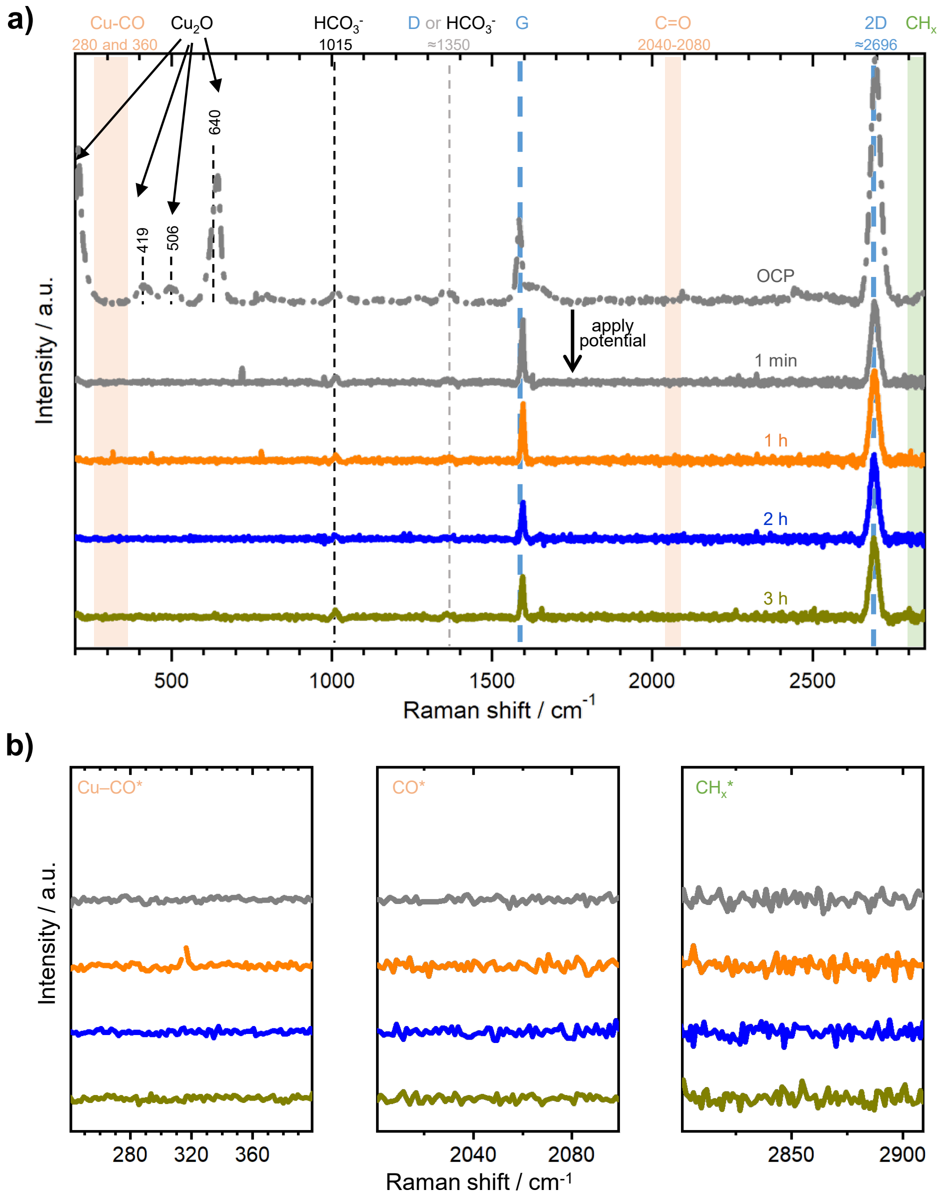

Figure B.7 – Raman spectra obtained on G-Cu at open circuit potential and during nanocuboid formation at $-0.03\,\mathrm{V}$ *vs* RHE in 0.1 M CO_2 saturated $KHCO_3$. (a) Raman spectra in spectral range between $200\,\mathrm{cm}^{-1}$ and $2850\,\mathrm{cm}^{-1}$ showing the characteristic bands of Cu_xO and the Raman signatures of graphene, *i.e.*, the G band at $\approx 1585\,\mathrm{cm}^{-1}$ and the 2D band at $\approx 2696\,\mathrm{cm}^{-1}$). (b) *In situ* Raman spectra showing the spectral region, where we expect the bands characteristic for CO_2RR intermediates: adsorbed CO (low spectral range for Cu–CO stretching and upper spectral region for CO) and hydrocarbons. Each spectrum is an average spectrum calculated based on the StreamLine maps collected over $25\times100\,\mu\mathrm{m}^2$ surface area.

Figure B.7 a) shows average Raman spectra calculated from 27 *in situ* Raman spectra covering the spectral range from 200 cm^{-1} and 2850 cm^{-1}. As denoted in Figure 2.7 c), Raman spectrum of G-Cu displays Cu$_x$O bands between 200 cm^{-1} and 800 cm^{-1} and graphene bands: the D band at ≈ 1350 cm^{-1}, the G band at ≈ 1585 cm^{-1}, and the 2D band at ≈ 2696 cm^{-1}.[56,59] Additionally, *in situ* Raman spectra might show the carbonates/bicarbonate Raman bands (spectral region between 1000 cm^{-1} and 1500 cm^{-1}) and the bands of surface adsorbates and CO$_2$RR intermediates. For examples, an *in situ* Raman study on Cu foams[199] reports on a variety of the CO$_2$RR intermediates containing –CO (low-frequency bands characteristic for Cu-CO stretch vibration at 280 cm^{-1} and 360 cm^{-1} and high-frequency intramolecular CO stretch bands between 1960 cm^{-1} and 2130 cm^{-1}) and –CH$_x$ functional groups (bands between 2800 cm^{-1} and 3010 cm^{-1}).

Raman spectra obtained during nanocuboid formation display three bands at 1015 cm^{-1}, ≈ 1585 cm^{-1}, and ≈ 2696 cm^{-1}. We assign the low-intensity band at 1015 cm^{-1} to C–OH stretching of bicarbonate.[199] This band is likely related to the vibration modes of the bicarbonate species in the electrolyte. Furthermore, the bands at ≈ 1585 cm^{-1} and ≈ 2696 cm^{-1} are the G and the 2D bands of graphene. No other bands were detected during nanocuboid formation. Figure B.7 b) shows the Raman spectra in the spectral regions, where one expects the bands of adsorbates and/or CO$_2$RR intermediates containing CO (Cu–CO, –CO) and –CH$_x$ functional groups. The absence of any bands in these spectral regions implies that either the surface nanostructuration upon nanocuboid formation on G-Cu is insufficient to induce surface-enhanced Raman spectroscopy effect or that no adsorbates are present during nanocuboid formation conditions. *In situ* Raman spectroscopy is thus inconclusive on the nature of adsorbates present on G-Cu during nanocuboid evolution. Therefore, the main conclusion on the absence of the surface adsorbates come from *in situ* EC-STM studies in Chapters 3 and 6, where the flat mound terraces and smooth step edges greatly resemble the metallic terraces of Cu(100) single crystals.[94]

C Supplementary Information: Chapter 5

Additional STM images

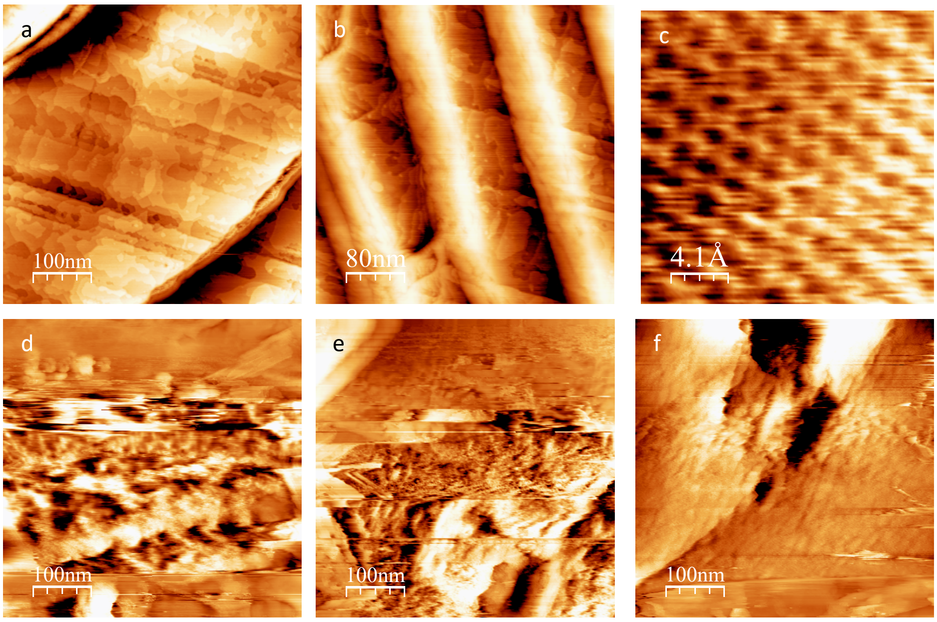

Figure C.1 – Series of *ex situ* STM images showing different (x, y) positions along the G-Cu sample after electrochemical cycling in 0.1 M CO_2 saturated $KHCO_3$ between $-0.6\,V$ and $+0.9\,V$ *vs* RHE. (a) and (b) Large scale STM images of the metallic Cu surface underneath graphene. The wide and flat surface terraces resemble Cu(100) terraces reported in STM study of graphene-covered Cu(100) single crystal.[200] (c) High-resolution STM image showing the graphene lattice. Lattice parameter: a=2.2 Å. (d)-(f) Large scale STM images showing imperfections in the graphene layer.

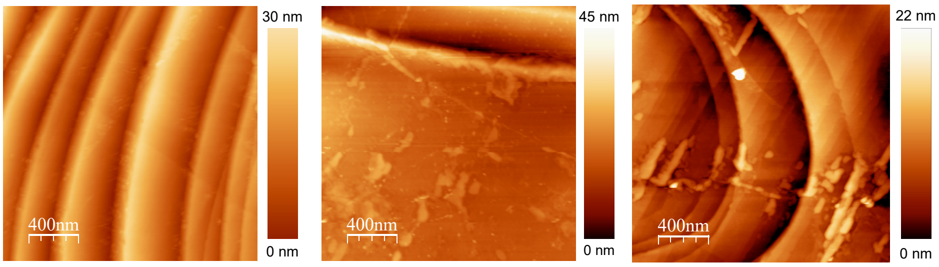

Figure C.2 – AFM height images showing three different positions along G-Cu sample that was cycled in 0.1 M CO_2 saturated $KHCO_3$ between $-0.7\,V$ and $-0.2\,V$ *vs* RHE for 20 cycles. Contrary to Figure 5.5, no NCs were formed upon cycling in this narrow cathodic potential window. These findings confirm that Cu_2O NCs form upon electrodissolution and electrodeposition cycles.

Air-borne hydrocarbon layer on G-Cu

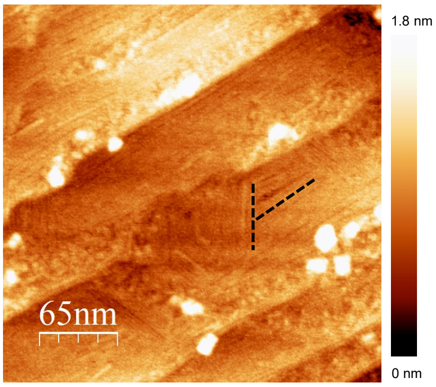

Figure C.3 – AFM height image of as-received G-Cu showing the Cu steps and the striped structure of the air-borne hydrocarbon contamination layer.

Air-borne hydrocarbon contaminants are characteristic for graphitic[1] surfaces. Literature identifies these contaminates through low-force AFM studies at the air/solid[202] and at the water/solid interfaces; however, without any conclusion on their chemical composition. Similarly, we observe these contaminants in AFM studies of pristine G-Cu. No adsorbates, neither in the form of the well-ordered layer, as here, nor as the disordered layer, have ever been visualized on any of our G-Cu samples by (EC-)STM. Also, we have never observed them in *ex situ* AFM characterization on the electrochemically treated G-Cu. These air-borne hydrocarbon contaminants might contribute to the O1s peak component at $\approx 530\,\mathrm{eV}$ and to the C=O and C–O C1s peak components of G-Cu samples (Figures 5.3 and C.5).

---

[1] Uhlig *et al.* report the formation of the same layer on a few-layer MoS_2 and WSe_2.[201]

Quasi *in situ* XPS: Cu nanocuboids *vs* Cu_2O NCs

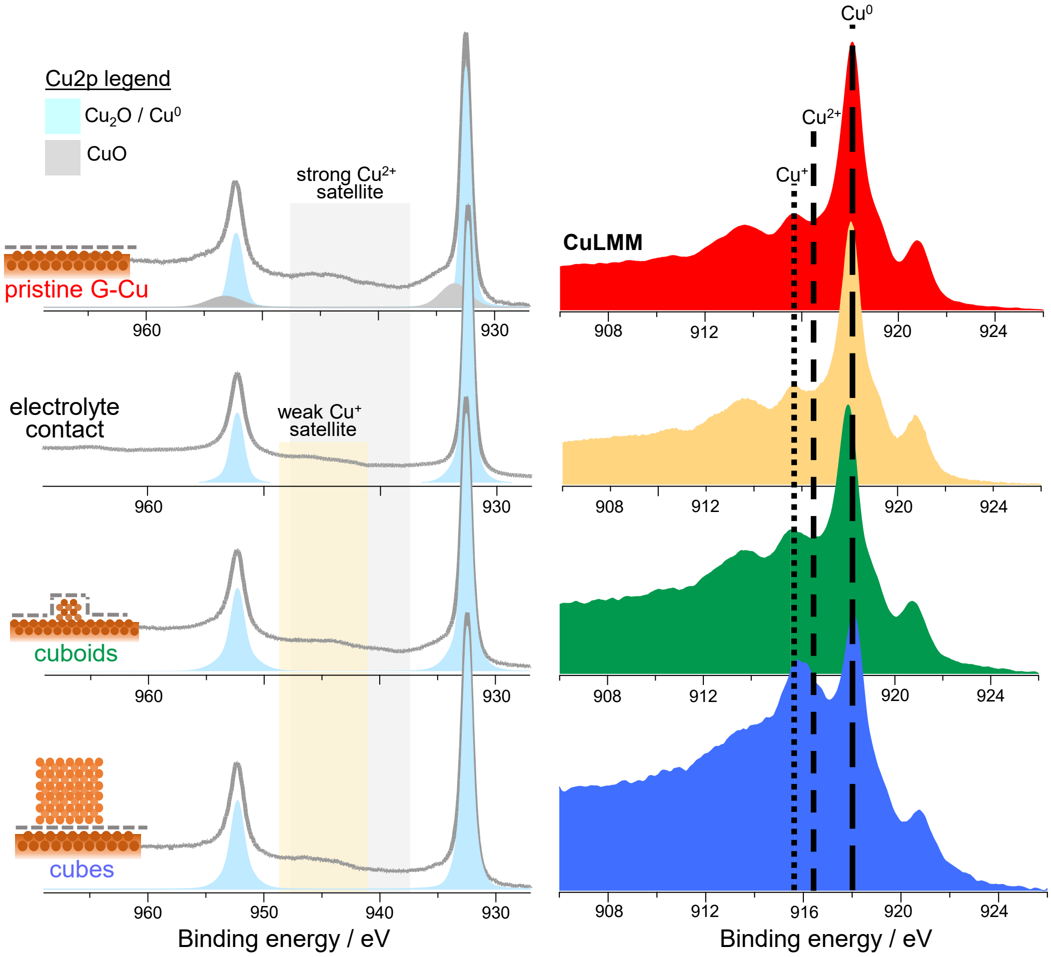

Figure C.4 – Quasi *in situ* Cu2p and CuLMM spectra of pristine (as-received) G-Cu, the same G-Cu sample after being in contact with the electrolyte, Cu nanocuboids on G-Cu, and Cu_2O NCs prepared on G-Cu upon electrochemical cycling. CuLMM spectra for pristine G-Cu, Cu nanocuboids, and the Cu_2O NCs were reproduced from Figure 5.3.

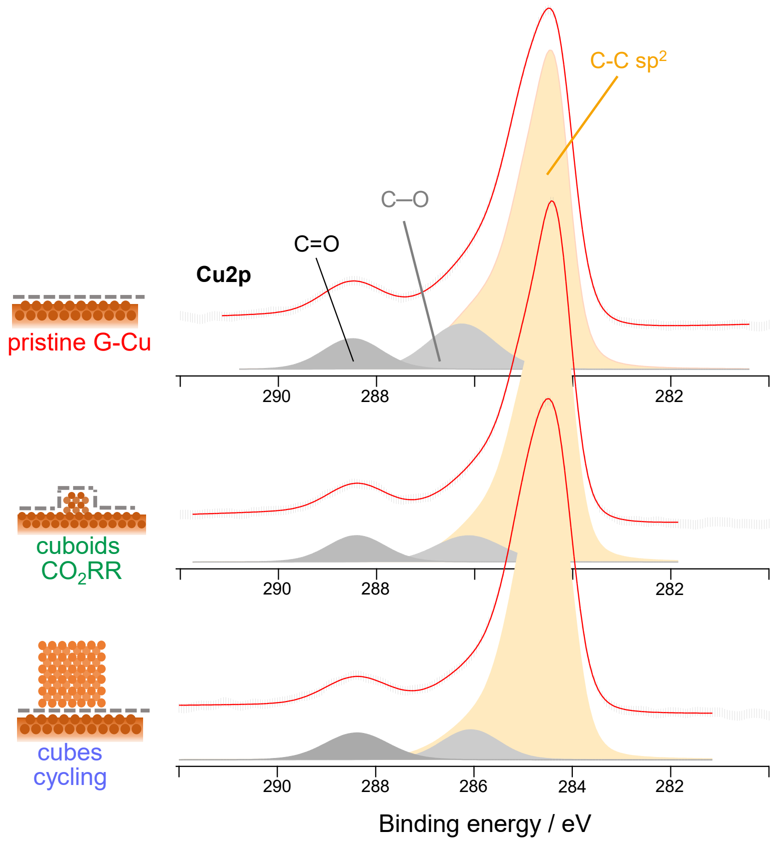

Figure C.5 – Quasi *in situ* C1s XPS spectra of pristine (as-received) G-Cu, G-Cu after Cu nanocuboid formation, and G-Cu after electrochemical cycling. The similarities between these spectra, as well as the similar intensities of the O1s peak component at ≈ 532 eV (Figure 5.3), suggest that there is similar amount of carbonaceous species in all samples. This confirms that graphene remains intact and no additional defects were created in graphene upon electrochemical treatments.

C1s spectra deconvolution reveals the dominant component at 284.4 eV assigned to sp^2-hybridized carbon atoms in decoupled (*i.e.*, oxygen-intercalated) graphene,[65,203] in agreement with the discussion on the fast graphene decoupling upon air exposure in Chapter 4. Two additional components at 286.2 eV and 288.5 eV were assigned to hydroxyl (C–O) and carbonyl (C=O) species, respectively.[203–205] The presence of these species might be related to the the carboxyl (O=C–O) groups on the graphene, known to be the main product of the (G-)Cu oxidation in the wet-environment.[206] Moreover, we cannot exclude the possibility that air-borne hydrocarbon contaminants contribute to C–O and C=O components.

All three C1s peak components remain unchanged for three samples without any shifts in the binding energies and keeping approximately the same intensity ratios with respect to each other. Therefore, all carbon species, including graphene overlayer, remain in the same chemical state upon different treatments as they were on the pristine sample.

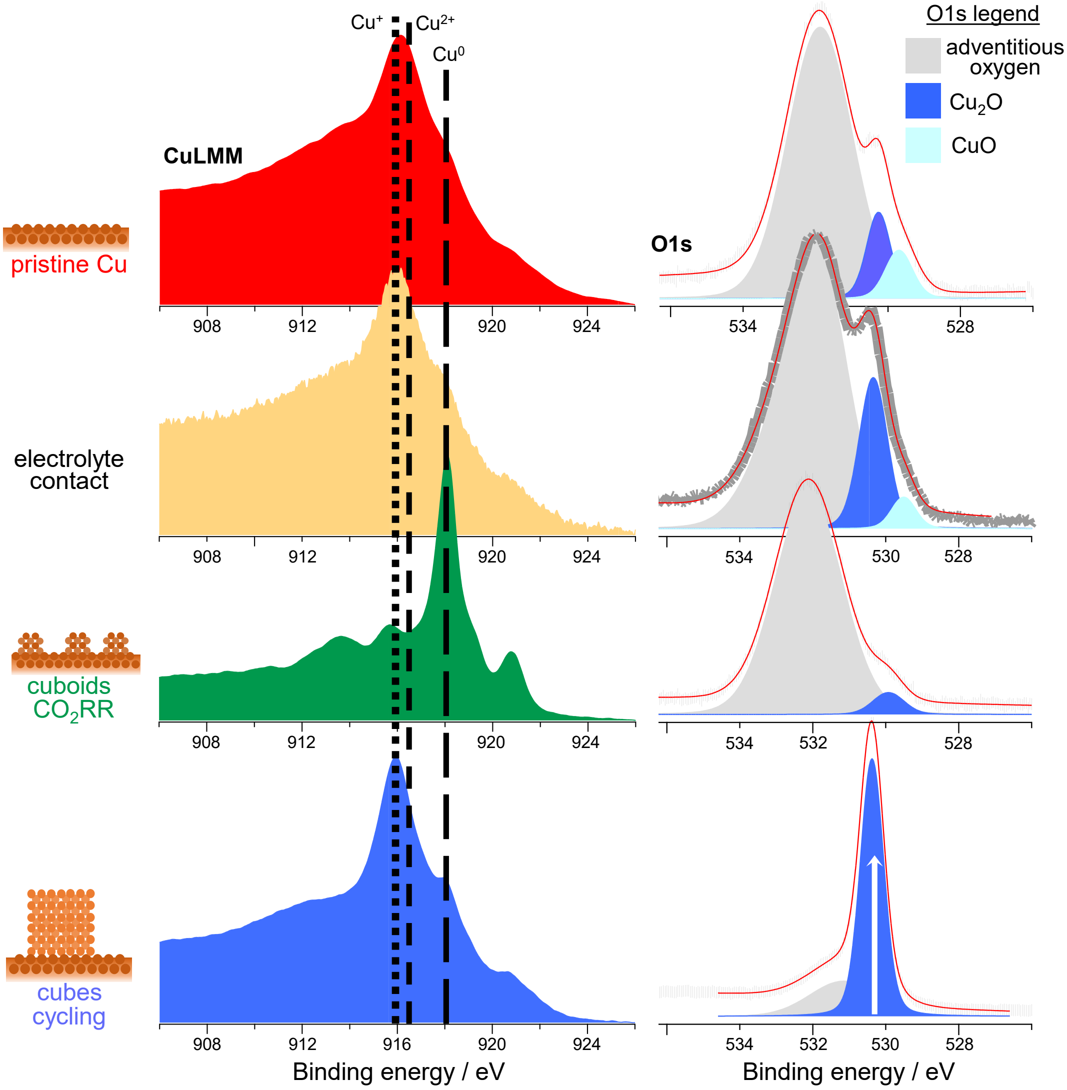

Figure C.6 – Quasi *in situ* CuLMM and O1s spectra of hydrogen-annealed polycrystalline Cu, the same Cu sample after being in contact with the electrolyte, Cu nanocuboids, and Cu_2O NCs, both prepared on hydrogen-annealed polycrystalline Cu foils following the same experimental procedures as for G-Cu (Figure 5.3).

Table C.1 – Binding energies (BE) and assignment of the fitted components in C1s and O1s XPS peaks for G-Cu shown in Figures C.5 and 5.3, respectively. The last column reports Cu2p peak components shown in Figure C.4. Binding energies are 932.6 eV for Cu^0 and Cu^+ peaks and 933.5 eV for Cu^{2+}.

	C1s		O1s		Cu2p
	assignment	BE / eV	assignment	BE / eV	assignment
Pristine	C sp^2	284.4	OH, H_2O, C–O, C=O	531.9	Cu^0 and Cu^+
	C–O	286.2	Cu_2O	530.4	Cu^{2+}
	C=O	288.6	CuO	529.9	
Cu nanocuboids (constant-potential polarization)	C sp^2	284.4	OH, H_2O, C–O, C=O	531.8	Cu^0 and Cu^+
	C–O	286.2	Cu_2O	530.3	
	C=O	288.5			
Cu_2O NCs (electrochemical cycling)	C sp^2	284.4	OH, H_2O, C–O, C=O	531.8	Cu^0 and Cu^+
	C–O	286.2	Cu_2O	530.4	
	C=O	288.5	CuO	529.8	

O1s spectra assignment of G-Cu is not straight-forward because on insufficient knowledge on the chemical composition of the graphene defects upon (G-)Cu ambient oxidation and adventitious carbon species.[65,207] The broad peak centered at 531.8 eV arises from to OH, H_2O, C–O, and C=O species.[206] We thus assign it to the adventitious oxygen species. Similarly as for C1s peak components, the binding energies and the intensities of this peak component remain unchanged for all three samples.

Oxidation states of the pristine, Cu nanocuboids, and the Cu_2O NCs prepared upon electrochemical cycling were deduced from Cu2p, CuLMM, and O1s spectra (Figures C.4 and 5.3). First, pristine G-Cu sample exhibits the characteristic Cu2p peak signature characteristic for a mixture of the metallic Cu/Cu_2O and CuO together with the weak Cu^+ satellites. The presence of metallic Cu and Cu^+ and Cu^{2+} species is also evident in CuLMM peak and further confirmed by O1s peak components at 530.4 eV and 529.9 eV assigned to Cu_2O and CuO, respectively.[65,70] These results revealing the presence of Cu_2O and the small CuO quantities further support the discussion on the heterogeneous Cu oxidation underneath graphene presented in Chapter 4, highlighting the local formation of Cu_2O/ CuO islands in the areas underneath graphene defects.[58]

Second, Cu nanocuboids formed upon constant-potential polarization have Cu2p, CuLMM, and O1s spectra characteristic for the metallic Cu with small amount of Cu_2O. Both Cu2p and CuLMM spectra are dominated by the metallic Cu signatures. Small Cu_2O quantities likely formed upon washing with non-degassed Milli-Q water, in agreement with the fast wet oxidation of the small Cu surface areas underneath graphene defects (Chapter 4).

Third, the Cu_2O NCs prepared upon electrochemical cycling exhibit high-intensity CuLMM peak component at 530.4 eV, suggesting high Cu_2O quantities. Formation of Cu_2O NCs upon electrochemical cycling is in agreement with Grosse *et al.*,[141] who reported the stabilization of Cu_2O NCs upon sequential electrodeposition and electrochemical cycling in $CuSO_4$ solution.

D Supplementary Information: Chapter 6

Additional EC-STM images

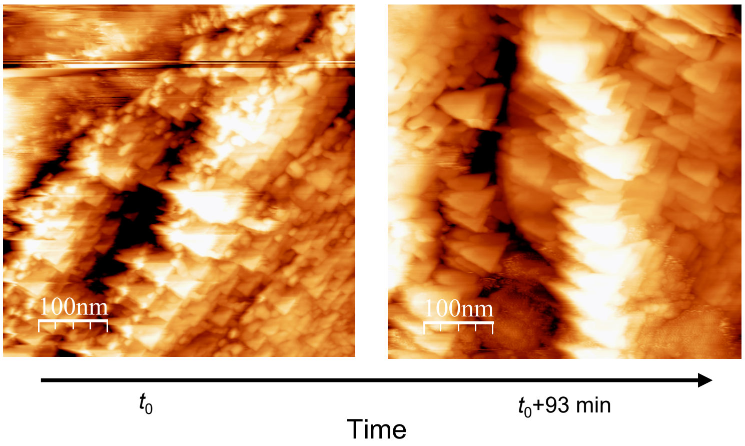

Figure D.1 – EC-STM images showing the triangular (111) mounds formed on (111) crystalline grain of Cu substrate. The images were obtained on G-Cu during potentiostatic polarization in 0.1 M N_2 saturated KOH at -1 V *vs* Pt pseudo-RE.

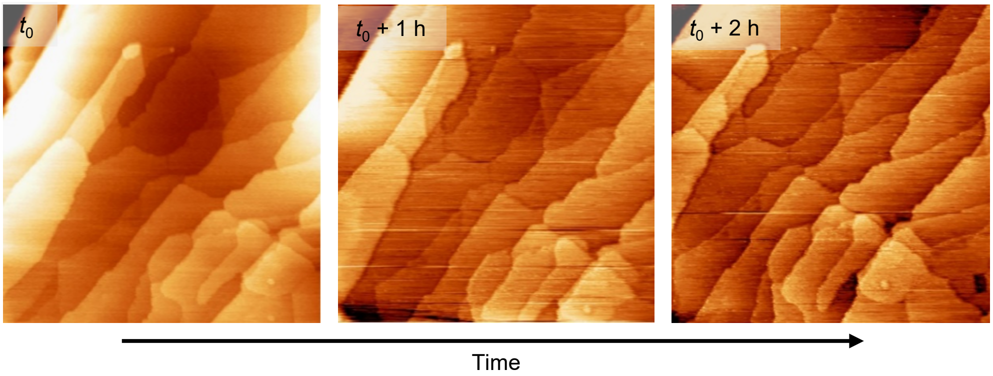

Figure D.2 – EC-STM images showing the stability of the step edge bunches over 2 hours. The images were obtained on G-Cu during potentiostatic polarization in 0.1 M CO_2 saturated $KHCO_3$ at $-1.6\,V$ *vs* Pt pseudo-RE. Scan size: 300×300 nm^2.

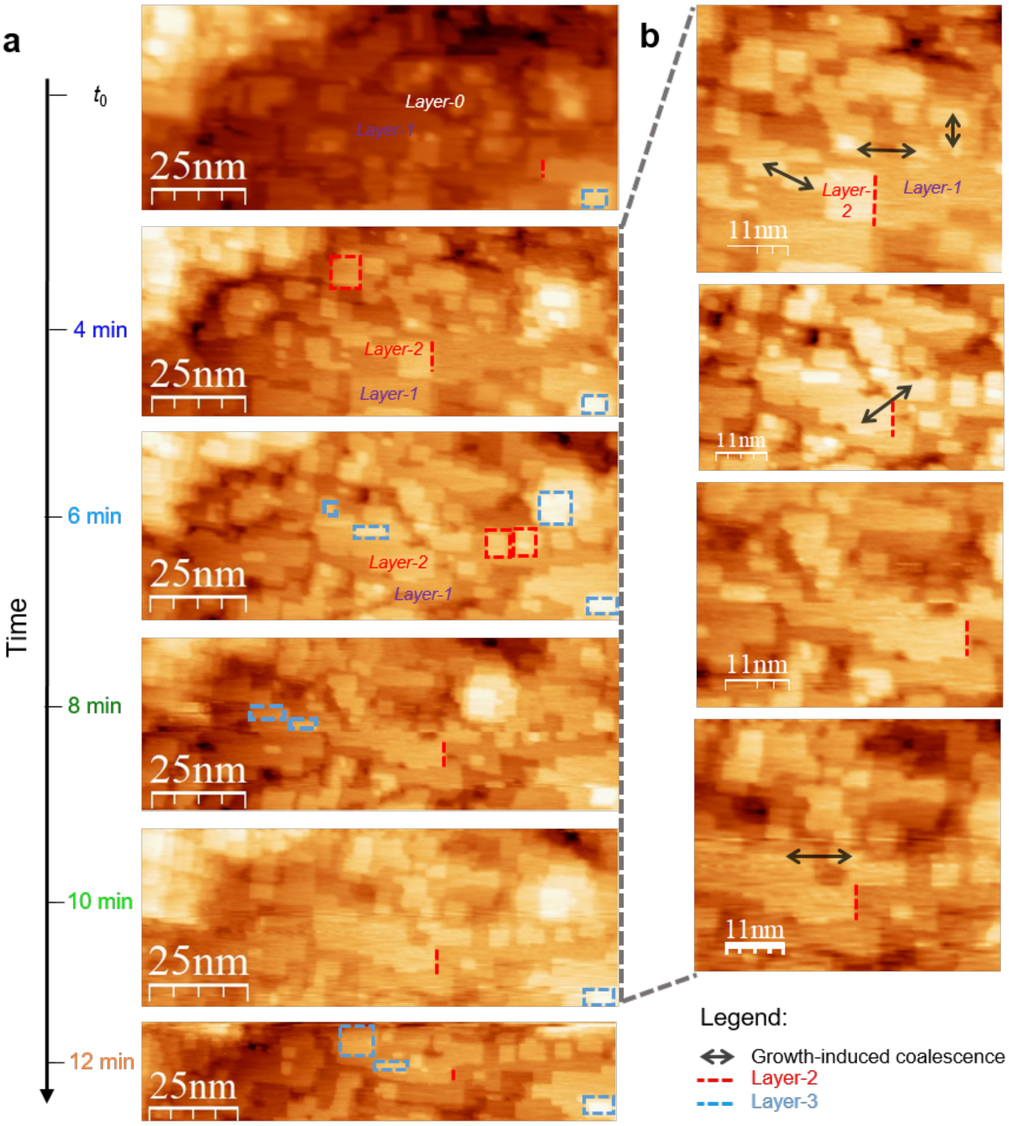
a
b
Time
t_0
4 min
6 min
8 min
10 min
12 min
Layer-0
Layer-1
Layer-2
25nm
11nm
Legend:
Growth-induced coalescence
Layer-2
Layer-3

Figure D.3 – Consecutive EC-STM images showing formation of the mounds. Great resemblance between the processes in Figure 6.6 confirms that the mounds form through kinetic roughening.

Product analysis

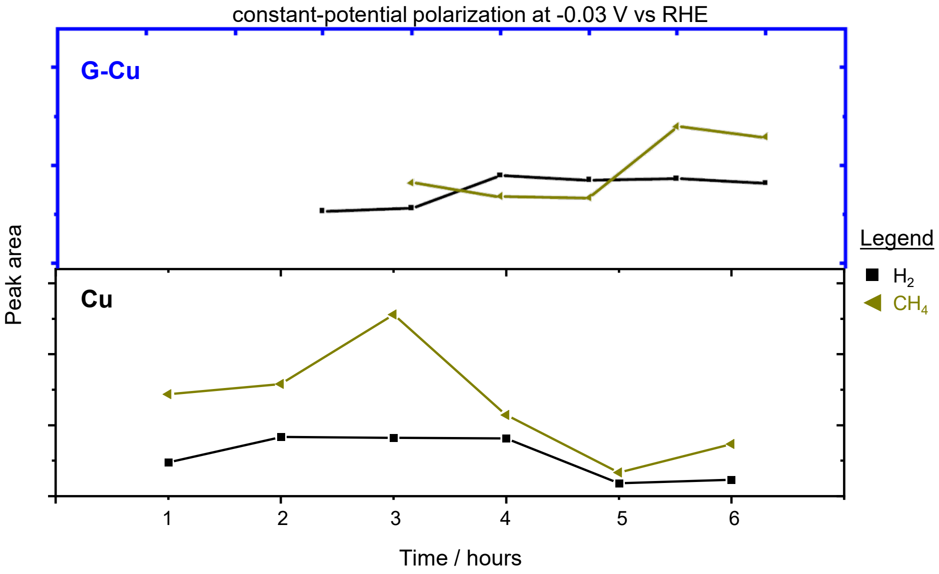

Figure D.4 – Qualitative analysis of the gas product evolved on the mounds. Note that y-axis denotes the areas of the chromatogram peaks. The absence of the data points for CH_4 and H_2 on G-Cu (Cu) at t=1 and 2 hours (7 and 8 hours) is due to unsuccessful injection of the gas samples to the gas chromatograph. Constant-potential CO_2RR was conducted on G-Cu and bare, polycrystalline Cu in 0.1 M CO_2 saturated $KHCO_3$ at -0.03 V *vs* RHE.

We followed the evolution of CO_2RR gas products during the mound formation. Direct translation of the experimental conditions under which *in situ* EC-STM studies were conducted to CO_2RR gas products analysis is rather challenging experimental task. This is because EC-STM experiments were conducted at low CO_2RR overpotentials associated with the low geometrical activity. To mimic the conditions of EC-STM experiments, under which we now fully understand the process of mounds formation, we conducted gas product analysis during chronoamperometric polarization in 0.1 M CO_2 saturated $KHCO_3$ at -0.03 V *vs* RHE (Figure D.4). The experiments were carried out on G-Cu (top panel) and on Cu (bottom panel) to discard any effects associated with graphene. In both cases, low quantities of the gas products, evolved under these conditions, were under the detection limits for quantitative analysis. We were thus limit us to qualitative analysis. We reported the areas of the chromatogram peaks rather than faradaic efficiencies that are regularly reported for quantitative CO_2RR product analysis. In such qualitative analysis, any changes in the chromatogram peak areas were not necessarily related to the quantitative changes. Therefore, Figure D.4 reports the data points only if the product was detected by gas chromatography. The missing data points for CH_4 and H_2 are related to an unsuccessful injection of the gas sample to the gas chromatograph. Further details on these experiments are denoted in the Section 6.2. Finally, we note that the peak of water overlaps with the peak of CO in thermal conductivity detector. These experiments were limited to detection of H_2, CH_4, and C_2H_4.

CH_4 and H_2 were produced on the mounds, while no C_2H_4 was detected. Similarities in qualitative results for both G-Cu and Cu indicate that graphene has no impact on the product selectivity. Therefore, the relationship between the morphology and the product selectivity is unaffected by graphene. We further comment these findings together for both Cu and G-Cu.

H_2 production is in agreement with the competition between HER and CO_2RR, where HER is unavoidable and often considered as parasitic side-reaction whenever aiming for high selectivity toward CO_2RR. In this particular case, H_2 evolution at such a low overpotential is likely related to the significant HER activity of Cu(100) single crystal.[174] Simultaneous CH_4 production is unexpected for such a low overpotential of $+0.2\,\mathrm{V}$ ($E_0 = +0.17\,\mathrm{V}$ *vs* RHE calculated from on the free energy of CH_4 formation[30]), that is more positive than the onset potentials reported in OLEMS studies on single crystalline and polycrystalline Cu surfaces (being $-0.65\,\mathrm{V}$ *vs* RHE[98]). Furthermore, the pathway towards CH_4 includes CO as the key intermediate together with formate and formaldehyde as by-products. We thus speculate that CO (in gas phase) and formate (in liquid phase) are also produced on the mounds.

Bibliography

[1] H. Tissot, C. Wang, J. H. Stenlid, T. Brinck, and J. Weissenrieder, *State of the Global Climate 2020*, Tech. Rep. (2020).

[2] NOAA National Centers for Environmental Information (NCEI), "Billion-dollar weather and climate disasters (2021)," https://www.ncdc.noaa.gov/billions/.

[3] United Nations Framework Convention on Climate Change, "Adoption of the Paris Agreement," (2015).

[4] E. Union, "Proposal for a European Climate Law," (2020).

[5] X.-G. Zhu, S. P. Long, and D. R. Ort, "What is the maximum efficiency with which photosynthesis can convert solar energy into biomass?" Curr. Opin. Biotechnol. **19**, 153–159 (2008).

[6] D. O. Hall and K. K. Rao, *Photosynthesis*, sixth ed. (Cambridge University Press, United Kingdom, 1999).

[7] J. R. Galan-Mascaros, "Photoelectrochemical solar fuels from carbon dioxide, water and sunlight," Catal. Sci. Technol. **10**, 1967–1974 (2020).

[8] M. Schreier, F. Héroguel, L. Steier, S. Ahmad, J. S. Luterbacher, M. T. Mayer, J. Luo, and M. Grätzel, "Solar conversion of CO_2 to CO using Earth-abundant electrocatalysts prepared by atomic layer modification of CuO," Nat. Energy **2**, 17087 (2017).

[9] M. Schreier, L. Curvat, F. Giordano, L. Steier, A. Abate, S. M. Zakeeruddin, J. Luo, M. T. Mayer, and M. Grätzel, "Efficient photosynthesis of carbon monoxide from CO_2 using perovskite photovoltaics," Nat. Commun. **6**, 7326 (2015).

[10] T. Arai, S. Sato, K. Sekizawa, T. M. Suzuki, and T. Morikawa, "Solar-driven CO_2 to CO reduction utilizing H_2O as an electron donor by earth-abundant Mn–bipyridine complex and Ni-modified Fe-oxyhydroxide catalysts activated in a single-compartment reactor," Chem. Commun. **55**, 237–240 (2018).

[11] C. Battaglia, A. Cuevas, and S. D. Wolf, "High-efficiency crystalline silicon solar cells: status and perspectives," Energy Environ. Sci. **9**, 1552–1576 (2016).

[12] G. Piao, S. H. Yoon, D. S. Han, and H. Park, "Ion-Enhanced Conversion of CO_2 into Formate on Porous Dendritic Bismuth Electrodes with High Efficiency and Durability," ChemSusChem **13**, 698–706 (2020).

[13] M. Asadi, K. Kim, C. Liu, A. V. Addepalli, P. Abbasi, P. Yasaei, P. Phillips, A. Behranginia, J. M. Cerrato, R. Haasch, P. Zapol, B. Kumar, R. F. Klie, J. Abiade, L. A. Curtiss, and A. Salehi-Khojin, "Nanostructured transition metal dichalcogenide electrocatalysts for CO_2 reduction in ionic liquid," Science **353**, 467–470 (2016).

[14] U. Kang, S. K. Choi, D. J. Ham, S. M. Ji, W. Choi, D. S. Han, A. Abdel-Wahab, and H. Park, "Photosynthesis of formate from CO_2 and water at 1% energy efficiency via copper iron oxide catalysis," Energy Environ. Sci. **8**, 2638–2643 (2015).

[15] X. Zhou, R. Liu, K. Sun, Y. Chen, E. Verlage, S. A. Francis, N. S. Lewis, and C. Xiang, "Solar-Driven Reduction of 1 atm of CO_2 to Formate at 10% Energy-Conversion Efficiency by Use of a TiO_2-Protected III–V Tandem Photoanode in Conjunction with a Bipolar Membrane and a Pd/C Cathode," ACS Energy Lett. **1**, 764–770 (2016).

[16] T. Arai, S. Sato, T. Kajino, and T. Morikawa, "Solar CO_2 reduction using H_2O by a semiconductor/metal-complex hybrid photocatalyst: enhanced efficiency and demonstration of a wireless system using $SrTiO_3$ photoanodes," Energy Environ. Sci. **6**, 1274–1282 (2013).

[17] S. Sato, T. Arai, T. Morikawa, K. Uemura, T. M. Suzuki, H. Tanaka, and T. Kajino, "Selective CO_2 Conversion to Formate Conjugated with H_2O Oxidation Utilizing Semiconductor/Complex Hybrid Photocatalysts," J. Am. Chem. Soc. **133**, 15240–15243 (2011).

[18] K. Sekizawa, S. Sato, T. Arai, and T. Morikawa, "Solar-Driven Photocatalytic CO_2 Reduction in Water Utilizing a Ruthenium Complex Catalyst on p-Type Fe_2O_3 with a Multiheterojunction," ACS Catal. **8**, 1405–1416 (2018).

[19] V. Andrei, B. Reuillard, and E. Reisner, "Bias-free solar syngas production by integrating a molecular cobalt catalyst with perovskite–BiVO 4 tandems," Nat. Mater. **19**, 189–194 (2020).

[20] Gurudayal, J. W. Beeman, J. Bullock, H. Wang, J. Eichhorn, C. Towle, A. Javey, F. M. Toma, N. Mathews, and J. W. Ager, "Si photocathode with Ag-supported dendritic Cu catalyst for CO_2 reduction," Energy Environ. Sci. **12**, 1068–1077 (2019).

[21] Y. J. Jang, I. Jeong, J. Lee, J. Lee, M. J. Ko, and J. S. Lee, "Unbiased Sunlight-Driven Artificial Photosynthesis of Carbon Monoxide from CO_2 Using a ZnTe-Based Photocathode and a Perovskite Solar Cell in Tandem," ACS Nano **10**, 6980–6987 (2016).

[22] Y. Ham, V. Ri, J. Kim, Y. Yoon, J. Lee, K. Kang, K.-S. An, C. Kim, and S. Jeon, "Multi-redox phenazine/non-oxidized graphene/cellulose nanohybrids as ultrathick cathodes for high-energy organic batteries," Nano Res. **14**, 1382–1389 (2021).

[23] H. Kumagai, G. Sahara, K. Maeda, M. Higashi, R. Abe, and O. Ishitani, "Hybrid photocathode consisting of a $CuGaO_2$ p-type semiconductor and a Ru(II)–Re(I) supramolecular photocatalyst: non-biased visible-light-driven CO_2 reduction with water oxidation," Chem. Sci. **8**, 4242–4249 (2017).

[24] L. J. Sonter, M. C. Dade, J. E. M. Watson, and R. K. Valenta, “Renewable energy production will exacerbate mining threats to biodiversity,” Nat. Commun. **11**, 4174 (2020).

[25] B. Moss, F. S. Hegner, S. Corby, S. Selim, L. Francàs, N. López, S. Giménez, J.-R. Galán-Mascarós, and J. R. Durrant, “Unraveling Charge Transfer in CoFe Prussian Blue Modified BiVO4 Photoanodes,” ACS Energy Lett. **4**, 337–342 (2019).

[26] S. Corby, M.-G. Tecedor, S. Tengeler, C. Steinert, B. Moss, C. A. Mesa, H. F. Heiba, A. A. Wilson, B. Kaiser, W. Jaegermann, L. Francàs, S. Gimenez, and J. R. Durrant, “Separating bulk and surface processes in NiOx electrocatalysts for water oxidation,” Sustainable Energy Fuels **4**, 5024–5030 (2020).

[27] D. Cardenas-Morcoso, M. García-Tecedor, T. Merdzhanova, V. Smirnov, F. Finger, B. Kaiser, W. Jaegermann, and S. Gimenez, “An integrated photoanode based on non-critical raw materials for robust solar water splitting,” Mater. Adv. **1**, 1202–1211 (2020).

[28] T. H. Phan, K. Banjac, F. P. Cometto, F. Dattila, R. García-Muelas, S. J. Raaijman, C. Ye, M. T. M. Koper, N. Lopez, and M. Lingenfelder, “Emergence of Potential-Controlled Cu-Nanocuboids and Graphene-Covered Cu-Nanocuboids under Operando CO_2 Electroreduction,” Nano Lett. **21**, 2059–2065 (2021).

[29] J. Li, G. Chen, Y. Zhu, Z. Liang, A. Pei, C.-L. Wu, H. Wang, H. R. Lee, K. Liu, S. Chu, and Y. Cui, “Efficient electrocatalytic CO_2 reduction on a three-phase interface,” Nat. Catal. **1**, 592 (2018).

[30] S. Nitopi, E. Bertheussen, S. B. Scott, X. Liu, A. K. Engstfeld, S. Horch, B. Seger, I. E. L. Stephens, K. Chan, C. Hahn, J. K. Nørskov, T. F. Jaramillo, and I. Chorkendorff, “Progress and Perspectives of Electrochemical CO_2 Reduction on Copper in Aqueous Electrolyte,” Chem. Rev. **119**, 7610–7672 (2019).

[31] Y. Hori, K. Kikuchi, and S. Suzuki, “Production of CO and CH_4 in electrochemical reduction of CO_2 at metal electrodes in aqueous hydrogencarbonate solution,” Chem. Lett. **14**, 1695–1698 (1985).

[32] Y. Hori, “Electrochemical CO_2 Reduction on Metal Electrodes,” in *Modern Aspects of Electrochemistry*, Modern Aspects of Electrochemistry (Springer, New York, NY, 2008) pp. 89–189.

[33] A. Bagger, L. Arnarson, M. H. Hansen, E. Spohr, and J. Rossmeisl, “Electrochemical CO Reduction: A Property of the Electrochemical Interface,” J. Am. Chem. Soc. **141**, 1506–1514 (2019).

[34] Y. Hori, I. Takahashi, O. Koga, and N. Hoshi, “Selective Formation of C_2 Compounds from Electrochemical Reduction of CO_2 at a Series of Copper Single Crystal Electrodes,” J. Phys. Chem. B **106**, 15–17 (2002).

[35] A. Loiudice, P. Lobaccaro, E. A. Kamali, T. Thao, B. H. Huang, J. W. Ager, and R. Buonsanti, “Tailoring Copper Nanocrystals towards C_2 Products in Electrochemical CO_2 Reduction,” Angew. Chem. Int. Ed. **55**, 5789–5792 (2016).

[36] F. S. Roberts, K. P. Kuhl, and A. Nilsson, “High selectivity for ethylene from carbon dioxide reduction over copper nanocube electrocatalysts,” Angew. Chem. Int. Ed. **54**, 5179–5182 (2015).

[37] K. Jiang, R. B. Sandberg, A. J. Akey, X. Liu, D. C. Bell, J. K. Nørskov, K. Chan, and H. Wang, “Metal ion cycling of Cu foil for selective C–C coupling in electrochemical CO_2 reduction,” Nat. Catal. **1**, 111–119 (2018).

[38] T. Kim and G. T. R. Palmore, “A scalable method for preparing Cu electrocatalysts that convert CO_2 into C_{2+} products,” Nat. Commun. **11**, 3622 (2020).

[39] R. Kas, R. Kortlever, A. Milbrat, M. T. M. Koper, G. Mul, and J. Baltrusaitis, “Electrochemical CO_2 reduction on Cu_2O-derived copper nanoparticles: Controlling the catalytic selectivity of hydrocarbons,” Phys. Chem. Chem. Phys. **16**, 12194–12201 (2014).

[40] M. Ma, K. Djanashvili, and W. A. Smith, “Selective electrochemical reduction of CO_2 to CO on CuO-derived Cu nanowires,” Phys. Chem. Chem. Phys. **17**, 20861–20867 (2015).

[41] D. Ren, Y. Deng, A. D. Handoko, C. S. Chen, S. Malkhandi, and B. S. Yeo, “Selective Electrochemical Reduction of Carbon Dioxide to Ethylene and Ethanol on Copper(I) Oxide Catalysts,” ACS Catal. **5**, 2814–2821 (2015).

[42] C. W. Li, J. Ciston, and M. W. Kanan, “Electroreduction of carbon monoxide to liquid fuel on oxide-derived nanocrystalline copper,” Nature **508**, 504–507 (2014).

[43] A. Verdaguer-Casadevall, C. W. Li, T. P. Johansson, S. B. Scott, J. T. McKeown, M. Kumar, I. E. L. Stephens, M. W. Kanan, and I. Chorkendorff, “Probing the Active Surface Sites for CO Reduction on Oxide-Derived Copper Electrocatalysts,” J. Am. Chem. Soc. **137**, 9808–9811 (2015).

[44] M. Favaro, H. Xiao, T. Cheng, W. A. Goddard, J. Yano, and E. J. Crumlin, “Subsurface oxide plays a critical role in CO_2 activation by Cu(111) surfaces to form chemisorbed CO_2, the first step in reduction of CO_2,” Proc. Natl. Acad. Sci. U.S.A. **114**, 6706–6711 (2017).

[45] A. Eilert, F. Cavalca, F. S. Roberts, J. Osterwalder, C. Liu, M. Favaro, E. J. Crumlin, H. Ogasawara, D. Friebel, L. G. M. Pettersson, and A. Nilsson, “Subsurface Oxygen in Oxide-Derived Copper Electrocatalysts for Carbon Dioxide Reduction,” J. Phys. Chem. Lett. **8**, 285–290 (2017).

[46] J. Huang, N. Hörmann, E. Oveisi, A. Loiudice, G. L. D. Gregorio, O. Andreussi, N. Marzari, and R. Buonsanti, “Potential-induced nanoclustering of metallic catalysts during electrochemical CO_2 reduction,” Nat. Commun. **9**, 3117 (2018).

[47] Y.-G. Kim, J. H. Baricuatro, A. Javier, J. M. Gregoire, and M. P. Soriaga, “The evolution of the polycrystalline copper surface, first to Cu(111) and then to Cu(100), at a fixed CO_2RR potential: a study by operando EC–STM,” Langmuir **30**, 15053–15056 (2014).

[48] D. Kim, C. S. Kley, Y. Li, and P. Yang, "Copper nanoparticle ensembles for selective electroreduction of CO_2 to C_2–C_3 products," Proc. Natl. Acad. Sci. U.S.A. **114**, 10560–10565 (2017).

[49] B. Voigtländer, *Scanning Probe Microscopy: Atomic Force Microscopy and Scanning Tunneling Microscopy*, NanoScience and Technology (Springer Berlin Heidelberg, Berlin, Heidelberg, 2015).

[50] B. W. Stel, *In situ Studies of Peptide and Protein Assemblies at the Solid-Liquid Interface: Hierarchical Self-Assembly, Dynamics and Functional Properties*, Doctoral thesis, Ecole Polytechnique Federale de Lausanne, Lausanne (2017).

[51] I. Horcas, R. Fernández, J. M. Gómez-Rodríguez, J. Colchero, J. Gómez-Herrero, and A. M. Baro, "WSXM: A software for scanning probe microscopy and a tool for nanotechnology," Rev. Sci. Instrum. **78**, 013705 (2007).

[52] J. Tersoff and D. R. Hamann, "Theory and Application for the Scanning Tunneling Microscope," Phys. Rev. Lett. **50**, 1998–2001 (1983).

[53] J. Bardeen, "Tunnelling from a Many-Particle Point of View," Phys. Rev. Lett. **6**, 57–59 (1961).

[54] M. Bowker and P. R. Davies, eds., *Scanning Tunneling Microscopy in Surface Science* (John Wiley & Sons, Ltd, 2009).

[55] R. Kazinczi, E. Szõcs, E. Kálmán, and P. Nagy, "Novel methods for preparing EC STM tips," Appl. Phys. A **66**, S535–S538 (1998).

[56] S. D. Costa, A. Righi, C. Fantini, Y. Hao, C. Magnuson, L. Colombo, R. S. Ruoff, and M. A. Pimenta, "Resonant Raman spectroscopy of graphene grown on copper substrates," Solid State Commun. **152**, 1317–1320 (2012).

[57] J. Azpeitia, I. Palacio, J. I. Martínez, I. Muñoz-Ochando, K. Lauwaet, F. J. Mompean, G. J. Ellis, M. García-Hernández, J. A. Martín-Gago, C. Munuera, and M. F. López, "Oxygen intercalation in PVD graphene grown on copper substrates: A decoupling approach," Appl. Surf. Sci. **529**, 147100 (2020).

[58] U. Lee, Y. Han, S. Lee, J. S. Kim, Y. H. Lee, U. J. Kim, and H. Son, "Time Evolution Studies on Strain and Doping of Graphene Grown on a Copper Substrate Using Raman Spectroscopy," ACS Nano **14**, 919–926 (2020).

[59] L. Álvarez Fraga, J. Rubio-Zuazo, F. Jiménez-Villacorta, E. Climent-Pascual, R. Ramírez-Jiménez, C. Prieto, and A. de Andrés, "Oxidation Mechanisms of Copper under Graphene: The Role of Oxygen Encapsulation," Chem. Mater. **29**, 3257–3264 (2017).

[60] C. Zhan, F. Dattila, C. Rettenmaier, A. Bergmann, S. Kühl, R. García-Muelas, N. López, and B. R. Cuenya, "Revealing the CO Coverage-Driven C–C Coupling Mechanism for Electrochemical CO2 Reduction on Cu2O Nanocubes via Operando Raman Spectroscopy," ACS Catal. **11**, 7694–7701 (2021).

[61] O. Frank, J. Vejpravova, V. Holy, L. Kavan, and M. Kalbac, “Interaction between graphene and copper substrate: The role of lattice orientation,” Carbon **68**, 440–451 (2014).

[62] C. Neumann, S. Reichardt, P. Venezuela, M. Drögeler, L. Banszerus, M. Schmitz, K. Watanabe, T. Taniguchi, F. Mauri, B. Beschoten, S. V. Rotkin, and C. Stampfer, “Raman spectroscopy as probe of nanometre-scale strain variations in graphene,” Nat. Commun. **6**, 8429 (2015).

[63] S. Lee, K. Banjac, M. Lingenfelder, and X. Hu, “Oxygen Isotope Labeling Experiments Reveal Different Reaction Sites for the Oxygen Evolution Reaction on Nickel and Nickel Iron Oxides,” Angew. Chem. Int. Ed. **58**, 10295–10299 (2019).

[64] P. van der Heide, *X-ray Photoelectron Spectroscopy: An introduction to Principles and Practices* (John Wiley & Sons, Inc., New Jersey, 2012).

[65] P. R. Kidambi, B. C. Bayer, R. Blume, Z.-J. Wang, C. Baehtz, R. S. Weatherup, M.-G. Willinger, R. Schloegl, and S. Hofmann, “Observing Graphene Grow: Catalyst–Graphene Interactions during Scalable Graphene Growth on Polycrystalline Copper,” Nano Lett. **13**, 4769–4778 (2013).

[66] I. Wlasny, P. Dabrowski, M. Rogala, P. J. Kowalczyk, I. Pasternak, W. Strupinski, J. M. Baranowski, and Z. Klusek, “Role of graphene defects in corrosion of graphene-coated Cu(111) surface,” Appl. Phys. Lett. **102**, 111601 (2013).

[67] A. A. Permyakova, J. Herranz, M. El Kazzi, J. S. Diercks, M. Povia, L. R. Mangani, M. Horisberger, A. Pătru, and T. J. Schmidt, “On the Oxidation State of Cu_2O upon Electrochemical CO_2 Reduction: An XPS Study,” ChemPhysChem **20**, 3120–3127 (2019).

[68] B. Wurster, *Two-Dimensional Metal-Organic Networks as a New Class of Electrocatalysts*, Doctoral thesis, Ecole Polytechnique Federale de Lausanne, Lausanne (2015).

[69] D. Hötger, *Metal-Organic and Oxide Nanostructures for Electrocatalyzing the Oxygen Half-Cell Reaction*, Doctoral thesis, Ecole Polytechnique Federale de Lausanne, Lausanne (2018).

[70] M. C. Biesinger, “Advanced analysis of copper X-ray photoelectron spectra,” Surf. Interface Anal. **49**, 1325–1334 (2017).

[71] Y. Y. Birdja, J. Shen, and M. T. M. Koper, “Influence of the metal center of metalloprotoporphyrins on the electrocatalytic CO_2 reduction to formic acid,” Catalysis Today **288**, 37–47 (2017).

[72] J. M. MacLeod and F. Rosei, “Molecular Self-Assembly on Graphene,” Small **10**, 1038–1049 (2014).

[73] S. Chen, L. Brown, M. Levendorf, W. Cai, S.-Y. Ju, J. Edgeworth, X. Li, C. W. Manguson, A. Velamakanni, R. D. Pinert, J. Kang, J. Park, and R. S. Ruoff, “Oxidation Resistance of Graphene-Coated Cu and Cu/Ni Alloy,” ACS Nano **5**, 1321–1327 (2011).

[74] J. M. Wofford, S. Nie, K. F. McCarty, N. C. Bartelt, and O. D. Dubon, "Graphene Islands on Cu Foils: The Interplay between Shape, Orientation, and Defects," Nano Lett. **10**, 4890–4896 (2010).

[75] A.-Y. Lu, S.-Y. Wei, C.-Y. Wu, Y. Hernandez, T.-Y. Chen, T.-H. Liu, C.-W. Pao, F.-R. Chen, L.-J. Li, and Z.-Y. Juang, "Decoupling of CVD graphene by controlled oxidation of recrystallized Cu," RSC Adv. **2**, 3008–3013 (2012).

[76] Q. Fu and X. Bao, "Surface chemistry and catalysis confined under two-dimensional materials," Chem. Soc. Rev. **46**, 1842–1874 (2017).

[77] D. E. Hurtado Salinas, *Design of Surface-Supported Bio-inspired Networks for* CO_2 *and* O_2 *Activation at Room Temperature*, Doctoral thesis, Ecole Polytechnique Fédérale de Lausanne, Lausanne (2018).

[78] Y. Hori, A. Murata, R. Takahashi, and S. Suzuki, "Enhanced formation of ethylene and alcohols at ambient temperature and pressure in electrochemical reduction of carbon dioxide at a copper electrode," J. Chem. Soc., Chem. Commun. **1**, 17–19 (1988).

[79] Y. Hori, A. Murata, R. Takahashi, and S. Suzuki, "Electroreduction of carbon monoxide to methane and ethylene at a copper electrode in aqueous solutions at ambient temperature and pressure," J. Am. Chem. Soc. **109**, 5022–5023 (1987).

[80] Y. Wang, Z. Wang, C.-T. Dinh, J. Li, A. Ozden, M. Golam Kibria, A. Seifitokaldani, C.-S. Tan, C. M. Gabardo, M. Luo, H. Zhou, F. Li, Y. Lum, C. McCallum, Y. Xu, M. Liu, A. Proppe, A. Johnston, P. Todorovic, T.-T. Zhuang, D. Sinton, S. O. Kelley, and E. H. Sargent, "Catalyst synthesis under CO_2 electroreduction favours faceting and promotes renewable fuels electrosynthesis," Nat. Catal. **3**, 98–106 (2020).

[81] Y. Kwon, Y. Lum, E. L. Clark, J. W. Ager, and A. T. Bell, "CO_2 Electroreduction with Enhanced Ethylene and Ethanol Selectivity by Nanostructuring Polycrystalline Copper," ChemElectroChem **3**, 1012–1019 (2016).

[82] C. W. Li and M. W. Kanan, "CO_2 Reduction at Low Overpotential on Cu Electrodes Resulting from the Reduction of Thick Cu_2O Films," J. Am. Chem. Soc. **134**, 7231–7234 (2012).

[83] R. Kas, R. Kortlever, H. Yılmaz, M. T. M. Koper, and G. Mul, "Manipulating the Hydrocarbon Selectivity of Copper Nanoparticles in CO_2 Electroreduction by Process Conditions," ChemElectroChem **2**, 354–358 (2015).

[84] G. L. De Gregorio, T. Burdyny, A. Loiudice, P. Iyengar, W. A. Smith, and R. Buonsanti, "Facet-Dependent Selectivity of Cu Catalysts in Electrochemical CO2 Reduction at Commercially Viable Current Densities," ACS Catal. **10**, 4854–4862 (2020).

[85] C. S. Chen, A. D. Handoko, J. H. Wan, L. Ma, D. Ren, and B. S. Yeo, "Stable and selective electrochemical reduction of carbon dioxide to ethylene on copper mesocrystals," Catal. Sci. Technol. **5**, 161–168 (2014).

[86] D. H. Jung, C. Kang, M. Kim, H. Cheong, H. Lee, and J. S. Lee, “Effects of Hydrogen Partial Pressure in the Annealing Process on Graphene Growth,” J. Phys. Chem. C **118**, 3574–3580 (2014).

[87] S. H. Lee, J. C. Lin, M. Farmand, A. T. Landers, J. T. Feaster, J. E. Avilés Acosta, J. W. Beeman, Y. Ye, J. Yano, A. Mehta, R. C. Davis, T. F. Jaramillo, C. Hahn, and W. S. Drisdell, “Oxidation State and Surface Reconstruction of Cu under CO_2 Reduction Conditions from In Situ X-ray Characterization,” J. Am. Chem. Soc. **143**, 588–592 (2021).

[88] J.-J. Velasco-Velez, R. V. Mom, L.-E. Sandoval-Diaz, L. J. Falling, C.-H. Chuang, D. Gao, T. E. Jones, Q. Zhu, R. Arrigo, B. Roldan Cuenya, A. Knop-Gericke, T. Lunkenbein, and R. Schlögl, “Revealing the Active Phase of Copper during the Electroreduction of CO_2 in Aqueous Electrolyte by Correlating In Situ X-ray Spectroscopy and In Situ Electron Microscopy,” ACS Energy Lett. **5**, 2106–2111 (2020).

[89] K. P. Kuhl, E. R. Cave, D. N. Abram, and T. F. Jaramillo, “New insights into the electrochemical reduction of carbon dioxide on metallic copper surfaces,” Energy Environ. Sci. **5**, 7050–7059 (2012).

[90] J. Hong, S. Lee, S. Lee, H. Han, C. Mahata, H.-W. Yeon, B. Koo, S.-I. Kim, T. Nam, K. Byun, B.-W. Min, Y.-W. Kim, H. Kim, Y.-C. Joo, and T. Lee, “Graphene as an atomically thin barrier to Cu diffusion into Si,” Nanoscale **6**, 7503–7511 (2014).

[91] D. Prasai, J. C. Tuberquia, R. R. Harl, G. K. Jennings, and K. I. Bolotin, “Graphene: Corrosion-Inhibiting Coating,” ACS Nano **6**, 1102–1108 (2012).

[92] J. C. Girard, Y. Samson, S. Gauthier, S. Roussel, and J. Klein, “STM study of the nucleation and annealing of ion bombardment induced defects on Cu(100),” Surf. Sci. **302**, 73–80 (1994).

[93] J. B. Hannon, C. Klünker, M. Giesen, H. Ibach, N. C. Bartelt, and J. C. Hamilton, “Surface Self-Diffusion by Vacancy Motion: Island Ripening on Cu(001),” Phys. Rev. Lett. **79**, 2506–2509 (1997).

[94] J. Kunze, V. Maurice, L. H. Klein, H.-H. Strehblow, and P. Marcus, “In situ STM study of the anodic oxidation of Cu(001) in 0.1 M NaOH,” J. Electroanal. Chem. **554-555**, 113–125 (2003).

[95] B. Eren, D. Zherebetskyy, L. L. Patera, C. H. Wu, H. Bluhm, C. Africh, L.-W. Wang, G. A. Somorjai, and M. Salmeron, “Activation of Cu(111) surface by decomposition into nanoclusters driven by CO adsorption,” Science **351**, 475–478 (2016).

[96] B. Eren, Z. Liu, D. Stacchiola, G. A. Somorjai, and M. Salmeron, “Structural Changes of Cu(110) and Cu(110)-(2 × 1)-O Surfaces under Carbon Monoxide in the Torr Pressure Range Studied with Scanning Tunneling Microscopy and Infrared Reflection Absorption Spectroscopy,” J. Phys. Chem. C **120**, 8227–8231 (2016).

[97] J. Resasco, L. D. Chen, E. Clark, C. Tsai, C. Hahn, T. F. Jaramillo, K. Chan, and A. T. Bell, “Promoter Effects of Alkali Metal Cations on the Electrochemical Reduction of Carbon Dioxide,” J. Am. Chem. Soc. **139**, 11277–11287 (2017).

[98] E. Pérez-Gallent, G. Marcandalli, M. C. Figueiredo, F. Calle-Vallejo, and M. T. M. Koper, “Structure- and Potential-Dependent Cation Effects on CO Reduction at Copper Single-Crystal Electrodes,” J. Am. Chem. Soc. **139**, 16412–16419 (2017).

[99] Y.-G. Kim, J. H. Baricuatro, and M. P. Soriaga, “Surface reconstruction of polycrystalline Cu electrodes in aqueous $KHCO_3$ electrolyte at potentials in the early stages of CO_2 reduction,” Electrocatalysis **9**, 526–530 (2018).

[100] S. B. Scott, T. V. Hogg, A. T. Landers, T. Maagaard, E. Bertheussen, J. C. Lin, R. C. Davis, J. W. Beeman, D. Higgins, W. S. Drisdell, C. Hahn, A. Mehta, B. Seger, T. F. Jaramillo, and I. Chorkendorff, “Absence of Oxidized Phases in Cu under CO Reduction Conditions,” ACS Energy Lett. **4**, 803–804 (2019).

[101] M. Lampimäki, K. Lahtonen, M. Hirsimäki, and M. Valden, “Nanoscale oxidation of Cu(100): Oxide morphology and surface reactivity,” J. Chem. Phys. **126**, 034703 (2007).

[102] K. Lahtonen, M. Hirsimäki, M. Lampimäki, and M. Valden, “Oxygen adsorption-induced nanostructures and island formation on Cu{100}: Bridging the gap between the formation of surface confined oxygen chemisorption layer and oxide formation,” J. Chem. Phys. **129**, 124703 (2008).

[103] N. Cabrera and N. F. Mott, “Theory of the oxidation of metals,” Rep. Prog. Phys. **12**, 163–184 (1949).

[104] C. Gattinoni and A. Michaelides, “Atomistic details of oxide surfaces and surface oxidation: the example of copper and its oxides,” Surf. Sci. Rep. **70**, 424–447 (2015).

[105] K. Kern, H. Niehus, A. Schatz, P. Zeppenfeld, J. Goerge, and G. Comsa, “Long-range spatial self-organization in the adsorbate-induced restructuring of surfaces: Cu{100}-(2 ×1)O,” Phys. Rev. Lett. **67**, 855–858 (1991).

[106] K. Yagyu, X. Liu, Y. Yoshimoto, K. Nakatsuji, and F. Komori, “Dissociative Adsorption of Oxygen on Clean Cu(001) Surface,” J. Phys. Chem. C **113**, 5541–5546 (2009).

[107] H. Iddir, D. D. Fong, P. Zapol, P. H. Fuoss, L. A. Curtiss, G.-W. Zhou, and J. A. Eastman, “Order-disorder phase transition of the Cu(001) surface under equilibrium oxygen pressure,” Phys. Rev. B **76**, 241404 (2007).

[108] M. Lee and A. J. H. McGaughey, “Energetics and kinetics of the $c(2 \times 2)$ to $(2\sqrt{2} \times \sqrt{2})R45^{\circ}$ transition during the early stages of Cu(100) oxidation,” Phys. Rev. B **83**, 165447 (2011).

[109] I. Platzman, R. Brener, H. Haick, and R. Tannenbaum, “Oxidation of Polycrystalline Copper Thin Films at Ambient Conditions,” J. Phys. Chem. C **112**, 1101–1108 (2008).

[110] J. S. Bunch, S. S. Verbridge, J. S. Alden, A. M. van der Zande, J. M. Parpia, H. G. Craighead, and P. L. McEuen, “Impermeable Atomic Membranes from Graphene Sheets,” Nano Lett. **8**, 2458–2462 (2008).

[111] M. Schriver, W. Regan, W. J. Gannerr, A. M. Zaniewski, M. F. Crommie, and A. Zett, “Graphene as a Long-Term Metal Oxidation Barrier: Worse Than Nothing,” ACS Nano **7**, 5763–5768 (2013).

[112] I. Wlasny, P. Dabrowski, M. Rogala, I. Pasternak, W. Strupinski, J. M. Baranowski, and Z. Klusek, “Impact of electrolyte intercalation on the corrosion of graphene-coated copper,” Corros. Sci. **92**, 69–75 (2015).

[113] K. Wong, S. J. Kang, C. W. Bielawski, R. S. Ruoff, and S. K. Kwak, “First-Principles Study of the Role of O2 and H2O in the Decoupling of Graphene on Cu(111),” J. Am. Chem. Soc. **138**, 10986–10994 (2016).

[114] H. Tissot, C. Wang, J. H. Stenlid, T. Brinck, and J. Weissenrieder, “The Surface Structure of Cu2O(100): Nature of Defects,” J. Phys. Chem. C **123**, 7696–7704 (2019).

[115] S. T. Mayer and R. H. Muller, “An In Situ Raman Spectroscopy Study of the Anodic Oxidation of Copper in Alkaline Media,” J. Electrochem. Soc. **139**, 426 (1992).

[116] P. Z. Sun, Q. Yang, W. J. Kuang, Y. V. Stebunov, W. Q. Xiong, J. Yu, R. R. Nair, M. I. Katsnelson, S. J. Yuan, I. V. Grigorieva, M. Lozada-Hidalgo, F. C. Wang, and A. K. Geim, “Limits on gas impermeability of graphene,” Nature **579**, 229–232 (2020).

[117] W. Wang, S. Yang, and A. Wang, “Observation of the unexpected morphology of graphene wrinkle on copper substrate,” Sci. Rep. **7** (2017), 10.1038/s41598-017-08159-8.

[118] M. Löffler, K. J. J. Mayrhofer, and I. Katsounaros, “Oxide Reduction Precedes Carbon Dioxide Reduction on Oxide-Derived Copper Electrodes,” J. Phys. Chem. C **125**, 1833–1838 (2021).

[119] J. Hui, M. Burgess, J. Zhang, and J. Rodríguez-López, “Layer Number Dependence of Li $^+$ Intercalation on Few-Layer Graphene and Electrochemical Imaging of Its Solid–Electrolyte Interphase Evolution,” ACS Nano **10**, 4248–4257 (2016).

[120] S. Zhao, R. Mu, Y. Ning, Q. Fu, and X. Bao, “Modulating electronic structure of graphene overlayers through electrochemical intercalation,” Appl. Surf. Sci. **522**, 146359 (2020).

[121] R. Blume, P. R. Kidambi, B. C. Bayer, R. S. Weatherup, Z.-J. Wang, G. Weinberg, M.-G. Willinger, M. Greiner, S. Hofmann, A. Knop-Gericke, and R. Schlögl, “The influence of intercalated oxygen on the properties of graphene on polycrystalline Cu under various environmental conditions,” Physical Chemistry Chemical Physics **16**, 25989–26003 (2014).

[122] Y. Yao, Q. Fu, Y. Y. Zhang, X. Weng, H. Li, M. Chen, L. Jin, A. Dong, R. Mu, P. Jiang, L. Liu, H. Bluhm, Z. Liu, S. B. Zhang, and X. Bao, “Graphene cover-promoted metal-catalyzed reactions,” Proc. Natl. Acad. Sci. U.S.A. **111**, 17023–17028 (2014).

[123] H. Li, J. Xiao, Q. Fu, and X. Bao, "Confined catalysis under two-dimensional materials," Proc. Natl. Acad. Sci. U.S.A. **114**, 5930–5934 (2017).

[124] H. Li, C. Guo, Q. Fu, and J. Xiao, "Toward Fundamentals of Confined Electrocatalysis in Nanoscale Reactors," J. Phys. Chem. Lett. , 533–539 (2019).

[125] S. Yasuda, K. Tamura, T.-o. Terasawa, M. Yano, H. Nakajima, T. Morimoto, T. Okazaki, R. Agari, Y. Takahashi, M. Kato, I. Yagi, and H. Asaoka, "Confinement of Hydrogen Molecules at Graphene–Metal Interface by Electrochemical Hydrogen Evolution Reaction," J. Phys. Chem. C **124**, 5300–5307 (2020).

[126] J. Wordsworth, T. M. Benedetti, A. Alinezhad, R. D. Tilley, M. A. Edwards, W. Schuhmann, and J. Justin Gooding, "The importance of nanoscale confinement to electrocatalytic performance," Chem. Sci. **11**, 1233–1240 (2020).

[127] M. Lozada-Hidalgo, S. Hu, O. Marshall, A. Mishchenko, A. N. Grigorenko, R. a. W. Dryfe, B. Radha, I. V. Grigorieva, and A. K. Geim, "Sieving hydrogen isotopes through two-dimensional crystals," Science **351**, 68–70 (2016).

[128] S. Titmuss, A. Wander, and D. A. King, "Reconstruction of Clean and Adsorbate-Covered Metal Surfaces," Chem. Rev. **96**, 1291–1306 (1996).

[129] G. A. Somorjai and Y. Li, *Introduction to Surface Chemistry and Catalysis*, 2nd ed. (Wiley, Hoboken, N.J, 2010).

[130] F. S. Roberts, K. P. Kuhl, and A. Nilsson, "Electroreduction of Carbon Monoxide Over a Copper Nanocube Catalyst: Surface Structure and pH Dependence on Selectivity," ChemCatChem **8**, 1119–1124 (2016).

[131] H. Liu, Y. Zhou, S. A. Kulinich, J.-J. Li, L.-L. Han, S.-Z. Qiao, and X.-W. Du, "Scalable synthesis of hollow Cu_2O nanocubes with unique optical properties via a simple hydrolysis-based approach," J. Mater. Chem. A **1**, 302–307 (2012).

[132] A. Eilert, F. S. Roberts, D. Friebel, and A. Nilsson, "Formation of Copper Catalysts for CO_2 Reduction with High Ethylene/Methane Product Ratio Investigated with In Situ X-ray Absorption Spectroscopy," J. Phys. Chem. Lett. **7**, 1466–1470 (2016).

[133] A. D. Handoko, F. Wei, Jenndy, B. S. Yeo, and Z. W. Seh, "Understanding heterogeneous electrocatalytic carbon dioxide reduction through operando techniques," Nat. Catal. **1**, 922 (2018).

[134] D. Grumelli, B. Wurster, S. Stepanow, and K. Kern, "Bio-inspired nanocatalysts for the oxygen reduction reaction," Nat. Commun. **4**, 2904 (2013).

[135] L. Martin, H. Martinez, D. Poinot, B. Pecquenard, and F. Le Cras, "Comprehensive X-ray Photoelectron Spectroscopy Study of the Conversion Reaction Mechanism of CuO in Lithiated Thin Film Electrodes," J. Phys. Chem. C **117**, 4421–4430 (2013).

[136] K. Andersson, G. Ketteler, H. Bluhm, S. Yamamoto, H. Ogasawara, L. G. M. Pettersson, M. Salmeron, and A. Nilsson, "Bridging the Pressure Gap in Water and Hydroxyl Chemistry on Metal Surfaces: The Cu(110) Case," J. Phys. Chem. C **111**, 14493–14499 (2007).

[137] X. Yin, Y. Li, F. Ke, C. Lin, H. Zhao, L. Gan, Z. Luo, R. Zhao, T. F. Heinz, and Z. Hu, “Evolution of the Raman spectrum of graphene grown on copper upon oxidation of the substrate,” Nano Res. **7**, 1613–1622 (2014).

[138] Y. Deng, A. D. Handoko, Y. Du, S. Xi, and B. S. Yeo, “In Situ Raman Spectroscopy of Copper and Copper Oxide Surfaces during Electrochemical Oxygen Evolution Reaction: Identification of CuIII Oxides as Catalytically Active Species,” ACS Catal. **6**, 2473–2481 (2016).

[139] R. M. Arán-Ais, F. Scholten, S. Kunze, R. Rizo, and B. Roldan Cuenya, “The role of in situ generated morphological motifs and Cu(I) species in C_{2+} product selectivity during CO_2 pulsed electroreduction,” Nat. Energy **5**, 317–325 (2020).

[140] R. M. Arán-Ais, R. Rizo, P. Grosse, G. Algara-Siller, K. Dembélé, M. Plodinec, T. Lunkenbein, S. W. Chee, and B. R. Cuenya, “Imaging electrochemically synthesized Cu_2O cubes and their morphological evolution under conditions relevant to CO_2 electroreduction,” Nat. Commun. **11**, 3489 (2020).

[141] P. Grosse, A. Yoon, C. Rettenmaier, S. W. Chee, and B. R. Cuenya, “Growth Dynamics and Processes Governing the Stability of Electrodeposited Size-Controlled Cubic Cu Catalysts,” J. Phys. Chem. C **124**, 26908–26915 (2020).

[142] F. D. Speck and S. Cherevko, “Electrochemical copper dissolution: A benchmark for stable CO_2 reduction on copper electrocatalysts,” Electrochem. Commun. **115**, 106739 (2020).

[143] M. J. A. Shiddiky, A. P. O’Mullane, J. Zhang, L. D. Burke, and A. M. Bond, “Large Amplitude Fourier Transformed AC Voltammetric Investigation of the Active State Electrochemistry of a Copper/Aqueous Base Interface and Implications for Electrocatalysis,” Langmuir **27**, 10302–10311 (2011).

[144] P. Marcus, V. Maurice, and H. H. Strehblow, “Localized corrosion (pitting): A model of passivity breakdown including the role of the oxide layer nanostructure,” Corros. Sci. **50**, 2698–2704 (2008).

[145] W.-C. Huang, L.-M. Lyu, Y.-C. Yang, and M. H. Huang, “Synthesis of Cu_2O nanocrystals from cubic to rhombic dodecahedral structures and their comparative photocatalytic activity,” J. Am. Chem. Soc. **134**, 1261–1267 (2012).

[146] G. Ayrault and G. Ehrlich, “Surface self-diffusion on an fcc crystal: An atomic view,” J. Chem. Phys. **60**, 281–294 (1974).

[147] G. Ehrlich and F. G. Hudda, “Atomic View of Surface Self-Diffusion: Tungsten on Tungsten,” J. Chem. Phys. **44**, 1039–1049 (1966).

[148] K. Morgenstern, G. Rosenfeld, and G. Comsa, “Decay of Two-Dimensional Ag Islands on Ag(111),” Phys. Rev. Lett. **76**, 2113–2116 (1996).

[149] G. Schulze Icking-Konert, M. Giesen, and H. Ibach, “Decay of Cu adatom islands on Cu(111),” Surf. Sci. **398**, 37–48 (1998).

[150] J. M. Wen, S. L. Chang, J. W. Burnett, J. W. Evans, and P. A. Thiel, “Diffusion of Large Two-Dimensional Ag Clusters on Ag(100),” Phys. Rev. Lett. **73**, 2591–2594 (1994).

[151] J.-M. Wen, J. W. Evans, M. C. Bartelt, J. W. Burnett, and P. A. Thiel, “Coarsening Mechanisms in a Metal Film: From Cluster Diffusion to Vacancy Ripening,” Phys. Rev. Lett. **76**, 652–655 (1996).

[152] C. R. Stoldt, C. J. Jenks, P. A. Thiel, A. M. Cadilhe, and J. W. Evans, “Smoluchowski ripening of Ag islands on Ag(100),” J. Chem. Phys. **111**, 5157–5166 (1999).

[153] W. W. Pai, A. K. Swan, Z. Zhang, and J. F. Wendelken, “Island Diffusion and Coarsening on Metal (100) Surfaces,” Phys. Rev. Lett. **79**, 3210–3213 (1997).

[154] O. V. Lysenko, V. S. Stepanyuk, W. Hergert, and J. Kirschner, “Mesoscopic Relaxation in Homoepitaxial Metal Growth,” Phys. Rev. Lett. **89**, 126102 (2002).

[155] A. Auer, M. Andersen, E.-M. Wernig, N. G. Hörmann, N. Buller, K. Reuter, and J. Kunze-Liebhäuser, “Self-activation of copper electrodes during CO electro-oxidation in alkaline electrolyte,” Nat. Catal. **3**, 797–803 (2020).

[156] G. H. Simon, C. S. Kley, and B. R. Cuenya, “Potential-dependent Morphology of Copper Catalysts During CO_2 Electroreduction Revealed by In Situ Atomic Force Microscopy,” Angew. Chem. **60**, 2561–2568 (2021).

[157] C. R. Stoldt, A. M. Cadilhe, C. J. Jenks, J.-M. Wen, J. W. Evans, and P. A. Thiel, “Evolution of Far-From-Equilibrium Nanostructures Formed by Cluster-Step and Cluster-Cluster Coalescence in Metal Films,” Phys. Rev. Lett. **81**, 2950–2953 (1998).

[158] A. Rendón-Calle, Q. H. Low, S. H. Lee Hong, S. Builes, B. S. Yeo, and F. Calle-Vallejo, “How symmetry factors cause potential- and facet-dependent pathway shifts during CO2 reduction to CH4 on Cu electrodes,” Applied Catalysis B: Environmental , 119776 (2020).

[159] J. W. Evans and M. C. Bartelt, “Nucleation, Growth, and Kinetic Roughening of Metal(100) Homoepitaxial Thin Films,” Langmuir **12**, 217–229 (1996).

[160] M. Giesen, C. Steimer, and H. Ibach, “What does one learn from equilibrium shapes of two-dimensional islands on surfaces?” Surf. Sci. **471**, 80–100 (2001).

[161] L. C. Jorritsma, M. Bijnagte, G. Rosenfeld, and B. Poelsema, “Growth Anisotropy and Pattern Formation in Metal Epitaxy,” Phys. Rev. Lett. **78**, 911–914 (1997).

[162] F. L. W. Rabbering, G. Stoian, R. van Gastel, H. Wormeester, and B. Poelsema, “Oblique incidence deposition of Cu/Cu(001): Enhanced roughness and ripple formation,” Phys. Rev. B **81**, 115425 (2010).

[163] S. van Dijken, L. C. Jorritsma, and B. Poelsema, “Grazing-incidence metal deposition: Pattern formation and slope selection,” Phys. Rev. B , 14047–14058 (2000).

[164] R.-F. Xiao and N.-B. Ming, “Surface roughening and surface diffusion in kinetic thin-film deposition,” Phys. Rev. E **49**, 4720–4723 (1994).

[165] M. I. Haftel and M. Rosen, “Influence of the electrode potential on the Ehrlich-Schwoebel barrier,” Phys. Rev. B **68**, 165402 (2003).

[166] S. Kondati Natarajan and J. Behler, “Self-Diffusion of Surface Defects at Copper–Water Interfaces,” J. Phys. Chem. C **121**, 4368–4383 (2017).

[167] M. Giesen, “Step and island dynamics at solid/vacuum and solid/liquid interfaces,” Prog. Surf. Sci. **68**, 1–154 (2001).

[168] J. Fassbender, U. May, B. Schirmer, R. Jungblut, B. Hillebrands, and G. Güntherodt, “Oscillatory surface in-plane lattice spacing during growth of Co and of Cu on a Cu(001) single crystal,” Phys. Rev. Lett. **75**, 4476–4479 (1995).

[169] F. Golks, Y. Gründer, J. Stettner, K. Krug, J. Zegenhagen, and O. M. Magnussen, “In situ surface x-ray diffraction studies of homoepitaxial growth on Cu(001) from aqueous acidic electrolyte,” Surf. Sci. **631**, 112–122 (2015).

[170] M. Giesen and G. Schulze Icking-Konert, “Equilibrium fluctuations and decay of step bumps on vicinal Cu (111) surfaces,” Surf. Sci. **412-413**, 645–656 (1998).

[171] I. Takahashi, O. Koga, N. Hoshi, and Y. Hori, “Electrochemical reduction of CO_2 at copper single crystal Cu(S)-[n(111)×(111)] and Cu(S)-[n(110)×(100)] electrodes,” J. Electroanal. Chem. **533**, 135–143 (2002).

[172] R. B. Sandberg, J. H. Montoya, K. Chan, and J. K. Nørskov, “CO-CO coupling on Cu facets: Coverage, strain and field effects,” Surf. Sci. **654**, 56–62 (2016).

[173] K. J. Schouten, Y. Kwon, C. J. M. v. d. Ham, Z. Qin, and M. T. M. Koper, “A new mechanism for the selectivity to C_1 and C_2 species in the electrochemical reduction of carbon dioxide on copper electrodes,” Chem. Sci. **2**, 1902–1909 (2011).

[174] R. Kortlever, K. H. Tan, Y. Kwon, and M. T. M. Koper, “Electrochemical carbon dioxide and bicarbonate reduction on copper in weakly alkaline media,” J. Solid State Electrochem. **17**, 1843–1849 (2013).

[175] P. Qi, L. Zhao, Z. Deng, H. Sun, H. Li, Q. Liu, X. Li, Y. Lian, J. Cheng, J. Guo, Y. Cui, and Y. Peng, “Revisiting the Grain and Valence Effect of Oxide-Derived Copper on Electrocatalytic CO_2 Reduction Using Single Crystal Cu(111) Foils,” J. Phys. Chem. Lett. **12**, 3941–3950 (2021).

[176] B. Roldan Cuenya, private communication (2021).

[177] B. Roldan Cuenya, “Selectivity control in the electrocatalytic reduction of CO_2 through rational catalyst design,” seminar (May 2021).

[178] X. Fan, S. Wagner, P. Schädlich, F. Speck, S. Kataria, T. Haraldsson, T. Seyller, M. C. Lemme, and F. Niklaus, “Direct observation of grain boundaries in graphene through vapor hydrofluoric acid (VHF) exposure,” Sci. Adv. **4**, eaar5170 (2018).

[179] J.-Y. Lee, J.-H. Lee, M. J. Kim, J. K. Dash, C.-H. Lee, R. Joshi, S. Lee, J. Hone, A. Soon, and G.-H. Lee, “Direct observation of grain boundaries in chemical vapor deposited graphene,” Carbon **115**, 147–153 (2017).

[180] Y. H. Zhang, B. Wang, H. R. Zhang, Z. Y. Chen, Y. Q. Zhang, B. Wang, Y. P. Sui, X. L. Li, X. M. Xie, G. H. Yu, Z. Jin, and X. Y. Liu, "The distribution of wrinkles and their effects on the oxidation resistance of chemical vapor deposition graphene," Carbon **70**, 81–86 (2014).

[181] G. Zhou, W. Dai, and J. C. Yang, "Crater formation via homoepitaxy of adatoms dislodged from reducing oxide islands on metal surfaces," Phys. Rev. B **77**, 245427 (2008).

[182] L. Li and G. Zhou, "3D KMC simulations of crater growth during the reduction of oxide nanoislands on metal surfaces," Surf. Sci. **605**, 54–61 (2011).

[183] L. Zou, J. Li, D. Zakharov, E. A. Stach, and G. Zhou, "In situ atomic-scale imaging of the metal/oxide interfacial transformation," Nat. Commun. **8**, 307 (2017).

[184] H. Jung, S. Y. Lee, C. W. Lee, M. K. Cho, D. H. Won, C. Kim, H.-S. Oh, B. K. Min, and Y. J. Hwang, "Electrochemical fragmentation of Cu_2O nanoparticles enhancing selective C-C coupling from CO_2 reduction reaction," J. Am. Chem. Soc. **141**, 4624–4633 (2019).

[185] Q. Lei, H. Zhu, K. Song, N. Wei, L. Liu, D. Zhang, J. Yin, X. Dong, K. Yao, N. Wang, X. Li, B. Davaasuren, J. Wang, and Y. Han, "Investigating the Origin of Enhanced C_{2+} Selectivity in Oxide-/Hydroxide-Derived Copper Electrodes during CO_2 Electroreduction," J. Am. Chem. Soc. **142**, 4213–4222 (2020).

[186] S. H. Lee, I. Sullivan, D. M. Larson, G. Liu, F. M. Toma, C. Xiang, and W. S. Drisdell, "Correlating Oxidation State and Surface Area to Activity from Operando Studies of Copper CO Electroreduction Catalysts in a Gas-Fed Device," ACS Catal. **10**, 8000–8011 (2020).

[187] I. Nahalka, G. Zwaschka, R. K. Campen, A. Marchioro, and S. Roke, "Mapping Electrochemical Heterogeneity at Gold Surfaces: A Second Harmonic Imaging Study," J. Phys. Chem. C **124**, 20021–20034 (2020).

[188] J. H. K. Pfisterer, M. Baghernejad, G. Giuzio, and K. F. Domke, "Reactivity mapping of nanoscale defect chemistry under electrochemical reaction conditions," Nature Communications **10**, 5702 (2019).

[189] J. H. K. Pfisterer, Y. Liang, O. Schneider, and A. S. Bandarenka, "Direct instrumental identification of catalytically active surface sites," Nature **549**, 74–77 (2017).

[190] R. W. Haid, R. M. Kluge, Y. Liang, and A. S. Bandarenka, "In Situ Quantification of the Local Electrocatalytic Activity via Electrochemical Scanning Tunneling Microscopy," Small Methods **5**, 2000710 (2021).

[191] M. D. Lay, T. A. Sorenson, and J. L. Stickney, "High-Resolution Electrochemical Scanning Tunneling Microscopy (EC-STM) Flow-Cell Studies," J. Phys. Chem. B **107**, 10598–10602 (2003).

[192] A. Auer and J. Kunze-Liebhäuser, "A universal quasi-reference electrode for in situ EC-STM," Electrochemistry Communications **98**, 15–18 (2019).

[193] M. C. O. Monteiro, L. Jacobse, T. Touzalin, and M. T. M. Koper, “Mediator-Free SECM for Probing the Diffusion Layer pH with Functionalized Gold Ultramicroelectrodes,” Anal. Chem. **92**, 2237–2243 (2020).

[194] A. Krull, P. Hirsch, C. Rother, A. Schiffrin, and C. Krull, “Artificial-intelligence-driven scanning probe microscopy,” Communications Physics **3**, 1–8 (2020).

[195] C. S. Wondergem, T. Hartman, and B. M. Weckhuysen, “In Situ Shell-Isolated Nanoparticle-Enhanced Raman Spectroscopy to Unravel Sequential Hydrogenation of Phenylacetylene over Platinum Nanoparticles,” ACS Catal. **9**, 10794–10802 (2019).

[196] B. S. Vishnugopi, F. Hao, A. Verma, and P. P. Mukherjee, “Surface diffusion manifestation in electrodeposition of metal anodes,” Phys. Chem. Chem. Phys. **22**, 11286–11295 (2020).

[197] X. Wang, K. Klingan, M. Klingenhof, T. Möller, J. Ferreira de Araújo, I. Martens, A. Bagger, S. Jiang, J. Rossmeisl, H. Dau, and P. Strasser, “Morphology and mechanism of highly selective Cu(II) oxide nanosheet catalysts for carbon dioxide electroreduction,” Nature Communications **12**, 794 (2021).

[198] F. Mirabella, M. Müllner, T. Touzalin, M. Riva, Z. Jakub, F. Kraushofer, M. Schmid, M. T. M. Koper, G. S. Parkinson, and U. Diebold, “Ni modified Fe3O4(001) surface as a simple model system for understanding the Oxygen Evolution Reaction,” Electrochimica Acta , 138638 (2021).

[199] S. Jiang, K. Klingan, C. Pasquini, and H. Dau, “New aspects of operando Raman spectroscopy applied to electrochemical CO_2 reduction on Cu foams,” J. Chem. Phys. **150**, 041718 (2018).

[200] H. I. Rasool, E. B. Song, M. Mecklenburg, B. C. Regan, K. L. Wang, B. H. Weiller, and J. K. Gimzewski, “Atomic-Scale Characterization of Graphene Grown on Copper (100) Single Crystals,” J. Am. Chem. Soc. **133**, 12536–12543 (2011).

[201] M. R. Uhlig, D. Martin-Jimenez, and R. Garcia, “Atomic-scale mapping of hydrophobic layers on graphene and few-layer MoS_2 and WSe_2 in water,” Nat. Commun. **10**, 2606 (2019).

[202] A. Temiryazev, A. Frolov, and M. Temiryazeva, “Atomic-force microscopy study of self-assembled atmospheric contamination on graphene and graphite surfaces,” Carbon **143**, 30–37 (2019).

[203] A. Kovtun, D. Jones, S. Dell’Elce, E. Treossi, A. Liscio, and V. Palermo, “Accurate chemical analysis of oxygenated graphene-based materials using X-ray photoelectron spectroscopy,” Carbon **143**, 268–275 (2019).

[204] R. Larciprete, S. Fabris, T. Sun, P. Lacovig, A. Baraldi, and S. Lizzit, “Dual Path Mechanism in the Thermal Reduction of Graphene Oxide,” J. Am. Chem. Soc. **133**, 17315–17321 (2011).

[205] L. Stobinski, B. Lesiak, A. Malolepszy, M. Mazurkiewicz, B. Mierzwa, J. Zemek, P. Jiricek, and I. Bieloshapka, “Graphene oxide and reduced graphene oxide studied by the XRD, TEM and electron spectroscopy methods,” J. Electron Spectrosc. Relat. Phenom. **195**, 145–154 (2014).

[206] J. Kwak, Y. Jo, S.-D. Park, N. Y. Kim, S.-Y. Kim, H.-J. Shin, Z. Lee, S. Y. Kim, and S.-Y. Kwon, “Oxidation behavior of graphene-coated copper at intrinsic graphene defects of different origins,” Nat. Commun. **8**, 1549 (2017).

[207] Z. Li, Y. Wang, A. Kozbial, G. Shenoy, F. Zhou, R. McGinley, P. Ireland, B. Morganstein, A. Kunkel, S. P. Surwade, L. Li, and H. Liu, “Effect of airborne contaminants on the wettability of supported graphene and graphite,” Nat. Mater. **12**, 925–931 (2013).

Acknowledgements

"Science is a way of life. Science is a perspective. Science is the process that takes us from confusion to understanding in a manner that's precise, predictive and reliable - a transformation, for those lucky enough to experience it, that is empowering and emotional."

— Brian Greene

I am deeply honored for the opportunities that came along with my PhD studies. This journey was a wonderful experience that enriched me both scientifically and personally. I had the privilege to work on the state-of-the-art research topic in a great work environment, to learn from the world-leading experts and amazing scientists, to share the lab struggles with the enthusiastic students, and to meet fantastic colleagues.

I would like to express my deepest gratitude:

To Maggie Lingenfelder for being a fantastic mentor. Thank you for always being there for me, no matter how stupid the question was and how busy you were. Your guidance in the lab, science, and outside of science was essential for this project and me personally. Thank you for your continuous support, advice, and kindness. Also, I am grateful for your patience with me, especially for the moments when you might have wanted to desiccate me on an XPS chamber. I am forever in your debt. I hope that each PhD student gets a mentor as you were to me.

To Professors Beatriz Roldán Cuenya, Marc Koper, Giulia Tagliabue, and Romuald Houndré for taking time to read this thesis and for serving as jury members at my exam.

To Yunchang Liang for the great discussions, support, great moments, and laughs. You are a real inspiration, and I am deeply honored that I had a chance to work with you. I will certainly miss both the scientific and non-scientific discussions with you.

To Thanh Hai Phan, Fernando Cometto, and Bart Stel for teaching me the basics of EC-STM, electrochemistry, and AFM.

To Priscila Vensaus, Guillaume Dupont, Claudia Arbeitman, and Daniel Hurtado for a great work atmosphere and an amazing group synergy. Special thanks to Priscilla and Guillaume, who helped with proofreading and translation!

To Professor Marc Koper, Stefan Raaijman, and Chunmiao Yu for great collaboration and warm hospitality in Leiden.

To Patrick Alexa and Rico Gutzler for their help with the XPS measurements, the lessons on UHV surface science, and great discussions. Also, I am deeply grateful to Professor Klaus Kern for the fruitful discussions.

To Professor Nùria Lòpez, Rodrigo García Muelas, and Federico Datilla for discussions on theoretical model.

To the consortium of the Horizon 2020 A-LEAF project for amazing team synergy. I am deeply honored that I had an opportunity to learn from the world-leading experts and expand my knowledge outside of the strict surface science boundaries.

To Astrid Olaya Avendano, Natalia Gasilova, Gian Luca De Gregorio, and Professor Rafaella Buonsanti for their help with the CO_2RR product analysis. Big thanks to Astrid, who supervised me with the experiments.

To Arnaud Magrez, Yoan Troillet, and Seunghwa Lee for their help with the Raman set-up.

To great collaborators with whom I had the privilege to work on many exciting research topics. First, to Professor Xile Hu and Seunghwa Lee for introducing me to OER catalysts. Second, to Professor Aleksandra Radenovic, Miao Zhang, and Martina Lihter for great collaboration on MoS_2 system. Third, Professor Christophe Galland, Wen Chen, and Aqeel Ahmed for insights in plasmonics.

To Tomislav with whom I shared the office in the last year of my PhD. Thank you for the scientific discussions and the words of comfort in the not-the-best moments.

To Anica and Neno for unconditional love and support.

To Anamarija for being there for me.

Publication list

An updated list of all published papers available at https://lingenfelder-lab.com/#publications

- Claudia Arbeitman, Claudia Simao Delgado, **Karla Banjac**, and Magalí Lingenfelder, "Nano and microstructured polymeric surfaces are bactericidal for *Klebsiella pneumoniae* multiresistant strains", in preparation.
- **Karla Banjac***, Di-Jiang Liu, Thanh Hai Phan, Yunchang Liang, Fernando P. Cometto, James Evans, and Magalí Lingenfelder, "Homoepitaxy processes during CO_2 electroreduction on polycrystalline Cu surfaces", submitted.
- **Karla Banjac***, Thanh Hai Phan, Fernando P. Cometto, Patrick Alexa, Yunchang Liang, Rico Gutzler, and Magalí Lingenfelder, "Surface chemistry of copper micro- and nanocubic catalysts for electrochemical CO_2 reduction", submitted.
- Yunchang Liang, Sofia De Oliveir Parreires, Seunghwa Lee, Victor Boureau, **Karla Banjac**, Jose H. Gallego, Xile Hu, David Écija, and Magalí Lingenfelder, "*Operando* investigation of Ni-Fe catalysts for water splitting: surface morphology, composition, and active centers", in preparation.
- Aqeel Ahmed, **Karla Banjac**, Sachin Verlekar, Fernando P. Cometto, Magalí Lingenfelder, and Christophe Galland, "Molecular layer morphology determines the stability of nanoparticle-on-mirror plasmonic cavities", *ACS Photonics*, in press, DOI:10.1021/acsphotonics.1c00645.
- Wen Chen, Philippe Roelli, Aqeel Ahmed, Sachin Verlekar, Huatian Hu, **Karla Banjac**, Magalí Lingenfelder, Tobias J. Kippenberg, Giulia Tagliabue, and Christophe Galland, "Intrinsic Luminescence Blinking from Plasmonic Nanojunctions", *Nature Communications*, 12, 2731, 2021, DOI:10.1038/s41467-021-22679-y.
- Miao Zhang, Martina Lihter, Tzu-Heng Chen, Michal Macha, Archith Rayabharam, **Karla Banjac**, Yanfei Zhao, Henyu Wang, Jing Zhang, Jean Comtet, Narayana R. Aluru, Magalí Lingenfelder, Andras Kis, and Aleksandra Radenovic, "Super-resolved Optical Mapping of Reactive Sulfur-Vacancies in Two-Dimensional Transition Metal Dichalcogenides", *ACS Nano*, 15, 4, 7168–7178, 2021, DOI:10.1021/acsnano.1c00373.
- Thanh Hai Phan[†], **Karla Banjac**[†], Fernando P. Cometto, Federico Dattila, Rodrigo García-Muelas, Stefan J. Raaijman, Chunmiao Ye, Marc T. M. Koper, Núria López, and Magalí Lingenfelder, "Emergence of Potential-Controlled Cu-Nanocuboids and Graphene-Covered Cu-Nanocuboids under *Operando* CO_2 Electroreduction", *Nano Letters* 21, 5, 2059-–2065, 2021, DOI:10.1021/acs.nanolett.0c04703. [†] contributed equally.
- Seunghwa Lee, **Karla Banjac**, Magalí Lingenfelder, and Xile Hu, "Oxygen Isotope Labeling Experiments Reveal Different Reaction Sites for the Oxygen Evolution Reaction on Nickel and Nickel Iron Oxides", *Angewandte Chemie*, 131, 30, 10401–10405, 2019, DOI:10.1002/anie.201903200.

Personal details

Name	**Karla Banjac**
Nationality	Croatia
Date of birth	January 27, 1994
Google Scholar	bqWkVi8AAAAJ
OrcID	0000-0001-7063-6213

Education

PhD in Physics 2017–2021
Max Planck-EPFL Nanolab, EPFL, Switzerland
Joint degree with Doctoral School of the Max Planck-EPFL Center
for Molecular Nanoscience and Technology

Master of Science (MSc) in
Nanoscience, Nanotechnology and Nanoengineering 2015–2017
Katholieke Universiteit Leuven, Belgium
Minor in Nanochemistry and Nanomaterials

Bachelor of Science (BSc) in Chemistry 2012–2015
University of Zagreb, Croatia

Distinctions

Best contribution prize
Dutch Scanning Probe Microscopy Day 2019, AMOLF, Amsterdam, The Netherlands.

Selected as one of eight contribution talks for 708. WE-Heraeus-Seminar: Operando surface science – Atomistic insights into electrified solid/liquid interfaces
Bad Honnef, Germany, 2019.

Conference contributions

Oral contributions

Operando surface science insight into copper-based catalysts for CO_2 reduction: Cu catalysts are dynamic
Pacifichem, Honolulu, US, December 2021.

Copper interfaces under electrochemical CO_2 reduction conditions: an *operando* study
Pacifichem, Honolulu, US, December 2021.

Emergence of potential-controlled Cu nanocubes under *operando* CO_2 reduction conditions

708. WE-Heraeus-Seminar: Operando surface science – Atomistic insights into electrified solid/liquid interfaces, Bad Honnef, Germany, December 2019.

Surface dynamics of the graphene-covered polycrystalline Cu under CO_2RR conditions
International Bunsen Discussion Meeting: Fundamentals and Applications of (Photo)Electrolysis for Efficient Energy Storage, Taormina, Italy, April 2019.

Surface reconstruction of graphene-covered polycrystalline Cu during electrochemical reduction of carbon dioxide
Science Day of the Max Planck-EPFL Center for Molecular Nanoscience and Technology, Lausanne, Switzerland, October 2018.

Adding a puzzle piece to the picture of biomolecular conformation: Local study of peptides at the solid-vacuum and solid-liquid interfaces
MRS Spring meeting, Phoenix, US, April 2018.

Posters

Surface dynamics of graphene-covered polycrystalline Cu during CO_2 electroreduction
Dutch Scanning Probe Microscopy Day, Amsterdam, Netherlands, November 2019.

Catalyst morphology evolution and chiral-induced spin selectivity effects on CO_2 reduction
Chirality at The Nanoscale, Ascona, Switzerland, October 2019.

Surface dynamics of graphene-covered Cu under CO_2 reduction conditions
35th Science of Surfaces, Interfaces and Nanostructures Meeting, Fribourg, Switzerland, January 2019.

Surface dynamics of graphene-covered Cu under CO_2 reduction conditions
Max Planck-EPFL Winter School: Quantum effects and miniaturization in Mechanics, Fluids, Optics and Electronics, Schloss Ringberg, Germany, January 2019.

Surface dynamics of a tunable graphene-covered Cu catalyst for electrochemical CO_2 reduction
Swiss Chemical Society Fall Meeting, EPFL, Lausanne, Switzerland, September 2018.

Surface dynamics of graphene-covered Cu under CO_2 reduction conditions
International Summer School "Power-to-X: Fundamentals and Applications of Modern Electrochemistry", Villars-sur-Ollon, Switzerland, August 2018.

Towards an artificial leaf: *In situ* studies of the CO_2 reduction reaction on metal surfaces
Max Planck-EPFL Summer School: Molecules at Surfaces and Interfaces – from Structure to Interaction, Berlin, Germany, September 2017.

Supervision

Master project:

Guillaume Dupont: "Bioinspired antimicrobial surfaces structured at the nanoscale", Institute of Physics, EPFL, 2021

Semester projects:

Guillaume Dupont: "Bioinspired antimicrobial nanostructured surfaces for biomedical devices", Institute of Physics, EPFL, 2020

Roeland Van Haecke: "Structural evolution of NiFe-based OER catalysts", Institute of Physics, EPFL, 2019

Professional Services

Horizon 2020 A-LEAF project

Oral contribution at the project panel review, Brussels, 2019

Oral contributions on the meetings of the A-LEAF board, 2017–2021

Organization

Selected as MRS Symposium Assistant, MRS Spring Meeting, Phoenix, U.S., 2018

Science popularization

Science outreach for Horizon 2020 A-LEAF project, including the A-LEAF video

Workshops for the preschool children: Magical Science sponsored by Student Section of the Croatian Chemical Society

Volunteer and co-organizer of the science popularization events, such as Science Festival Zagreb, Chemistry Department Door Open Day

Teaching

General Physics: Electromagnetism, PHYS-114, 2018–2020

General Physics: Mechanics, PHYS-101(c), 2017

Ce document a été imprimé au Centre d’impression EPFL,
imprimerie climatiquement neutre, certifiée myClimate.